Pathogenesis of anti-paranodal autoantibodies in peripheral neuropathies

---

Pathogenese anti-paranodaler Autoantikörper bei peripheren Neuropathien

Doctoral thesis for a doctoral degree
at the Graduate School of Life Sciences,
Julius-Maximilians-Universität Würzburg,
Section Neuroscience

submitted by

Julia Grüner
from
Ulm

Würzburg, 2021

Submitted on:

Members of the *Promotionskomitee*:

Chairperson: Prof. Dr. Keram Pfeiffer

Primary Supervisor: PD Dr. Kathrin Doppler

Supervisor (Second): Prof. Dr. Carmen Villmann

Supervisor (Third): Prof. Dr. Markus Sauer

Date of Public Defense:

Date of Receipt of Certificates:

Abstract

Autoantibodies against proteins of the node of Ranvier have been identified in a subset of patients with chronic inflammatory demyelinating polyradiculoneuropathy (CIDP). Main antigens targeted by autoantibodies are the paranodal proteins contactin 1 (CNTN1), neurofascin (NF) 155 or contactin associated protein (Caspr) as well as the nodal NF186. Several studies investigated the role of anti-paranodal autoantibodies in the pathophysiology of CIDP leading to the current knowledge that immunoglobulin G (IgG)4 deposition results in detachment of myelin from the axon at the paranodes. However, many questions remain unsolved. Thus, autoantibodies against NF155 have been well studied and their pathogenicity has been proven in an animal model *in vivo*. However, in some patients, autoantibodies against all isoforms of NF are detectable. These anti-pan-NF autoantibodies occur more rarely and lead to a very severe clinical phenotype. As the pathogenesis of patient-derived autoantibodies against pan-NF has never been investigated *in vivo* before, we used an animal model to study the effect of acute exposure to anti-pan-NF IgG3 by intraneural injections to the rat sciatic nerve. In addition, we used anti-NF155 IgG4 from a seropositive patient. Behavioral testings as well as nerve conduction studies did not reveal any deficits after injection neither for anti-NF155 nor for anti-pan-NF autoantibodies. This leads to the suspicion that the disease is more likely induced by a chronic process.

A common symptom in patients with anti-CNTN1 associated neuropathy is sensory ataxia and therefore, an involvement of dorsal root ganglia (DRGs) is hypothesized. We show that sera from anti-CNTN1 positive patients specifically bind to DRG neurons *in vitro* and reduce surface expression of CNTN1. This is most probably due to internalization mediated by coexisting IgG3 although IgG4 is the predominant subclass of autoantibodies. As it is known that CNTN1 interacts with the β1 subunit of specific sodium channels we analyzed channel expression and sodium currents of DRG neurons after incubation with anti-CNTN1 positive patients' sera. We identified reduced sodium currents after long-term treatment with patients' material although surface channel expression remained stable. We therefore concluded that CNTN1 might influence channel properties indirectly through auxiliary β1 subunits. Moreover, we suggest an involvement of DRG neurons in the pathogenesis of anti-CNTN1 associated CIDP as medium-large size neurons are more affected than small neurons. However, the exact mechanism of how anti-CNTN1 autoantibodies influence sodium channels should be subject of further studies.

Furthermore, preliminary results indicate that the epitope for anti-CNTN1 autoantibodies from seropositive patients might be associated with distinct clinical features. We could show that autoantibodies might be either directed against a conformational epitope as binding is prevented after deletion of the first immunoglobulin (Ig) domain of CNTN1 or against the fibronectin type III (FnIII) domains. Strikingly, both patients with FnIII domain specificity had very high titers of anti-CNTN1 autoantibodies and a chronic disease progression, whereas patients binding to a conformational epitope or to the Ig domains are related to a relapsing-remitting or even monophasic disease course. However, these results need to be further confirmed before a clear statement can be made.

In conclusion, the present study contributes to elucidate the pathogenesis of peripheral neuropathies associated with anti-paranodal autoantibodies. However, further studies are required including a higher number of patients as well as considering effects on structures like DRGs besides the node of Ranvier to fully understand the disease mechanisms.

Zusammenfassung

Autoantikörper gegen Proteine des Ranvierschen Schnürrings wurden bei einer Untergruppe von Patienten mit chronisch inflammatorischer demyelinisierender Polyradikuloneuropathie (CIDP) identifiziert. Antigene, gegen die sich die Autoantikörper hauptsächlich richten, sind die paranodalen Proteine Contactin 1 (CNTN1), Neurofascin (NF) 155 oder das Contactin-assoziierte Protein (Caspr) sowie das nodal exprimierte NF186. Mehrere Studien untersuchten die Rolle von anti-paranodalen Autoantikörpern in der Pathophysiologie der CIDP, was zu der aktuellen Erkenntnis führte, dass Immunglobulin G (IgG) 4-Ablagerungen die Ablösung des Myelins vom Axon an den Paranodien zur Folge haben. Viele Fragen bleiben jedoch ungelöst. So sind Autoantikörper gegen NF155 gut untersucht worden und ihre Pathogenität wurde in einem Tiermodell *in vivo* nachgewiesen. Bei einigen Patienten sind jedoch Autoantikörper gegen alle Isoformen von NF nachweisbar. Diese anti-pan-NF-Autoantikörper treten seltener auf und führen zu einem sehr schweren klinischen Phänotyp. Da die Pathogenese von Autoantikörpern gegen pan-NF bisher nicht *in vivo* untersucht wurde, haben wir in einem Tiermodell die Wirkung der akuten Exposition von anti-pan-NF IgG3 durch intraneurale Injektionen in den Ischiasnerv der Ratte untersucht. Zusätzlich verwendeten wir anti-NF155 IgG4 von einem seropositiven Patienten. Verhaltenstests sowie Nervenleitfähigkeitsuntersuchungen zeigten weder nach Injektion von anti-NF155 noch von anti-pan-NF-Autoantikörpern Defizite. Dies lässt den Verdacht aufkommen, dass die Erkrankung eher durch einen chronischen Prozess ausgelöst wird.

Ein häufiges Symptom bei Patienten mit anti-CNTN1-assoziierter Neuropathie ist die sensorische Ataxie, weshalb eine Beteiligung der Spinalganglien vermutet wird. Wir zeigen, dass Seren von anti-CNTN1-positiven Patienten *in vitro* spezifisch an Spinalganglion-Neurone binden und die Oberflächenexpression von CNTN1 reduzieren. Dies ist höchstwahrscheinlich auf eine Internalisierung zurückzuführen, die durch koexistierendes IgG3 vermittelt wird, obwohl IgG4 die vorherrschende Subklasse der Autoantikörper ist. Da bekannt ist, dass CNTN1 mit der β1-Untereinheit von spezifischen Natriumkanälen interagiert, haben wir die Kanalexpression und die Natriumströme von Spinalganglion-Neuronen nach Inkubation mit anti-CNTN1-positiven Patientenseren analysiert. Wir stellten reduzierte Natriumströme nach Langzeitbehandlung mit Patientenmaterial fest, obwohl die Oberflächenkanalexpression stabil blieb. Daraus schlossen wir, dass CNTN1 die Kana-

leigenschaften möglicherweise indirekt über die β1-Untereinheiten beeinflusst. Darüber hinaus legen wir eine Beteiligung von Spinalganglion-Neuronen an der Pathogenese der anti-CNTN1-assoziierten CIDP nahe, da mittelgroße bis große Neurone stärker betroffen sind als kleine Neurone. Der genaue Mechanismus, wie anti-CNTN1-Autoantikörper Natriumkanäle beeinflussen, sollte jedoch Gegenstand weiterer Studien sein.

Darüber hinaus deuten vorläufige Ergebnisse darauf hin, dass das Epitop für anti-CNTN1-Autoantikörper von seropositiven Patienten mit unterschiedlichen klinischen Merkmalen assoziiert sein könnte. Wir konnten zeigen, dass die Autoantikörper entweder gegen ein konformationelles Epitop gerichtet sein könnten, da die Bindung nach Deletion der ersten Immunglobulin (Ig)-Domäne von CNTN1 verhindert wird, oder gegen die Fibronektin Typ III (FnIII)-Domänen. Auffallend ist, dass beide Patienten mit FnIII-Domänen-Spezifität sehr hohe anti-CNTN1-Autoantikörper Titer und einen chronischen Krankheitsverlauf aufwiesen, während Patienten, die an ein konformationelles Epitop beziehungsweise die Ig-Domänen binden, mit einem schubförmigen oder sogar monophasischen Krankheitsverlauf assoziiert sind. Diese Ergebnisse müssen jedoch noch weiter bestätigt werden, bevor eine klare Aussage getroffen werden kann.

Zusammenfassend trägt die vorliegende Studie dazu bei, die Pathogenese von peripheren Neuropathien, die mit anti-paranodalen Autoantikörpern assoziiert sind, aufzuklären. Es sind jedoch weitere Studien erforderlich, die eine größere Anzahl von Patienten einschließen und auch Auswirkungen auf Strukturen wie beispielsweise Spinalganglien neben dem Ranvierschen Schnürring berücksichtigen, um die Krankheitsmechanismen vollständig zu verstehen.

Contents

Parts of the results presented in this thesis have been accepted for publication:

Grüner, J., Stengel, H., Werner, C., Appeltshauser, L., Sommer, C., Villmann, C., and Doppler, K. (2021). "Anti-contactin-1 antibodies affect surface expression and sodium currents in dorsal root ganglia". In: *Neurology-Neuroimmunology Neuroinflammation.* DOI: 10.1212/NXI.0000000000001056.

The published manuscript and this thesis contain similar text passages in adapted form in some sections.

1 Introduction

Disorders of the peripheral nervous system (PNS) can affect large nerve fibers as well as small nerve fibers (Levine, 2018). Those peripheral neuropathies can be hereditary like in Friedreich's ataxia, Fabry disease or Charcot-Marie-Tooth disease, but can also be caused by diabetes, human immunodeficiency virus (HIV) or chemotherapy (Thomas et al., 2019). Furthermore, peripheral neuropathies can be autoimmune-mediated or idiopathic.

1.1 Nerve fiber classification

Nerve fibers of the PNS can be divided into three groups, based on their axon diameter, myelination degree and associated sensory receptors: A-fibers, B-fibers and C-fibers (Tubbs et al., 2015). A-fibers are myelinated and can be further classified as Aα-, Aβ-, Aγ- and Aδ-fibers. Aα-fibers are large nerve fibers with a diameter of 12–20 µm, show high conduction velocities of 70–120 m/s and are mainly responsible for innervation of extrafusal muscle fibers and proprioception. Aβ-fibers have diameters between 5 µm and 12 µm and conduction velocities of 30–70 m/s. These fibers innervate almost all mechanoreceptors except for free nerve endings. Aγ-fibers have a diameter of 3–6 µm, conduction velocities of 15–30 m/s and innervate intrafusal muscle spindles. In contrast to Aα- and Aβ-fibers, Aδ-fibers are only thinly myelinated, have smaller diameters of 2–5 µm and show slower conduction velocities (12–30 m/s). Aδ-fibers are responsible for innervation of free nerve endings and nociceptors that are also innervated by C-fibers. This type of nerve fiber is not myelinated and has only small diameters in a range of 0.5–2 µm which results in slow conduction velocities (0.5–2 m/s). B-fibers with diameters between 5 µm and 12 µm are myelinated, show conduction velocities of 15–30 m/s and innervate preganglionic fibers of the autonomic nervous system.

1.2 Saltatory conduction at the node of Ranvier

Since 1939 it is known that signal transduction is mainly saltatory in the central nervous system (CNS) and PNS of vertebrates (Tasaki, 1939; Huxley and Stämpfli, 1949). This is achieved by the myelin sheath which is wrapped around the axon and acts as an electrical insulator. The myelin sheath is only interrupted at the nodes of Ranvier where impulse conduction in form of action potentials takes place (Fig. 1.1). Together with other parameters like the axon diameter or the length of the segments between the nodes of Ranvier (internodes), myelination leads to significant increase in conduction velocity (Waxman, 1980). In contrast to oligodendrocytes in the CNS, Schwann cells form the myelin sheath around peripheral nerves. Both cell types belong to glial cells but their mechanisms underlying myelin development and assembly differ (Salzer, 2015). For example, an oligodendrocyte myelinates up to 50 axons, whereas a Schwann cell only forms a single myelin sheath around one axon (Baumann and Pham-Dinh, 2001).

After receiving information at the cell body, action potentials are generated at axon initial segments which are located at the base of axons and propagated along the axon. In myelinated nerves, the action potential “jumps” from one node of Ranvier to the next until reaching the synapses where the information is propagated by chemical transmission to the targeted cell.

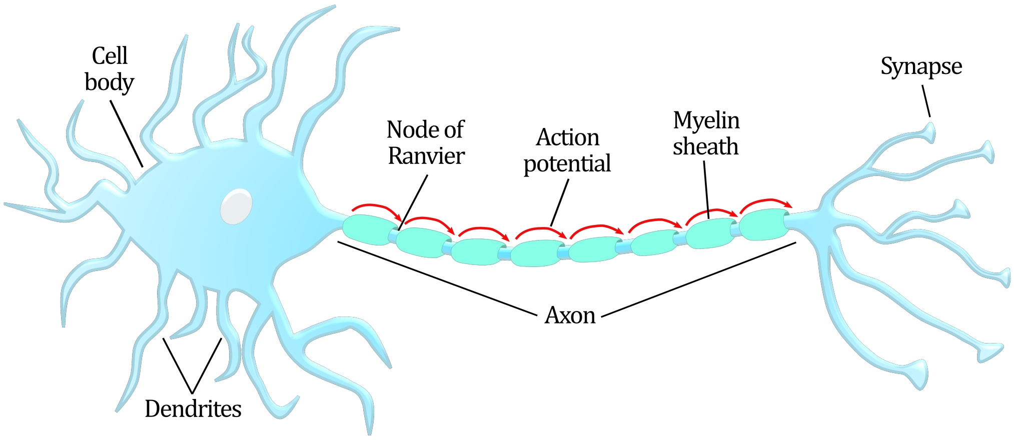

Figure 1.1: Saltatory conduction in neurons. Saltatory conduction of action potentials is achieved by the myelin sheath acting as an electrical insulator around the axon. The myelin is only interrupted at the nodes of Ranvier were impulse conduction takes place.

1.2.1 The node of Ranvier

Conduction of action potentials in myelinated neurons takes place at nodes of Ranvier (Fig. 1.2, A). The node of Ranvier is a highly organized structure consisting of three different regions: the juxtaparanode (Fig. 1.2, B), the paranode (Fig. 1.2, C) and the node (Fig. 1.2, D). Each of these domains contains distinct proteins leading to a specialized function. At the paranode, myelin is attached to the axon by the protein complex of the neuronal CNTN1 and Caspr and the glial NF 155. This paranodal complex is required to generate a diffusion barrier for voltage-gated ion channels. Thereby, not only voltage-gated sodium (Na_V) channels are clustered at the node in an area of 1–2 µm (Salzer, 1997), but also voltage-gated potassium (K_V) channels are clustered at the juxtaparanodal region.

At the node, specific Na_V and K_V channels are located to enable rapid depolarization and repolarization. Na_V channels are large multimeric complexes that consist of an α subunit and one or more smaller β subunits (Yu and Catterall, 2003). The α subunits of the channel are encoded by ten genes. $Na_V1.1$, $Na_V1.2$ and $Na_V1.3$ are mainly expressed in the CNS whereas $Na_V1.7$, $Na_V1.8$ and $Na_V1.9$ are located predominantly in the PNS (Catterall, 2012). In adult nodes of Ranvier, $Na_V1.6$ is the most abundant channel subtype both in the CNS and PNS (Schafer et al., 2006). $Na_V1.4$ is primarily expressed in skeletal muscle while $Na_V1.5$ is mainly located in the heart and Na_X, which is not voltage-gated, is involved in salt sensing (Catterall, 2012). Expression and gating properties of the α subunits are modified by the auxiliary β subunits (Ahern et al., 2016). Currently, four β subunits are known from which $\beta1$ and $\beta3$ are associated non-covalently and $\beta2$ and $\beta4$ interact via disulfide bonds with the α subunit of the channel (Catterall, 2012). Interestingly, β subunits have structural similarity to cell adhesion molecules (CAMs) which is further discussed in 1.2.2.

A direct interaction partner of axonal Na_V channels is ankyrin G (Fig. 1.2, D) which, together with βIV-spectrin, plays a role not only in channel clustering at the node but also in modulating gating properties of the Na_V channels (Komada and Soriano, 2002; Shirahata et al., 2006). In addition, ankyrin G anchors NF186 and the neuronal cell adhesion molecule (NrCAM) to the cytoskeleton. NF186 is a nodal NF isoform encoded by the *Nfasc* gene and consists of four FnIII domains, six Ig domains and a mucin domain between the FnIII domains 4 and 5 (Fig. 1.2, D). Recently, it has been shown that ablation of NF186 leads to progressive nodal disorganization and axonal degeneration in mice (Taylor et al., 2017). Thus, NF186 plays a crucial role in Na_V channel clustering at the node of Ranvier, thereby contributing to proper transmission of action potentials.

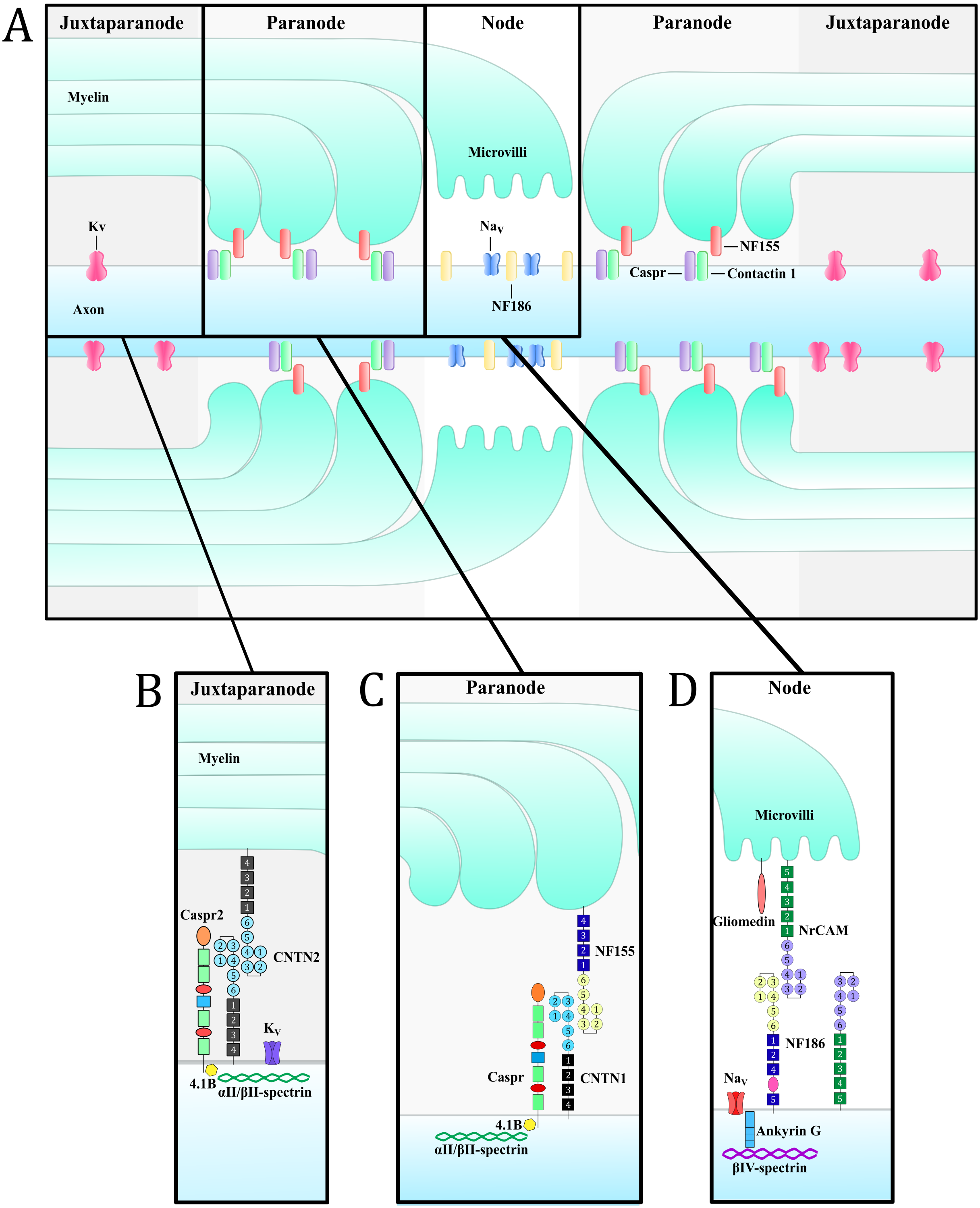

Figure 1.2: Scheme of the node of Ranvier. The node of Ranvier (A) in myelinated nerves can be divided into the juxtaparanodal (B), the paranodal (C) and the nodal region (D). Each domain contains specific proteins leading to specific functions. At the node, voltage-gated sodium channels (Na$_V$) are located which are essential for the generation of action potentials. The paranodal complex of contactin 1 (CNTN1), Caspr and neurofascin 155 (NF155) is essential as it works as a diffusion barrier for ion channels. At the juxtaparanode, voltage-gated potassium channels (K$_V$) contribute to rapid repolarization after depolarization of an action potential.

1.2.2 The paranode

Proper distribution of nodal voltage-gated sodium channels and juxtaparanodal potassium channels is achieved by the attachment of myelin loops to the axon at the paranode. This requires the interaction of the glial protein NF155 with the axonal proteins CNTN1 and Caspr resulting in a physiological barrier (Faivre-Sarrailh, 2020). Destruction of the paranodal architecture may lead to severe polyneuropathy which is described in detail in 1.3.7.

CNTN1 is a glycophosphatidylinositol (GPI) anchored CAM consisting of six Ig domains and four FnIII domains (Ranscht, 1988). CNTN1 interacts with Caspr in cis (on the same cell, Fig. 1.2, C). It has previously been shown that Caspr is retained in the endoplasmic reticulum when not associated with CNTN1 (Faivre-Sarrailh et al., 2000). This indicates that CNTN1 is either required for proper folding of Caspr and/or for the export to the membrane. CNTN1 is furthermore posttranslationally modified with N-linked glycans predominantly in the Ig domains. Especially the mannose-rich glycoform of CNTN1 is known to associate with NF155 in trans (Bonnon et al., 2007; Labasque et al., 2014) and is thus required for the formation of the paranodal complex. CNTN1 is not restricted to the paranodal domain of the peripheral node of Ranvier but is also strongly expressed throughout the whole CNS and in DRGs. Furthermore, low levels of CNTN1 have also been identified in pancreas, lung, kidney and skeletal muscle (Reid et al., 1994). Recent studies showed that CNTN1 overexpression is associated with metastasis in several types of cancer (Liu et al., 2012; Wu et al., 2012; Li et al., 2016; Chen et al., 2018).

Interestingly, the third Ig domain of CNTN1 has amino-acid sequence similarity to the Ig domain of the β2 subunit of Na_V channels (Isom and Catterall, 1996; Kazarinova-Noyes et al., 2001). Furthermore, the extracellular juxtamembrane regions of both proteins are homologous and CNTN1 as well as Na_V β2 are able to bind tenascin-R, a protein at CNS nodes (Xiao et al., 1996; Xiao et al., 1999). Thus, CNTN1 (like Na_V β2) may also interact with Na_V α or β1 subunits. Indeed, as shown via co-immunoprecipitation, CNTN1 associates specifically with the β subunit of $Na_V1.2$ channels and increases channel density at the plasma membrane (Kazarinova-Noyes et al., 2001). Additionally, CNTN1 associates with $Na_V1.3$ (Shah et al., 2004) and $Na_V1.8$ and $Na_V1.9$ in predominantly nociceptive DRG neurons (Liu et al., 2001; Rush et al., 2005).

CNTN1 interacts in trans with the glial NF155 which is besides the nodal NF186 (see 1.2.1) and NF140 another isoform of the *Nfasc* gene. NF140 is the embryonic isoform which has a similar function as NF186 in mature nodes, that is clustering of sodium channels at developing nodes of Ranvier (Zhang et al., 2015). Compared to NF186, NF155 lacks a mucin domain and the Ig5 domain, but has an additional Ig3 domain (Davis et al. (1996), Fig. 1.2, C).

The paranodal complex is linked to the cytoskeleton via Caspr which belongs to the family of neurexins. The intracellular region of Caspr interacts with the adapter protein 4.1B which in turn binds to αII/βII-spectrin, thus leading to a determined localization of the paranodal complex (Poliak and Peles (2003), Fig. 1.2, C).

1.2.3 The juxtaparanode

Adjacent to the paranode is the juxtaparanode (Fig. 1.2, B). In this domain, K_V1 channels are located in high densities contributing to fast repolarization of action potentials. These channels belong to the delayed rectifier K^+ channels of the *Shaker* family and comprise predominantly $K_V1.1$, $K_V1.2$ and the cytoplasmic $K_V\beta2$ subunit (Poliak and Peles, 2003; Rasband and Peles, 2015). Clustering of the channels requires axonal Caspr2 and CNTN2 which is located at the axon as well as at the glial side of the neuron (Poliak et al., 2003). Similar to the paranode, protein 4.1B links the complex to the axonal cytoskeleton through αII/βII-spectrin (Susuki et al., 2016).

1.3 Immune-mediated peripheral neuropathies

Peripheral neuropathies represent a heterogeneous group of disorders of the peripheral nervous system. Affected nerves can be motor, sensory or autonomic and one (mononeuropathy) or more nerves (polyneuropathy) can be involved resulting in various disease patterns. A well-known example for a mononeuropathy is the carpal tunnel syndrome caused by physical compression of the median nerve (Burton et al., 2014). Polyneuropathies can be inherited like Charcot-Marie-Tooth disease or acquired. Common causes of acquired polyneuropathies are diabetes, alcohol abuse, vitamin deficiency or chemotherapy. Furthermore, polyneuropathies can be immune-mediated which is described in detail in the following sections.

1.3.1 Classification of immune-mediated neuropathies

Autoimmune-mediated peripheral neuropathies are a diverse group of disorders that can generally be divided into acute and chronic forms. Acute neuropathies include Guillain-Barré syndrome (GBS), whereas CIDP is the most common chronic form. Clinical subtypes of GBS are the acute inflammatory demyelinating polyradiculoneuropathy (AIDP) and the primary axonal subtypes acute motor axonal neuropathy (AMAN) and acute motor and sensory axonal neuropathy (AMSAN) (Hernández-Torruco et al., 2014; Yadegari et al., 2014; Uncini and Kuwabara, 2018). Another rare GBS subtype is the Miller Fisher syndrome.

CIDP is characterized by a chronic progressive or relapsing and remitting disease course. Atypical CIDP forms include distal acquired demyelinating symmetric (DADS) neuropathy and multifocal acquired demyelinating sensory and motor (MADSAM) neuropathy also referred to as Lewis-Sumner syndrome (Pollard, 2002; Lehmann et al., 2019).

1.3.2 Epidemiology

GBS is the most common cause of acute and sub-acute flaccid paralysis worldwide (Esposito and Longo, 2017; Liu et al., 2018a). The incidence ranges between 0.62 to 2.66 per 100 000 people per year and increases with age (Sejvar et al., 2011). With a ratio of 3:2, males are slightly more often affected than females (Walling and Dickson, 2013). Incidences of GBS subtypes vary geographically. In North America and Europe, AIDP is the most common form with up to 60–80 % of GBS patients. In contrast, 30–65 % of patients in Asia show axonal forms of GBS (Berg et al., 2014). Miller Fisher syndrome is more common in Eastern Asia with up to 34 %, whereas in Europe this subtype is rather rare (3 %) (Doets et al., 2018). GBS is often associated with respiratory or gastrointestinal tract infection within 4 weeks of disease onset (Willison et al., 2016). It has been shown, that especially infections with *Campylobacter jejunii* are implicated in GBS pathogenesis (Hughes et al., 1999; Loshaj-Shala et al., 2015) but also infections with *Mycoplasma pneumoniae*, cytomegalovirus, Epstein-Barr virus, *Haemophilus influenzae*, influenza A virus and Zika virus have been reported to be associated with the disease (Mori et al., 2000; Hadden et al., 2001; Taheraghdam et al., 2014; Nascimento and Silva, 2017).

The most common chronic autoimmune neuropathy worldwide is CIDP with a prevalence of 1.9 to 8.9 per 100 000 people (Laughlin et al., 2009; Mathey et al., 2015). Like in GBS, men are more often affected and the prevalence increases with age (Broers et al., 2019).

About 50 % of CIDP patients show the classical clinical phenotype whereas 24–35 % are diagnosed with DADS and 8–15 % with MADSAM (Latov, 2014).

1.3.3 Clinical features

GBS is usually a monophasic disorder which reaches its nadir at 2 to 4 weeks after symptom onset (Hughes and Cornblath, 2005). After a plateau phase, progressive recovery over weeks or months takes place. However, 7–16 % of the patients show recurring episodes of worsening after initial improvement (Vucic et al., 2009). In general, clinical key features of GBS are rapidly progressive and symmetrical weakness of the limbs and hyporeflexia or areflexia (Berg et al., 2014; Liu et al., 2018a).

AIDP which is a sensorimotor subtype of GBS is further characterized by cranial nerve involvement, autonomic dysfunction and involvement of both proximal and distal muscles. In 25 % of AIDP patients mechanical ventilation is necessary because of respiratory muscle weakness (Vucic et al., 2009). Furthermore, AIDP is often accompanied by pain, whereas other sensory symptoms are rather mild (Berg et al., 2014).

In contrast to the demyelinating AIDP subtype, the axonal subtype AMAN is a pure motor syndrome with almost no sensory symptoms. The disease course is more rapid and severe compared to AIDP (Dimachkie and Barohn, 2013a) and cranial nerve involvement is less frequent. AMAN is sometimes accompanied by pain and autonomic dysfunction (Berg et al., 2014). AMSAN which is another axonal subtype of GBS can be considered as a severe form of AMAN where not only motor but also sensory fibers are affected (Dimachkie and Barohn, 2013a; Berg et al., 2014).

Miller Fisher syndrome, another GBS subtype, is typically characterized by a triad of ophthalmoplegia, areflexia and ataxia (Vucic et al., 2009; Esposito and Longo, 2017).

Similar to GBS, clinical key features of CIDP include symmetric proximal and distal weakness and absence of deep tendon reflexes (Latov, 2014). Furthermore, up to 75 % of patients with CIDP show fatigue (Boukhris et al., 2005) and more than one-third of patients suffer from moderate or severe chronic pain (Goebel et al., 2012). Additionally, mild autonomic dysfunction was reported (Pasangulapati et al., 2017). In contrast to GBS, the disease course in CIDP is slowly progressive or relapsing and symptoms develop at least over 8 weeks (Van den Bergh et al., 2010).

DADS, which is a subtype of CIDP, is characterized by symmetric distal weakness and sensory loss, whereas patients with MADSAM, another CIDP subtype, show asymmetric distal weakness combined with sensory deficits (Dimachkie and Barohn, 2013b).

1.3.4 Diagnosis

Diagnosis of GBS is determined by clinical examination (see 1.3.3), cerebrospinal fluid (CSF) analysis and nerve conduction studies (NCS). Two weeks after disease onset, albuminocytologic dissociation in the CSF, which means an increased protein level in combination with a normal cell count, is present in 90 % of the patients (Willison et al., 2016; Esposito and Longo, 2017). While NCS can be still normal at the beginning of the disease, nerve conduction abnormalities are usually detected one week after symptom onset (Gordon and Wilbourn, 2001). NCS are not only required to confirm the diagnosis of GBS but can also help to discriminate between demyelinating and axonal subtypes. In AIDP, signs of demyelination like prolonged distal motor latency (dml), reduced nerve conduction velocity (NCV), prolonged F-wave latency, increased temporal dispersion and conduction blocks are present (Berg et al., 2014; Willison et al., 2016; Esposito and Longo, 2017). In axonal variants of GBS signs of demyelination are absent in NCS, but the distal compound muscle action potential (CMAP) is decreased in AMAN. Some patients with AMAN additionally show reversible conduction failure (RCF) which is a transient conduction block or slowing that rapidly recovers during disease course and is a correlate of a paranodal dysfunction, not axonal damage (Uncini and Kuwabara, 2012). To differentiate between AMAN and AMSAN, sensory nerve studies can be performed where patients with AMSAN show reduced sensory nerve action potential (SNAP) amplitudes (Capasso et al., 2011). SNAP amplitudes are also decreased in 30 % of patients with Miller Fisher syndrome. Furthermore, H-reflexes are frequently absent in this subtype of GBS (Kuwabara et al., 2017).

For diagnosis of CIDP, diagnostic criteria of the European Federation of Neurological Societies/Peripheral Nerve Society are used most frequently for scientific studies which include clinical criteria, electrophysiological criteria and supportive criteria (Van den Bergh et al., 2010). Clinical criteria consist of inclusion and exclusion criteria and are based on the clinical presentation of typical and atypical CIDP described in 1.3.3. Electrophysiological criteria are divided into definite, probable and possible electrodiagnostic certainty. Definite signs can be motor distal prolongation, reduced motor conduction velocity, prolonged F-wave latencies or absent F-waves, a partial motor conduction block, abnormal temporal dispersion or increased distal CMAP duration (Van den Bergh et al., 2010).

One of these signs has to be fulfilled for more than one nerve in order to confirm definite CIDP diagnosis. For possible certainty, one of these criteria has to be fulfilled only in one nerve. Besides clinical and electrophysiological criteria, diagnosis of CIDP can be confirmed by supportive criteria which include CSF, magnetic resonance imaging (MRI) and nerve biopsy analysis. As in GBS, 80–95 % of all CIDP patients show albuminocytologic dissociation (Allen, 2020). In MRI, enlargement of the cauda equina, lumbosacral or cervical nerve roots or the brachial or lumbosacral plexuses are supportive for CIDP diagnosis (Lehmann et al., 2019). Histopathology of nerve biopsies often shows signs of demyelination or remyelination like thinly myelinated axons or onion bulbs (Roggenbuck et al., 2018). Furthermore, endoneurial oedema may occur. Based on these clinical, electrophysiological and supportive criteria, diagnosis of definite, probable or possible CIDP can be made. The CIDP subtype DADS can be distinguished from the typical CIDP clinically as weakness is only distal and not proximal and distal. Furthermore, conduction blocks are uncommon in DADS patients, whereas in typical CIDP patients this feature is very common (Saperstein et al., 2001). Diagnosis of MADSAM can be confirmed by the asymmetrical appearance which can be detected by clinical examination as well as in electrophysiological recordings (Saperstein et al., 2001).

1.3.5 Pathophysiology

As mentioned in 1.3.2, GBS patients often had a respiratory or gastrointestinal infection prior to disease onset. Such infections may play a crucial role in the pathophysiology of GBS, especially in the axonal subtypes AMAN and AMSAN. In 1993, molecular mimicry between surface molecules of *Campylobacter jejunii* and those of the axonal surface in AMAN was first described (Yuki et al., 1993). Here, specific lipo-oligosaccharides on the outer membrane of gram-negative *Campylobacter jejunii* mimic carbohydrates of gangliosides. This leads to antibody responses directed against lipo-oligosaccharides of the pathogen and additionally against structurally identical glycans on gangliosides of peripheral nerves like GM1, GD1a, GQ1b or GalNAc-GD1a (Willison et al., 2016; Liu et al., 2018a). These antibodies are of IgG 1 and IgG3 subclass and therefore activate complement which results in membrane attack complex formation at the nodal axolemma leading to axonal degeneration.

For Miller Fisher syndrome, the concept of molecular mimicry is even more prominent as about 90 % of patients are positive for antibodies against the ganglioside GQ1b (Mori and Kuwabara, 2011). As GQ1b is located at paranodal regions of ocular motor nerves, autoimmunity to this ganglioside leads to the typical symptom of ophthalmoplegia in

Miller Fisher syndrome (Chiba et al., 1993). In contrast to AMAN and Miller Fisher syndrome, the pathomechanism underlying the demyelinating AIDP is more complex and not completely understood yet. Although there are some reported cases in association with ganglioside or galactocerebroside antibodies (Samukawa et al., 2016), the role of autoantibodies in AIDP remains unclear. As complement deposition was found to be present at the Schwann cell surface in nerve biopsies of AIDP patients (Hafer-Macko et al., 1996), autoimmune reaction directed against an antigenic target at the Schwann cell surface is suggested. Typically, inflammatory infiltrates, endoneurial edema and multifocal segmental demyelination are present in nerve roots as well as in motor and sensory nerves (Lehmann et al., 2009; Liu et al., 2018a). Macrophages may penetrate the basal lamina of Schwann cells resulting in demyelination (Kaida, 2019) and the typical electrophysiological features of AIDP patients.

In contrast to GBS, preceding infections with pathogens are uncommon in CIDP. Although the target antigen is unknown in most CIDP patients, there is evidence for an autoimmune mechanism. The classical concept of CIDP pathophysiology is the macrophage induced demyelination (Koike and Katsuno, 2020). In the first step, pathogenic factors lead to disruption of the blood-nerve barrier (Tang et al., 2020). It is assumed that T cells activate macrophages resulting in phagocytosis and production of proinflammatory molecules (Lehmann et al., 2009). This theory is supported by the presence of inflammatory infiltrates containing T cells and macrophages in nerve biopsies of CIDP patients. Another pathomechanism in which the paranodal architecture is disrupted by autoantibodies against paranodal proteins is further described in 1.3.7.

1.3.6 Therapy

As GBS is a life-threatening disorder and up to 5 % of patients die from medical complications (Yuki and Hartung, 2012), optimum medical care can be lifesaving. In severe cases, monitoring of cardiac and pulmonary dysfunction and prevention of pulmonary embolism are most important. As GBS is an immune-mediated disorder, immunotherapy, such as plasma exchange (PE) or intravenous immune globulin (IVIg), has proven to be effective. By PE, antibodies and complement are filtered out of the blood and therefore PE leads to faster clinical improvement (Yuki and Hartung, 2012; Esposito and Longo, 2017). IVIg therapy results in antibody neutralization and inhibition of complement activation leading to an equal improvement as by PE therapy when initiated within two weeks after disease onset (Hughes and Cornblath, 2005; Yuki and Hartung, 2012).

IVIg is the best therapy option in CIDP as well. Additionally, treatment with corticosteroids shows similar clinical efficacy. PE might be considered in severe cases, as it leads to rapid improvement of symptoms. However, as this treatment is invasive and time-consuming and symptoms often deteriorate after first improvement, IVIg or corticosteroids are usually preferred for long-term treatment (Van den Bergh et al., 2010).

1.3.7 Nodo-paranodopathies

The concept of “nodo-paranodopathy” has recently been introduced by Uncini et al. (2013) to characterize peripheral neuropathies mediated by anti-ganglioside autoantibodies as the traditional classification into either axonal or demyelinating might be misleading in patients showing these autoantibodies. Thus, electrophysiological features in these patients resemble the demyelinating subtype although histopathologically no signs of demyelination are detectable. In the following years, the concept of “nodo-paranodopathy” was extended to include other autoimmune-mediated neuropathies related to the node of Ranvier as the primary site of immune attack (Uncini and Vallat, 2018). During this time, autoantibodies directed against proteins of the paranode were detected in a subset of patients with peripheral neuropathies (Mathey et al., 2007; Ng et al., 2012; Querol et al., 2013; Doppler et al., 2015; Doppler et al., 2016). Although less than 10 % of CIDP patients are seropositive (Doppler and Sommer, 2017), detection of autoantibodies is very important as the treatment response differs from seronegative patients. Similar to anti-ganglioside mediated neuropathy, no signs of demyelination are detectable in neuropathies associated with autoantibodies against paranodal proteins, but electrophysiological properties often resemble those in typical CIDP. Thus, conduction blocks, prolonged F-wave latency, prolonged dml and reduction of NCV are common in seropositive patients (Miura et al., 2015; Ogata et al., 2015; Doppler et al., 2016). Potential antigens of the paranode are CNTN1, NF155 or Caspr. Autoantibodies directed against Caspr alone have only been described in few patients so far (Doppler et al., 2016; Cortese et al., 2020) or in combination with CNTN1 autoantibodies (Querol et al., 2013). In contrast, anti-CNTN1 and anti-NF autoantibodies have been identified in several studies over the last years and will be discussed in the following sections.

1.3.7.1 Anti-contactin 1 associated neuropathy

In 2013, autoantibodies to CNTN1 were identified in two CIDP patients for the first time (Querol et al., 2013). Additionally, autoantibodies to both CNTN1 and Caspr were detected in another patient in this study. Seropositive patients shared common clinical features like advanced age, aggressive symptom onset, predominantly motor involvement, early axonal involvement and poor response to IVIg. Several studies confirmed the presence of CNTN1 autoantibodies in a small subset of CIDP patients with a frequency of 2.2–8.7 % (Doppler et al., 2015; Miura et al., 2015; Mathey et al., 2017; Lehmann et al., 2019). Additionally to the symptoms described in the first study by Querol et al. (2013), the follow-up studies also described sensory ataxia, disabling tremor or cranial nerve involvement (Doppler et al., 2015; Miura et al., 2015; Cortese et al., 2020; Dubey et al., 2020). A former study showed that NCV is dramatically reduced in CNTN1 mutant mice although axon diameter, myelin thickness and internodal distance were in the normal range (Boyle et al., 2001). Interestingly, sodium channel clustering at the node of Ranvier was not disrupted in those mice, but potassium channels, which are normally located at the juxtaparanodal region, were clustered at the paranode. In contrast to typical CIDP, neither macrophage mediated demyelination or onion bulbs nor inflammatory infiltrates were detected in nerve biopsies of anti-CNTN1 positive patients. CNTN1 autoantibodies cause destruction of paranodal junctions and thus, widening of the periaxonal space which leads to electrophysiological impairment (Doppler et al., 2015; Koike et al., 2017). Similar to typical demyelinating CIDP, conduction velocities are reduced, distal latencies and F-wave latencies are prolonged and CMAP is reduced.

Autoantibodies to CNTN1 are predominantly of the IgG4 subclass which does neither activate complement nor bind Fc-receptors. Furthermore, IgG4 causes little to no inflammation which is in accordance with nerve biopsy findings in seropositive patients (Huijbers et al., 2018). Thus, a blocking effect of the protein interaction at the paranodal junction by binding of CNTN1 autoantibodies is more likely than an inflammatory mechanism. The IgG subclass also accounts for the poor response to IVIg in most seropositive patients as this treatment interacts with the complement pathway (Shimizu et al., 2020). Therefore, detection of autoantibodies is of great importance in order to choose a patient-oriented treatment in an early stage of disease. Patients with anti-CNTN1 autoantibodies showed good response to rituximab (Doppler et al., 2015; Querol et al., 2015; Cortese et al., 2020; Dubey et al., 2020) which is a chimeric monoclonal antibody directed against CD20 on the membrane surface of B cells leading to depletion of this cell type (Huijbers et al., 2018). The efficacy and safety of rituximab in CIDP patients is subject of an ongoing study (Shimizu et al., 2020). Besides IgG4, IgG1 or IgG3 autoantibodies directed against CNTN1 have been detected as the most abundant subclass in a lower number of patients (Doppler et al., 2015; Cortese et al., 2020). Interestingly these subclasses were found predominantly during the acute phase at disease onset. As complement deposition could be detected in those patients, the pathomechanism differs depending on the present IgG subclass. It is supposed that antibody subclass switches from IgG3 to IgG4 occur during the disease course (Doppler et al., 2015).

Pathogenicity of anti-CNTN1 autoantibodies was proven *in vivo* by passive transfer to adult Lewis rats (Doppler et al., 2019). Whole purified IgG from anti-CNTN1 positive patients was used for intraneural injections directly to the sciatic nerve of the animals in order to simulate acute autoantibody exposure. Rats treated with whole IgG from a patient with predominantly IgG3 autoantibodies to CNTN1 showed conduction blocks and loss of F-waves in NCS. Moreover, motor deficits were detectable in behavioral testings, and paranodal complement deposition was seen at some nodes (Doppler et al., 2019). In contrast, animals treated with anti-CNTN1 positive IgG from a patient with mainly IgG4 autoantibodies did not show any abnormalities in behavioral testings. However, in some rats conduction blocks and loss of F-waves were detectable although the frequency was lower compared to animals treated with predominantly IgG3 (Doppler et al., 2019). It has been suggested that coexisting IgG3 in the whole purified IgG caused these alterations and that a pathogenic effect of IgG4 can more likely be detected in a chronic model than after acute exposure to anti-CNTN1 autoantibodies (Doppler et al., 2019).

Epitope mapping of anti-CNTN1 autoantibodies was performed in two studies (Labasque et al., 2014; Miura et al., 2015). Labasque et al. (2014) showed that specific *N*-linked glycosylations of CNTN1 are essential for autoantibody recognition, whereas the study of Miura et al. (2015) revealed that the epitope is independent of CNTN1 glycosylation and is located in the Ig5-Ig6 domain. These findings seem to be controversial, but it is also possible that autoantibodies from different patients may recognize different epitopes of the protein.

1.3.7.2 Anti-neurofascin associated neuropathy

Another antigen of the nodal/paranodal region in CIDP is NF. NFs are transmembrane proteins of the L1 CAM family which are ubiquitously expressed in both the CNS and PNS. Alternatively splicing of the *Nfasc* gene results in three isoforms of the protein. Neuronal NF140 is primarily expressed during embryonic development where it plays a role in Na_V channel clustering at developing nodes of Ranvier (Zhang et al., 2015). However, it has recently been shown that NF140 is also expressed in demyelinated white matter regions of multiple sclerosis patients (Zhang et al., 2015). The two other isoforms of NF are expressed at mature nodes of Ranvier. The glial NF155 forms a complex with CNTN1 and Caspr at the paranodal region by which the myelin loops are attached to the axon. This leads to a physiological diffusion barrier for juxtaparanodal K_V channels and nodal Na_V channels. NF186 is a neuronal isoform of the protein expressed at the nodes. Here, it is involved in Na_V channel clustering and prevents the invasion of paranodal loops to the nodal region (Thaxton et al., 2011).

Autoantibodies to NFs have first been detected in patients with multiple sclerosis by Mathey et al. (2007). The authors of this study found autoantibodies directed against both NF155 and NF186 in serum samples of multiple sclerosis patients. Furthermore, intraperitoneal (IP) injection of a monoclonal antibody against NF155/186 led to selective binding at nodes of CNS tissue and exacerbated disease in an experimental autoimmune encephalomyelitis (EAE) rat model.

A few years later, Ng et al. (2012) were the first detecting autoantibodies to NF in CIDP patients. They found an overall prevalence of 4 % of which most of the patients only showed reactivity to either NF155 or NF186. The reason for this specificity was that the epitope for NF155 autoantibodies was identified within the Fn3Fn4 domains which are unique for this isoform. For autoantibodies directed against NF186, the binding site was the mucin-Fn5 domain which is specifically expressed in NF186 (Ng et al., 2012). Main IgG subclasses for autoantibodies directed against the NF186 isoform were IgG1 and IgG3, for anti-NF155 autoantibodies the predominant subclass was IgG4. Authors could demonstrate prolonged and enhanced disease in an experimental autoimmune neuritis (EAN) rat model after intravenous injection of a monoclonal antibody against pan-NF. However, passive transfer of antibodies to naive rats did not lead to clinical deficits (Ng et al., 2012). In another study, a commercial anti-pan-NF antibody was administered to an EAN rat model by IP injection which exacerbated the clinical signs of the disease (Yan et al., 2014). Furthermore, the study showed that antibodies bind only to the nodal NF186 although they are directed against all isoforms of the protein. This suggests that the paranodal NF155 is inaccessible for antibodies *in vivo*. Additionally, intraneural injections of the commercial anti-pan-NF antibody to the rat sciatic nerve led to electrophysiological alterations 6 d after injection which recovered again at 17 d (Yan et al., 2014).

With a frequency of 4–18 % of CIDP patients, anti-NF155 autoantibodies are the most common detected anti-paranodal autoantibodies (Vural et al., 2018). CIDP associated with these autoantibodies is characterized by a younger age at disease onset (around 20–30 years), a predominantly distal phenotype, subacute onset and disabling tremor as well as sensory and cerebellar ataxia (Querol et al., 2014; Ogata et al., 2015; Devaux et al., 2016; Garg et al., 2018; Stengel et al., 2019). Furthermore, protein levels in CSF are elevated, nerve roots are often enlarged, and F-wave latencies as well as dml are prolonged

(Querol et al., 2014; Ogata et al., 2015; Kadoya et al., 2016). As autoantibodies to NF155 predominantly belong to the IgG4 subclass that does not activate complement, patients poorly respond to the standard therapy with IVIg. Rituximab may be considered as an alternative.

Pathogenicity of anti-NF155 autoantibodies *in vivo* was investigated in a passive transfer animal model where patient-derived autoantibodies were applied to neonatal or adult Lewis rats (Manso et al., 2019). The outcome of the study was that the formation of paranodes was prevented in neonatal animals by anti-NF155 autoantibodies and that they bind to the glial surface and cause depletion of NF155 in adult rats. This is in contrast to anti-CNTN1 associated polyneuropathy where a functional blocking activity of autoantibodies is proposed to disrupt the paranodal architecture (Doppler et al., 2019). The phenotype of rats treated with anti-NF155 was similar to that of anti-NF155 positive patients but without tremor. Additionally, characteristic electrophysiological features like conduction slowing were detected in the animals. However, signs of paranodal demyelination were not detected. Short-term application by intraneural injection of anti-NF155 autoantibodies to the rat sciatic nerve did not lead to any alterations (Manso et al., 2019).

Autoantibodies to NF186/140 or to all isoforms of NF (pan-NF) mainly belong to the IgG3 subclass and complement deposition induced by antibodies could be demonstrated (Delmont et al., 2017; Vallat et al., 2018; Stengel et al., 2019). The first patient with autoantibodies against pan-NF was described by Burnor et al. (2018). This patient was severely affected and almost completely locked-in. Initial symptoms comprised proximal and distal weakness and areflexia. Electrophysiological investigation revealed prolonged dml and F-waves and absent sensory responses. As the autoantibody subclass was mainly IgG4, the patient was refractory to treatment with IVIg or PE. However, Rituximab therapy resulted in gradual improvement of symptoms. A few months later, another patient with anti-pan-NF autoantibodies was described by Vallat et al. (2018). Symptoms strongly resembled those detected in the first patient by Burnor et al. (2018) with tetraplegia and almost complete locked-in, although autoantibodies from this patient belonged to the IgG3 subclass. As treatment with IVIg did not lead to improvement, the patient received corticosteroids and PE and improved quickly approximately three months after disease onset. Interestingly, autoantibody titers correlated with the clinical course and were not detectable anymore after recovery. Ultrastructural analysis of a sural nerve biopsy revealed lack of microvilli and paranodal invasion at the nodal region (Vallat et al., 2018).

Furthermore, Stengel et al. (2019) detected autoantibodies against pan-NF in three patients and autoantibodies specifically directed against NF155 in three additional patients. The IgG subclass of anti-pan-NF autoantibodies was IgG3. In contrast, IgG3 autoantibodies were detected only in one anti-NF155 positive patient. The main subclass of anti-NF155 autoantibodies in the two other patients was IgG4. Similar to both studies described before, patients with anti-pan-NF autoantibodies suffered from tetraplegia and showed cranial nerve involvement. This was the first study detecting paranodal/nodal autoantibodies (anti-pan-NF) in the CSF of one patient and not only in blood samples which may account for CNS involvement like cerebellar ataxia.

1.4 Aims of the study

Autoantibodies directed against proteins of the paranode can be identified in a subset of patients suffering from polyneuropathies. Pathogenicity of these autoantibodies has been examined *in vivo* by several studies (Ng et al., 2012; Yan et al., 2014; Doppler et al., 2019; Manso et al., 2019). Long-term exposure of autoantibodies against NF155 in a passive transfer rat model led to depletion of NF155 at paranodes (Manso et al., 2019). Intraneural injection of anti-CNTN1 autoantibodies resulted in conduction blocks and motor deficits (Doppler et al., 2019). Furthermore, two other studies showed that injection of a commercial anti-pan-NF antibody enhanced and prolonged disease in an EAN rat model (Ng et al., 2012; Yan et al., 2014). However, the pathogenesis of patient-derived autoantibodies against pan-NF *in vivo* has not been investigated yet. The present study aims to elucidate the pathological relevance of anti-NF autoantibodies from seropositive patients addressing the following questions:

Does acute exposure to anti-NF autoantibodies induce neuropathy *in vivo*?
Does the pathogenesis differ between anti-pan-NF and anti-NF155 autoantibodies?

To answer these questions, acute passive transfer of purified IgG from CIDP patients with anti-pan-NF or anti-NF155 autoantibodies was performed by intraneural injection to the sciatic nerve of adult Lewis rats. Behavioral testings as well as nerve conduction studies were performed before and after injection to investigate acute effects of anti-NF autoantibodies *in vivo*.

A major clinical symptom in anti-CNTN1 associated CIDP is sensory ataxia. This form of ataxia is often caused by damage to DRGs (Martinez et al., 2012). Recent studies reported a prevalence of 90–100 % of sensory ataxia in CIDP patients with anti-CNTN1 autoantibodies (Miura et al., 2015; Cortese et al., 2020; Delmont et al., 2020; Dubey et al., 2020). As the blood DRG barrier is more permeable than the blood nerve barrier (Reinhold and Rittner, 2020), DRGs are relatively easily accessible for autoantibodies. Therefore, we aimed to investigate the following question:

> Do autoantibodies against CNTN1 from seropositive patients have a pathological effect on DRG neurons *in vitro*?

To study this, DRG neurons were cultivated after isolation from adult wild-type mice and incubated with anti-CNTN1 positive patients' sera to test binding to the neurons. Furthermore, as CNTN1 is known to interact with sodium channels via their β subunit, whole-cell sodium currents of DRG neurons were analyzed after the treatment with serum of patients. To investigate if CNTN1 or Na_V expression is altered by the treatment, we additionally performed super-resolution microscopy.

In the last years, the binding site of CNTN1 for patients' autoantibodies was investigated in two studies (Labasque et al., 2014; Miura et al., 2015). While the first study reported posttranslational modifications of the protein as the epitope for anti-CNTN1 autoantibodies (Labasque et al., 2014), the latter identified the binding site in the Ig5-Ig6 domain of the protein core (Miura et al., 2015). As the findings of both studies are inconsistent, it is likely that different epitopes are involved in the pathogenesis of anti-CNTN1 associated CIDP. Those studies gave raise to the following question:

> Which epitope(s) of CNTN1 is/are recognized by patients' autoantibodies?

Concerning this matter, CNTN1 was modified by site-directed mutagenesis in order to remove *N*-linked glycosylations sites or whole Ig domains. Binding of patients' autoantibodies to these constructs of CNTN1 was evaluated in a HEK 293 cell-based assay. Furthermore, the unmodified protein was treated with the enzyme peptide-*N*-glycosidase F (PNGase F) to remove all *N*-linked glycosylations. Binding of autoantibodies from seropositive patients to unglycosylated CNTN1 was analyzed by immunoblotting.

2 Materials and methods

2.1 Materials

2.1.1 Technical equipment

Table 2.1: Technical equipment

Equipment	Company
Agfa CP1000 X-ray film processor	Agfa-Gevaert, Mortsel, Belgium
BioDocAnalyze Imaging System	Biometra GmbH, Göttingen, Germany
Biometra Compact M system	Analytik Jena AG, Jena, Germany
Block heater Cole-Parmer Stuart SBH130D	Cole-Parmer, Staffordshire, UK
Catwalk™ XT	Noldus, Weimar, Germany
Cell Culture Microscope CKX53	Olympus, Hamburg, Germany
Centrifuges	
Centrifuge 5424	Eppendorf, Hamburg, Germany
Centrifuge 5702	Eppendorf, Hamburg, Germany
Megafuge® 1.0 R	Heraeus, Osterode, Germany
MicroStar 17R	VWR International, Darmstadt, Germany
MiniSpin®	Eppendorf, Hamburg, Germany
Counting Chamber Improved Neubauer	Glaswarenfabrik Karl Hecht GmbH & Co KG, Sondheim vor der Röhn, Germany
FiveEasy pH meter F20	Mettler-Toledo, Columbus, Ohio, USA
Hargreaves Apparatus	Ugo Basile®, Gemonio, Italy
Heating table	MEDAX, Neumünster, Germany
Incubators	
HERAcell® CO_2 incubator	Kendro Laboratory Products, Hanau, Germany

Table 2.1: Technical equipment, continued

Equipment	**Company**
New Brunswick™ Innova® 42 Shaker	Eppendorf, Hamburg, Germany
Microscopes	
Axio ImagerM.2 with Apotome	Zeiss, Oberkochen, Germany
SIM Elyra S.1	Zeiss, Oberkochen, Germany
Microsyringes	Hamilton, Reno, Nevada, USA
Microwave	Robert Bosch GmbH, Gerlingen-Schillerhöhe, Germany
Mini-PROTEAN® 3 Cell	Bio-Rad Laboratories, Feldkirchen, Germany
Mini-PROTEAN® Tetra cell	Bio-Rad Laboratories, Feldkirchen, Germany
Neurosoft, Evidence 3102	Schreiber & Tholen Medizintechnik, Stade, Germany
Objectives	
Plan-Apochromat 20x/0.8 Ph2 M27	Zeiss, Oberkochen, Germany
Plan-Apochromat 40x/0.95 Korr M27	Zeiss, Oberkochen, Germany
Plan-Apochromat 63x/1.4 Oil DIC M27	Zeiss, Oberkochen, Germany
Plan-Apochromat 63x/1.4 Oil Ph3 M27	Zeiss, Oberkochen, Germany
P95DE digital printer	Mitsubishi Electric Europe B.V., Ratingen, Germany
Photometer	
BioPhotometer Plus	Eppendorf, Hamburg, Germany
NanoDrop 1000 Spectrophotometer	Thermo Fisher Scientific, Karlsruhe, Germany
PowerPac 300 Power Supply	Bio-Rad Laboratories, Feldkirchen, Germany
PowerPac Basic Power Supply	Bio-Rad Laboratories, Feldkirchen, Germany
RotaRod Advanced	TSE Systems, Bad Homburg, Germany

Table 2.1: Technical equipment, continued

Equipment	Company
Surgical cutlery	Fine Science Tools, Heidelberg, Germany
ThermoMixer® comfort	Eppendorf, Hamburg, Germany
TProfessional Basic Thermocycler Gradient	Biometra GmbH, Göttingen, Germany
Tumbling Table WT12	Biometra GmbH, Göttingen, Germany
Von Frey Aesthesiometer	Stoelting, Wood Dale, Illinois, USA
Vortex-Genie™ 2	Scientific Industries SI™, Bohemia, New York, USA
Waterbath WNB 7	Memmert GmbH & Co KG, Schwabach, Germany

2.1.2 Disposable material

Table 2.2: Disposable material

Disposable material	Company (Product #)
BD PlastiPak™ Luer Slip syringe	BD (REF300013)
Blotting Papers ROTILABO™	Carl Roth (CL67.1)
Carbon steel scalpel blades # 10	B. Braun (BB510)
CELLSTAR® Filter Cap Cell Culture Flasks	Greiner Bio-One (658175)
Cell scraper	Sarstedt (83.1830)
CoverGrip™ Coverslip Sealant	Biotium (23005)
Coverslips	
Cover glasses, round, 13 mm	VWR International (631-0149)
Cover slips, round, 12 mm	A. Hartenstein (DRK1)
Developer	Agfa (G153)
Fixer	Agfa (G354)
Nalgene™ Rapid-Flow™ Sterile Single Use Bottle Top Filters	Thermo Fisher Scientific (291-4520)

Table 2.2: Disposable material, continued

Disposable material	**Company (Product #)**
Needles	
Sterican® Needle 27G	B. Braun (4665457)
Sterican® Safety Needle 25G	B. Braun (4670016S-01)
Petri dishes	
Falcon® Bacteriological Petri Dishes	Corning (351008)
Nunc™ Cell-Culture Treated Multidishes	Thermo Fisher Scientific (142475)
Nunclon™ Delta, 35 x 10 mm Dish	Thermo Fisher Scientific (150318)
Petri dish 92 x 16 mm	Sarstedt (82.1473.001)
TC 35, Standard	Sarstedt (83.3900)
TC 100, Standard	Sarstedt (83.3902)
Tubes	
13 ml	Sarstedt (62.515.006)
15 ml	Greiner Bio-One (188271)
50 ml	Greiner Bio-One (227261)
Safe Seal tube 1.5 ml	Sarstedt (72.706)
Safe Seal tube 2.0 ml	Sarstedt (2.695.500)
Semi-micro cuvette, PS	Sarstedt (67.742)
Super PAP Pen Liquid Blocker	Science Services (N71310)
Suture	
Dafilon® 4/0	B. Braun (C0933341)
Silkam® 4/0	B. Braun (C0762253)
X-ray film Super RX-N	Fujifilm (47410-19284)

2.1.3 Reagents and chemicals

Table 2.3: Reagents and chemicals

Reagent	Company (Product #)
Agar-Agar, Kobe I	Carl Roth (5210)
Ammonium peroxydisulphate (APS)	Carl Roth (9592)
Biozym LE agarose	Biozym Scientific (840004)
Bovine serum albumin	Sigma-Aldrich (A4503-50G)
Fetal bovine serum	Sigma-Aldrich (F7524)
HotStar HiFidelity Polymerase Kit	Qiagen (202602)
Isofluran CP®	CP-Pharma (1214)
Markers and Ladders	
Color Prestained Protein Standard, Broad Range (10-250 kDa)	New England Biolabs (P7712)
Midori Green Advance DNA stain	Nippon Genetics Europe (MG04)
O’Gene Ruler™ 1 kb DNA ladder	Thermo Fisher Scientific (11551615)
pRK7 + Hinf DNA ladder	Prepared by AG Villmann
DNA marker	30 % glycerol; 0.2 M EDTA; 0.05 % bromphenol blue; 0.05 % xylene cyanol FF
Nerve Growth Factor-7S from murine submaxillary gland	Sigma-Aldrich (N0513)
Normal goat serum	Agilent (X0907)
Penicillin (10 000 Units/ml)/streptomycin (10 000 µg/ml)	Thermo Fisher Scientific (15140122)
Paraformaldehyde	Merck (1040051000)
Poly-D-lysine hydrobromide	Sigma-Aldrich (P6407)
Powdered milk, blotting grade	Carl Roth (T145)
ProLong™ Glass Antifade Mountant	Thermo Fisher Scientific (P36982)
TEMED	Carl Roth (2367)
Triton X-100	Sigma-Aldrich (T8787)
Ursotamin®, 100 mg/ml	Serumwerk Bernburg AG

Table 2.3: Reagents and chemicals, continued

Reagent	Company (Product #)
VECTASHIELD Antifade Mounting Medium with DAPI	Vector Laboratories (H-1200)
Xylavet®, 20 mg/ml	CP-Pharma(1206)

2.1.4 Antibodies

Table 2.4: Primary and secondary antibodies

Reactivity	Host	Company (Product #)	Application (dilution)
		Primary antibodies	
β III tubulin	chicken	abcam (ab41489)	Immunocytochemistry of DRG neurons (1:250)
β-actin	mouse	Biozol, GeneTex (GTX26276)	Loading control in Western Blotting (1:5000)
Caspr	rabbit	abcam (ab34151)	Immunohistochemistry of rat teased fibers (1:250)
Contactin-1	goat	R&D Systems (AF904)	Immunoblotting (1:500) Immunocytochemistry of HEK 293 cells (1:250) Immunocytochemistry of DRG neurons (1:250)
Sodium channel, pan	mouse	Sigma-Aldrich (S8809)	Immunohistochemistry of rat teased fibers (1:250) Analysis of DRG sodium channels (1:250)
		Secondary antibodies	
Alexa Fluor® 488 AffiniPure Anti-Goat IgG (H+L)	donkey	Jackson ImmunoResearch (705-545-147)	Detection of CNTN1 in SIM recordings of DRG neurons (1:250)

Table 2.4: Primary and secondary antibodies, continued

Reactivity	**Host**	**Company (Product #)**	**Application (dilution)**
Alexa Fluor® 488 AffiniPure Anti-Mouse IgG (H+L)	goat	Jackson ImmunoResearch (115-545-003)	Detection of Na_V channels in teased fibers
Alexa Fluor® 647 AffiniPure Anti-Rabbit IgG (H+L)	donkey	Jackson ImmunoResearch (711-605-152)	Detection of Caspr in teased fibers
ATTO 643 NHS-Ester Anti-Mouse IgG	goat	ATTO-TEC (AD 643-31; custom labeled by Dr. Christian Werner)	Detection of Na_V channels in SIM recordings of DRG neurons (1:250)
Cy™3 AffiniPure Anti-Chicken IgY (IgG) (H+L)	goat	Jackson ImmunoResearch (103-165-155)	Detection of β III tubulin in DRG neurons
Cy™3 AffiniPure Anti-Goat IgG (H+L)	donkey	Jackson ImmunoResearch (705-165-147)	Detection of CNTN1 in transfected HEK 293 cells
Cy™3 AffiniPure Anti-Human IgG (H+L)	goat	Jackson ImmunoResearch (109-165-003)	Detection of human IgG in HEK 293 cells and DRG neurons
Peroxidase AffiniPure Anti-Goat IgG (H+L)	donkey	Jackson ImmunoResearch (705-035-003)	Detection of CNTN1 by immunoblotting (1:15,000)
Peroxidase AffiniPure Anti-Human IgG (H+L)	donkey	Jackson ImmunoResearch (709-035-149)	Detection of human IgG by immunoblotting (1:15,000)
Peroxidase AffiniPure Anti-Mouse IgG (H+L)	donkey	Jackson ImmunoResearch (715-035-150)	Detection of β-actin by immunoblotting (1:15,000)

2.1.5 Media, buffers and solutions

Table 2.5: Media

Medium	Composition	Company (Product #)
HEK 293 medium	87 % MEM	Thermo Fisher Scientific (21090-022)
	10 % FBS	Sigma-Aldrich (F7524)
	1 % L-Glutamine	Thermo Fisher Scientific (25030-024)
	1 % Pen/Strep	Thermo Fisher Scientific (15140-122)
	1 % sodium pyruvate	Thermo Fisher Scientific (11360-039)
DRG medium	89 % DMEM/F-12, GlutaMAX™	Thermo Fisher Scientific (10565-018)
	10 % FCS	Sigma-Aldrich (F7524)
	1 % Pen/Strep	Thermo Fisher Scientific (15140-122)
Microbial growth medium	2x YT Broth	Carl Roth (X966.2)

Table 2.6: Buffers and solutions

Solution	Composition
2x HBS	50 mM HEPES; 12 mM D-Glucose; 10 mM KCl; 280 mM NaCl; 1.5 mM Na_2HPO_4 x 2 H_2O; pH 6.95
Blocking solution for HEK 293 cells	10 % BSA in PBS
Blocking solution for teased fibers	4 % NGS; 4 % FCS; 0.3 % Triton X-100 in 0.1 M PBS
Blocking solution for immunoblotting	5 % milk powder in TBS-T
$CaCl_2$	2.5 M $CaCl_2$; pH 7
External solution for electrophysiology	70 mM NaCl; 70 mM choline chloride, 3 mM KCl; 1 mM $MgCl_2$; 1 mM $CaCl_2$; 20 mM TEA-Cl; 5 mM CsCl; 0.1 mM $CdCl_2$; 10 mM HEPES; pH 7.3; 320 mOsm/l
Internal solution for electrophysiology	140 mM CsF; 1 mM EDTA; 10 mM NaCl; 10 mM HEPES; pH 7.3; 310 mOsm/l
PBS	137 mM NaCl; 2.7 mM KCl; 1.5 mM KH_2PO_4; 8.1 mM Na_2PO_4; pH 7.4

Table 2.6: Buffers and solutions, continued

Solution	Composition
Plasmid preparation buffer P1	50 mM glucose; 10 mM EDTA; 25 mM Tris-HCl; pH 8
Plasmid preparation buffer P2	200 mM NaOH; 1 % (w/v) SDS
Plasmid preparation buffer P3	3 M potassium acetate; 11.5 % (w/v) acetic acid
SDS running buffer	25 mM Tris; 192 mM glycine; 0.1 % (w/v) SDS; pH 8.3
SDS sample buffer 6x	90 mM Tris-HCl pH 6.8, 20 % (v/v) glycerol, 6 % (w/v) SDS, 0.02 % (w/v) bromphenol blue
TE buffer	10 mM Tris; 1 mM EDTA; pH 8
TBE buffer	89 mM Tris; 89 mM borate; 2 mM EDTA; pH 8.3
TBS-T buffer	50 mM Tris; 150 mM NaCl; 0.1 % Tween 20
Western Blot transfer buffer	25 mM Tris; 192 mM glycine; 10 % ethanol

2.1.6 Strains, primary cells and cell lines

Cells used in this study consisted of primary neurons, human cell lines and bacterial strains.

2.1.6.1 Primary neurons

Primary cells used in this study comprised dorsal root ganglion (DRG) neurons taken from adult C57BL/6 wild-type mice.

2.1.6.2 Human cell lines

Transfection with contactin 1 (CNTN1) constructs was performed on human embryonic kidney (HEK) 293 cells purchased from ATCC (ATCC®, Manassas, Virginia, USA, CRL-1573™).

2.1.6.3 Bacterial strains

After ligation of insert and vector DNA, generated plasmids were transformed to NEB5α competent *E. coli* (New England Biolabs, Frankfurt am Main, Germany, C2987I).

2.1.7 Vectors

Table 2.7: Vectors used for cloning

Name	Company	Resistance	Comments
pEGFP-N1	Clontech Laboratories	Kanamycin	Expression of enhanced green fluorescent protein (EGFP)
pRK5	P. Seeburg, MPI for Medical Research, Heidelberg, Germany	Ampicillin	Cytomegalovirus and SP6 promotor

2.1.8 Primers

All primers used for sequencing of CNTN1 or pRK5 plasmid as well as primers for cloning of CNTN1 into pRK5 or pGFP-N1 plasmids are listed in Table 2.1.8. For incorporation of specific substitutions or deletions into the CNTN1 DNA, site-directed mutagenesis with mutagenic forward and reverse primers listed in Table 2.1.8 was performed. All primers were purchased from Invitrogen (Karlsruhe, Germany).

Table 2.8: Primers for sequencing of CNTN1 or pRK5 plasmid and primers for cloning

Primer name	Sequence (5' to 3')
Primers for sequencing	
CNTN1_AS1	GCTTGCCCGTGCCCGGCAGT
CNTN1_AS2	GGTGTATATGTCCTTGAACTGCA
CNTN1_AS3	CCTCTGGTAATGAATATTTGT
CNTN1_AS4	CGTGCTTCCAATGGACAGAGAT
CNTN1_AS5	CCGGTGGATCCCGGGCCCGCGGTA
CNTN1_S1	GGATTTGGACCCATTTTTGA
CNTN1_S2	GGATCGTCCTGAAGTGAA
CNTN1_S3	GCATTTCCTGAATGGGTA
CNTN1_S4	GGAGGAATCTATACATGCT
CNTN1_S5	CCAAGACGATTCTCTCA
CNTN1_S6	GTCACCAGCCAGGAGTACTCA
CNTN1_S7	CTAGCGCTACCGGACTCAGATCTCGAGCTCAAGCTT

Table 2.8: Primers for sequencing of CNTN1 or pRK5 plasmid and primers for cloning, continued

Primer name	Sequence (5' to 3')
Plasmid primers	
pRK5_forward	TAGGTGACACTATAGAATAACATC
pRK5_forward_long	TAGGTGACACTATAGAATAACATCCACTTTGCCTT
pRK5_reverse	GTAACCATTATAAGCTGCAATAAACAAGTT
Primers for cloning	
CNTN1_SalI_AS	ACGCGTCGACTCAAAATTCCGAATAGAAGACAA
CNTN1_delSTOP	ACGCGTCGACTGAAATTCCGAATAGAAGACAAG
CNTN1_sense_GT	CGCGATTGAATTCTGCACGAGGC

Table 2.9: Primers for incorporation of specific substitutions or deletions into CNTN1

Primer name	Sequence (5' to 3')
CNTN1_S1357_N1	GTGGCTTGTGCAGAGCAGCAGAA
CNTN1_AS1383_N1	CTGCTGCTCTGCTCAAGCCACT
CNTN1_S1405_N2	CTTGGAAATCAATCAAATTACAAGAAAT
CNTN1_AS1431_N2	CATTTCTTGTAATTTGATTGATTTCCAAG
CNTN1_S1468_N3	GAGGGAAAGCTCAAAGCACCGGGA
CNTN1_AS1494_N3	GTCCCGGTGCTTTGAGCTTTCCCT
CNTN1_S121_Ig1	GATAAAGGATTTGGATTTGGGTATCTTGACCCCTTT CCTCCTGAG
CNTN1_AS408_Ig1	GTCAAGATACCCAAATCCAAATCCTTTATCCTCCTC AGAAACTCC
CNTN1_S121_Ig2	GATAAAGGATTTGGAAGCAAATTTATACCCCTCATT CCGATACCT
CNTN1_AS684_Ig2	GGGTATAAATTTGCTTCCAAATCCTTTATCCTCCTC AGAAACTCC
CNTN1_S121_Ig3	GATAAAGGATTTGGAGTTCAAGCATTTCCTGAATGG GTAGAGCAT
CNTN1_AS993_Ig3	AGGAAATGCTTGAACTCCAAATCCTTTATCCTCCTC AGAAACTCC

Table 2.9: Primers for incorporation of specific substitutions or deletions into CNTN1, continued

Primer name	Sequence (5' to 3')
CNTN1_S121_Ig4	GATAAAGGATTTGGAATCCTGGCTTTAGCTCCAACT TTTGAAATG
CNTN1_AS1236_Ig4	AGCTAAAGCCAGGATTCCAAATCCTTTATCCTCCTC AGAAACTCC
CNTN1_S121_Ig5	GATAAAGGATTTGGAATCACAAATCCCACACGAATC ATTTTGGCC
CNTN1_AS1545_Ig5	TGTGGGATTTGTGATTCCAAATCCTTTATCCTCCTC AGAAACTCC
CNTN1_S121_Ig6	GATAAAGGATTTGGAGTACGAGGCCCCCCAGGCCCT CCAGGTGGC
CNTN1_AS1818_Ig6	TGGGGGGCCTCGTACTCCAAATCCTTTATCCTCCTC AGAAACTCC

2.1.9 Enzymes

Table 2.10: Enzymes

Enzyme name	Company (Product #)	Application
HotStar HiFidelity DNA Polymerase (2.5 Units/µl)	Qiagen (202602)	PCRs for site-directed mutagenesis of CNTN1
Liberase™ TH Research Grade	Roche (5401135001)	Dissociation of DRGs
Liberase™ TM Research Grade	Roche (5401119001)	Dissociation of DRGs
Pfu DNA Polymerase	Institute of Clinical Neurobiology	Overlap extension PCRs
PNGase F (500.000 Units/ml)	New England Biolabs (P0704)	Removal of *N*-linked glycosylations from CNTN1
RNase A (100 mg/ml)	Carl Roth (7156.1)	Plasmid preparation
T4 DNA Ligase	New England Biolabs (M0202)	Ligation of CNTN1 DNA and vector DNA
Trypsin-EDTA (0.05 %)	Thermo Fisher Scientific (25300054)	Passaging of HEK 293

Table 2.11: Restriction enzymes for DNA cloning

Enzyme name	Recognition sequence 5' to 3'	Buffer	Company (Product #)
EcoRI-HF®	G AATTC	CutSmart®	New England Biolabs (R3101)
SalI-Hf®	G TCGAC	CutSmart®	New England Biolabs (R3138)

2.1.10 Kits

Table 2.12: Kits

Kit	Company (Product #)	Application
Bio-Rad Protein Assay	Bio-Rad Laboratories (5000006)	Quantification of protein amounts in HEK 293 cell lysates
CytoBuster™ Protein Extraction Reagent	Novagen® (71009-4)	Preparation of HEK 293 cell lysates
NucleoBond™ Xtra Maxi	Macherey-Nagel (740414.50)	Plasmid preparation
NucleoSpin® Gel and PCR Clean-up	Macherey-Nagel™ (740609.250)	DNA purification
SuperSignal™ West Femto Maximum Sensitivity Substrate	Thermo Fisher Scientific (34096)	Protein detection by Western Blot analysis
SuperSignal™ West Pico PLUS Chemiluminescent Substrate	Thermo Fisher Scientific (34577)	Protein detection by Western Blot analysis

2.2 Patients

In order to study the pathogenesis of paranodal autoantibodies in neuropathies, material from eight anti-CNTN1 positive patients and two anti-neurofascin (NF) positive patients was investigated. Autoantibodies were detected in laboratories of the Department for Neurology at the University Hospital of Würzburg by enzyme-linked immunosorbent assay (ELISA) and binding assays with murine teased fibers and transfected HEK 293 cells. The median age at disease onset was 65 years (28-76 years). The only patient who was very young (28 years) when symptoms started was diagnosed with anti-NF155 autoantibodies. Six of the patients were male and four were female. Almost all patients showed paresis, most of them in all four limbs. Sensory symptoms like paresthesia or sensory ataxia were also common. Moreover, the patient with NF155 autoantibodies presented with autonomic symptoms like orthostatic hypotension or hyperhidrosis. Titers of autoantibodies varied from 1:250 to 1:30 000. The predominant immunoglobulin G (IgG) subclasses were IgG3 and IgG4, IgG2 was detected at low levels in some of the patients.

Clinical data of all patients are summarized in Table 2.3. For more detailed information about patients 1 to 3, see Doppler et al. (2015), for patient 6, see Appeltshauser et al. (2020). Clinical data of patients 9 and 10 have been published in Stengel et al. (2019). All participants gave written informed consent to take part in the study. The study was approved by the Ethics Committee of the University of Würzburg Medical Faculty.

2.3 Animals

For passive transfer experiments, eight-week-old female Lewis rats were purchased from Charles River Laboratories (Sulzfeld, Germany) and housed in cages with food and water *ad libitium* in the animal facilities of the University of Würzburg (Center for Experimental Molecular Medicine). All experiments were approved by the Bavarian State authorities (Regierung von Unterfranken; license number: 55.2.2-2532-2-593-17).

For *in vitro* cultivation of primary neurons adult wild-type C57BL/6 mice (Charles River Laboratories, Sulzfeld, Germany) were used. Animals were housed in filtertop cages with food and water access *ad libitium* at a 12 h/12 h light/dark rhythm in the animal facilities of the University of Würzburg (Institute for Clinical Neurobiology, Würzburg, Germany; Center for Experimental Molecular Medicine, Würzburg, Germany). All experiments were approved by the local veterinary authority (Veterinäramt der Stadt Würzburg) and the Ethics Committee of Animal Experiments (Regierung von Unterfranken, Würzburg; license number: FBVVL 568/200-324/13).

Table 2.13: Clinical data of seropositive patients

	Patient 1	**Patient 2**	**Patient 3**	**Patient 4**	**Patient 5**	**Patient 6**	**Patient 7**	**Patient 8**	**Patient 9**	**Patient 10**
Age	76	48	61	62	71	75	59	72	71	28
Gender	male	male	female	male	male	female	female	male	male	male
Clinical features	acute tetraparesis, paresthesia, respiratory failure, facial palsy, diplopia	acute tetraparesis, dysesthesia, respiratory failure, action tremor	acute tetraparesis, paresthesia, sensory ataxia, facial palsy, diplopia, rest and action tremor	CNI, neuropathic pain	neuropathic pain	distal tetraparesis, paresthesia, hypoesthesia, areflexia	proximal paresis, cervico-brachialgia, facial palsy	n.a.	pallanaesthesia, distal hypoesthesia, cardiac arrest, locked-in syndrome	tremor, neuropathic pain, orthostatic hypotension, hyperhidrosis
Antigen	CNTN1	CNTN1	CNTN1	CNTN1	CNTN1	CNTN1	CNTN1	CNTN1	pan-NF	NF155
Titer	1:7500 (serum)	1:1500 (PE material)	1:10 000 (serum)	1:19 000 (serum)	1:500 (serum)	1:30 000 (serum)	1:400 (serum)	1:1000 (serum)	*NF155* 1:4000, *NF186* 1:2000 (serum)	1:6000 (serum)
IgG subclass	IgG3 > IgG4	IgG4 >> IgG3	IgG4 >> IgG2	IgG4 > IgG2	IgG4	IgG4 >> IgG2	IgG4	IgG4 > IgG2 >> IgG1	IgG3	IgG4

CNI, cranial nerve involvement; CNTN1, contactin 1; NF, neurofascin; PE, plasma exchange; n.a., not available

2.4 Methods

2.4.1 Passive transfer experiments

In order to study the effect of acute exposure to anti-NF autoantibodies on the sciatic nerve of the rat, passive transfer of IgG from anti-NF positive patients (see 2.2) was performed with eight-week-old female Lewis rats. Figure 2.1 shows the timeline of the passive transfer experiment. All animals were examined in behavioral testings (BTs) and nerve conduction studies (NCS) prior to the first injection of IgG into the sciatic nerve in order to get used to experimental procedures and to create a baseline value. After the second surgery, the two following days were used to repeat BTs and NCS. On the last day of the experiments, rats were sacrificed immediately after NCS and the sciatic nerve was dissected for immunohistochemical analysis.

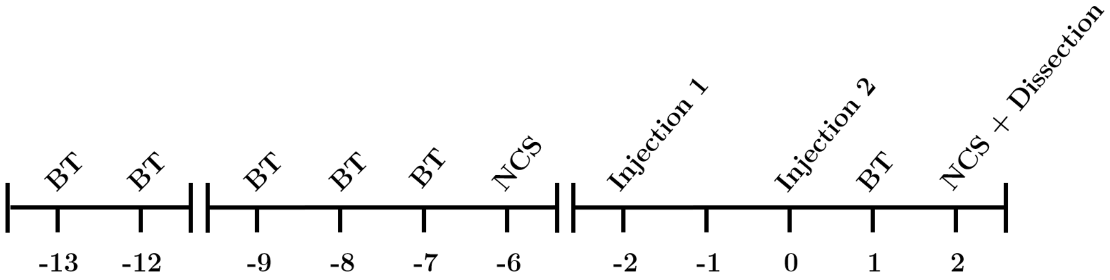

Figure 2.1: Timeline of passive transfer experiments. Behavioral testings (BTs) and nerve conduction studies (NCS) were performed prior to injection on days -13 to -6. Results from BT on day -7 and NCS on day -6 were used as baseline values. On days -2 and 0, purified IgG of anti-NF positive patients or a healthy control was injected into the sciatic nerve. BT and NCS were repeated on day 1 and 2 to analyze potential effects of the passive transfer of anti-NF autoantibodies. At the last day of the experiment, the sciatic nerve was dissected immediately after NCS.

2.4.1.1 Intraneural injection of purified IgG

IgG from anti-NF positive patients was purified by ion exchange chromatography from plasma exchange (PE) material by Susanne Hellmig (AG Schuhmann, Department of Neurology, Würzburg) as described previously (Sommer et al., 2005). For intraneural injection of 10 µl patient or control IgG (100 mg/ml) to the sciatic nerve, rats were anesthetized with 2–2.5 % isoflurane and treated with ketamine (0.1 mg/kg bodyweight) by intraperitoneal (IP) injection for analgesia. After shaving the left pelvic region, the rat was fixed on a polystyrene disk in prone position. By incising the skin at the sciatic notch on the left side and by blunt dissection of the biceps femoris muscle the sciatic nerve was exposed (Fig. 2.2) and patient or control IgG was injected into the nerve with a microsyringe and a 27-gauche needle. The investigator was blinded to the treatment at any timepoint of the experiment. For some animals 25 % human complement serum was added to the purified IgG prior to injection. After the first injection, the wound was sutured with a non-absorbable Dafilon® suture, whereas after the second surgery the biceps femoris muscle was sutured with Silkam® and the wound was closed with a surgical staple.

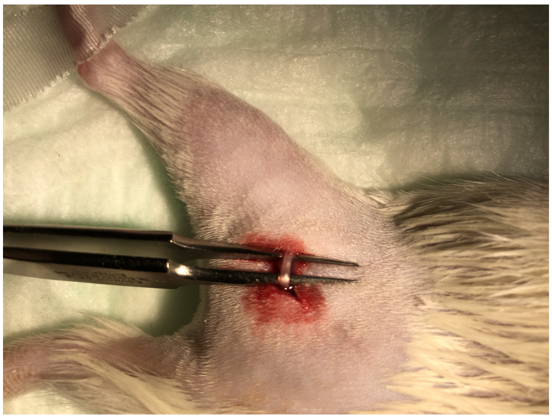

Figure 2.2: Surgical exposure of the sciatic nerve. After skin incision and blunt dissection of the biceps femoris, the sciatic nerve was surgically exposed for subsequent intraneural injection of purified IgG from anti-NF positive patients.

2.4.1.2 Behavioral testings

Behavioral testings were performed before and after injection of IgG (Fig. 2.1) and included motor skill tests, gait analysis with the CatWalk™ XT system as well as nociception assays in order to test the sensory function of the rats.

Motor skill assessment

For motor skill assessment, animals were placed on a motorized rotating drum using the RotaRod Advanced system. Rotation speed accelerated constantly from an initial speed of 5 rpm to an end speed of 50 rpm within 500 s. The latency until the animal falls down from the drum was recorded automatically by an infrared beam in the system. For each rat the mean latency of three trials per test day was calculated. In order to compare patient and control animals, the ratio of fall latencies before and after injection of IgG was determined.

Gait analysis

The CatWalk™ XT system is a tool which allows quantitative gait analysis of an animal. It consists of a glass walkway and a high-speed camera with high temporal and spatial resolution recording the animal traversing the walkway. The system uses the Illuminated Footprints™ technology where a green LED light is internally reflected within the whole glass plate. Only where the rat touches the glass, light is scattered depending on the intensity of footprint. This light signal is then captured by the camera and footprints are analyzed automatically by the Catwalk™ XT software.

Analyzed parameters included the average speed by which the animal traverses the walkway, the maximum contact area and the maximum intensity of the treated left hindpaw. Furthermore, stride length (distance between two consecutive footprints of the same paw), step cycle (duration between two consecutive footprints of the same paw), swing time (time, where the paw is lifted), standing time (time, where the paw touches the glass plate) and print area (area of the whole footprint) of the left hindpaw were investigated (Fig. 2.3).

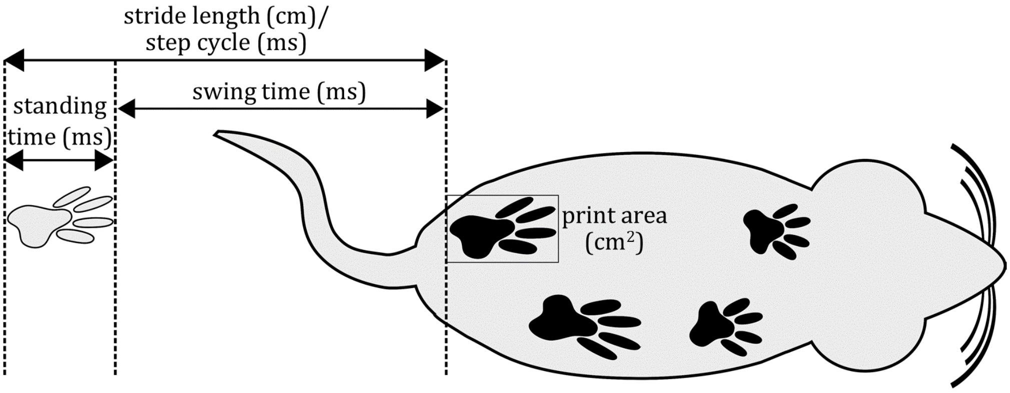

Figure 2.3: Parameters analyzed by the CatWalk™ XT system. Gait analysis in passive transfer experiments was performed by assessing stride length (cm), step cycle (ms), swing time (ms), standing time (ms) and the print area (cm^2) of the left hindpaw.

Sensory function

Mechanical sensitivity was evaluated in a von Frey test where each rat was placed into an acrylic glass box on a wire grid. After adaption to the environment for 30 min, the first von Frey filament (Stoelting, Wood Dale, Illinois, USA) with a force of 15 g was placed on the plantar surface of the right and the left hindpaws until it bent. If the rat reacted to the stimulus by withdrawing its paw the next thinner von Frey filament was tested, if it did not show any reaction the next thicker filament was applied. Each hindpaw was tested six times based on Dixon's staircase system. The 50 % withdrawal threshold was calculated via equation 2.1, where X is the log of the force of the final von Frey filament, k is a tabular value from Dixon (1965) and d is the increment between the tested von Frey filaments.

$$50\,\%\ withdrawal\ threshold\ (g) = \frac{10^{(X+kd)}}{10000} \tag{2.1}$$

Sensitivity to thermal stimulation was tested in a plantar test with a Hargreaves Apparatus (Ugo Basile®, Gemonio, Italy). Here again, rats were placed into individual acrylic glass boxes where they adapted to the environment for 30 min. After that, a radiant heat stimulus with an infrared intensity of 25 was applied to the right and the left hindpaw. The latency until the stimulus exceeded the pain threshold of the rat and therefore it withdrew its hindpaw was measured automatically by a fiber optic sensor. For comparison of thermal sensitivity, the mean value of three measurements before and after injection was calculated.

2.4.1.3 Nerve conduction studies

Previously, it had been shown that passive transfer of CNTN1 IgG 3 autoantibodies to the sciatic nerve of rats induces conduction blocks (Doppler et al., 2019). Moreover, conduction alterations were also observed after intrathecal injection of anti-NF autoantibodies (Manso et al., 2019). In order to study the effect of intraneural injection of anti-NF on the nerve conduction, rats were anesthetized with a mixture of xylavet (xylazine: 8 mg/kg body weight) and ursotamin (ketaminhydrochloride: 100 mg/kg body weight) by intraperitoneal injection. In contrast to isoflurane, xylavet and ursotamin do not affect F-wave parameters (Nowicki et al., 2014).

Animals were fixed on a polystyrene disk in prone position and body temperature was kept constantly at 34–36 °C using a heating lamp. Neurographic recordings from the right and left sciatic nerve were performed by using a digital Neurosoft Evidence 3102 electromyograph as described before (Zielasek et al., 1996). Monopolar needle electrodes were placed at the ankle or at the sciatic notch for distal and proximal stimulation, respectively. Recording electrodes were placed at the hindpaw between the third and fourth toe and at the first toe.

Distal as well as proximal compound muscle action potential (CMAP) amplitudes [mV] and latencies [s] were measured after supramaximal stimulation. Nerve conduction velocity (NCV) [m/s] was calculated by measuring the distance [m] between stimulation and recording electrodes and dividing it by the latency. In addition, F-wave and H-reflex latencies and persistences were measured after ten supramaximal stimuli at frequencies of 0.3 Hz, 1 Hz and 10 Hz. Mixed afferents were investigated by placing the stimulation electrodes at the ankle and the recording electrodes at the sciatic notch. Again, NCV was calculated by dividing the distance of stimulating and recording electrode by the latency.

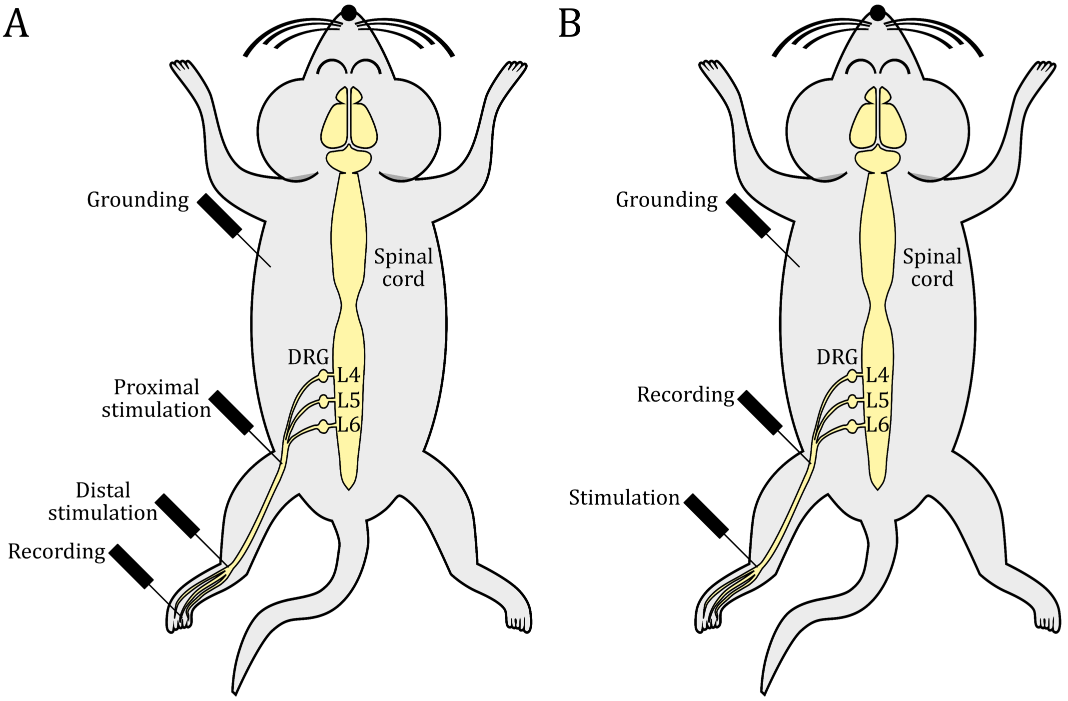

Figure 2.4: Needle electrode placement for NCS. (A) For motor neurographies, the stimulation electrode was placed at the ankle for distal stimulation or at the sciatic notch for proximal stimulation. F-wave and H-reflex studies were performed by supramaximal distal stimulation at the ankle. The recording electrode was placed between the third and fourth toe. A ground electrode was placed for providing a reference point. (B) For studies of mixed afferents, the stimulation electrode was placed at the ankle and the recording electrode was placed at the sciatic notch.

2.4.1.4 Sciatic nerve dissection

Immediately after NCS, rats were sacrificed by decapitation and the sciatic nerve was dissected and cut into three pieces. The proximal part of the nerve was embedded in Tissue-Tek® OCT compound, frozen in liquid nitrogen and stored at −80 °C. The middle part of the nerve was prefixed in 4 % paraformaldehyde (PFA) for 10 min at room temperature (RT), washed 3 × in phosphate buffer before teasing single nerve fibers on slides with forceps. Teased fibers were stored at −20 °C until staining. The distal part of the sciatic nerve was fixed in 4 % PFA/glutaraldehyde.

2.4.1.5 Immunohistochemistry of the sciatic nerve

In order to ensure binding of purified IgG from anti-neurofascin positive patients to rat sciatic nerves, a binding assay with teased fibers was performed. After fixing the fibers in acetone for 10 min at −20 °C, samples were washed in 0.1 M phosphate buffered saline (PBS). Unspecific binding sites were blocked in a solution containing 4 % normal goat serum (NGS), 4 % fetal bovine serum (FBS) and 0.3 % Triton X-100 in PBS for 1 h in a humidity chamber at RT. After removing the blocking solution, sciatic fibers were incubated with purified IgG or serum of healthy controls at a dilution of 1:500 in the blocking solution overnight at 4 °C. Human IgG or serum was removed by washing the samples 3 × in PBS. Secondary antibodies (Cy™3 AffiniPure goat anti-human IgG (H+L)) were then applied to the sciatic fibers at a dilution of 1:100 in blocking solution for 1 h at RT in the dark. After three washing steps with PBS, sciatic nerve fibers were embedded in VECTASHIELD Antifade Mounting Medium with DAPI and analyzed by fluorescence microscopy.

For analysis of autoantibody binding to the sciatic nerve from rats which were treated with IgG from seropositive patients or a healthy control in passive transfer experiments, teased fibers were stained the same way as described before but without primary antibodies.

Furthermore, co-stainings of contactin associated protein (Caspr) and pan voltage-gated sodium (Na_V) were performed on teased fibers from passive transfer experiments to label the paranodal and nodal region, respectively. The same protocol was used as described before with primary antibodies against Caspr and pan Na_V at a dilution of 1:250. Appropriate secondary antibodies (Alexa Fluor® 647 AffiniPure donkey anti-rabbit IgG (H+L), Alexa Fluor® 488 AffiniPure goat anti-mouse IgG (H+L)) were used at a dilution of 1:100 for fluorescent labelling.

2.4.2 Analysis of CNTN1 and pan Na_V in DRG neurons

As CNTN1 interacts with voltage-gated sodium channels via their β subunit and enhances channel density at the plasma membrane in DRG neurons (Rush et al., 2005), the effect of anti-CNTN1 autoantibodies on sodium currents in DRG neurons was investigated.

2.4.2.1 Primary culture of DRG neurons

Cells for electrophysiological and structured illumination microscopy (SIM) measurements were obtained by isolating DRGs from adult C57BL/6 wild-type mice. After sacrificing the mice by overdose exposure to CO_2 or isoflurane, DRGs were dissected as described before (Sleigh et al., 2016). In short, the spinal column was cut dorsally into two halves and DRGs were pulled out of the invertebral foramen after removing the spinal cord. Anterior and posterior nerve roots were cut off and DRGs were transferred into ice-cold Dulbecco's Modified Eagle Medium/Nutrient Mixture F-12 (DMEM/F-12) with GlutaMAX™ supplement. By incubating DRGs with Liberase™ TH Research Grade at a collagenase concentration of 1.92 mg/ml and a high concentration of thermolysin for 30 min at 900 revolutions per minute (rpm) and 37 °C in a ThermoMixer® comfort, cells get detached from each other. Following another incubation step with Liberase™ TM Research Grade at the same collagenase concentration but with a medium concentration of thermolysin for 10 min at 900 rpm and 37 °C, cells were triturated in DRG medium consisting of 89 % DMEM/F-12 with GlutaMAX™ supplement, 10 % FBS, penicillin (10 000 U/ml)/streptomycin (10 000 µg/ml) and 100 ng/ml nerve growth factor-7S (NGF). DRG neurons were then seeded on coverslips which were coated with poly-D-lysine (0.1 mg/ml) for 1 h at RT and placed in the incubator at 37 °C and 5 % CO_2.

2.4.2.2 Incubation of DRG neurons with serum of patients

1 d old DRG neurons were incubated with anti-CNTN1 positive serum or PE material of patients 1, 2 or 3 or serum of three healthy controls for different time intervals (Fig. 2.5) prior to patch-clamp measurements. For this, cells were transferred into 24-well cell culture plates and incubated with serum or PE material at a dilution of 1:250 in DRG medium for 1 h, 2 h, 24 h, 48 h and 72 h in the incubator at 37 °C and 5 % CO_2.

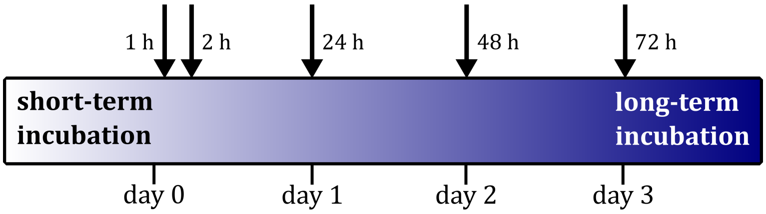

Figure 2.5: Incubation of DRG neurons prior to electrophysiological recordings. 1 d after seeding DRG neurons were incubated with serum or PE material of patients 1, 2 or 3 or serum of a healthy control for 1 h, 2 h, 24 h, 48 h and 72 h.

2.4.2.3 Whole-cell recordings of DRG neurons

After incubation of DRG neurons with patients' or controls' material for specific periods of time, whole cell recordings of sodium currents were performed. For this, coverslips with DRGs were transferred into a recording chamber filled with bath solution containing 70 mM NaCl, 70 mM choline chloride, 3 mM KCl, 1 mM $MgCl_2$, 1 mM $CaCl_2$, 20 mM TEA-Cl, 5 mM CsCl, 0.1 mM $CdCl_2$ and 10 mM HEPES and adjusted to pH 7.3 with NaOH and to an osmotic concentration of 320 mOsm/l with glucose. The internal solution consisted of 140 mM CsF, 1 mM EGTA, 10 mM NaCl and 10 mM HEPES with a pH adjusted to 7.3 with NaOH and 310 mOsm/l adjusted with glucose and was filled in recording pipettes produced from borosilicate glass capillaries with a resistance of about 5 MΩ pulled with a micropipette puller. Patch clamp measurements were controlled with the PATCHMASTER software (HEKA, Lambrecht, Germany) and sodium current signals were amplified using an EPC-10 amplifier. Currents were filtered at 2.9 kHz and recorded in the whole-cell configuration with depolarization steps of 10 mV from −80 mV to +60 mV at a holding potential of −70 mV. All experiments were carried out at RT.

2.4.2.4 Immunocytochemistry of primary neurons

In order to ensure binding of patients' serum to DRG neurons, which were analyzed by the patch clamp technique, immunocytochemistry was performed. After fixing cells in 4 % PFA for 20 min, neurons were washed in PBS 3 × for 5 min. Following a blocking step for 20 min with 10 % bovine serum albumin (BSA) in PBS, secondary antibodies (Cy™3 AffiniPure Goat Anti-Human IgG (H+L)) were added to the cells at a dilution of 1:100 in 2 % BSA/PBS and incubated for 1 h at room temperature in the dark. After that, cells were washed again in PBS 3 × for 5 min and were embedded in VECTASHIELD Antifade Mounting Medium with DAPI.

Double stainings of CNTN1 and pan $\mathrm{Na_V}$ for SIM measurements were performed in a similar way. After long-term incubation of DRG neurons with patients' or controls' material for 72 h, cells were blocked for 20 min in 10 % BSA/PBS and incubated with a commercial antibody to CNTN1 (1:250) for 1 h in the incubator at 37 °C and 5 % CO_2. Then, cells were washed once for 5 min in PBS before fixing them in 4 % PFA for 20 min. After washing 3 × in PBS, cell membranes of DRG neurons were permeabilized with 0.1 % Triton X-100 for 20 min. Thereafter a primary antibody to pan $\mathrm{Na_V}$ was added at a dilution of 1:250 overnight at 4 °C. Another washing step with PBS (3 × 5 min) ensured that any unbound antibody was removed from the cells. Incubation with appropriate secondary antibodies (donkey anti-goat AF488, goat anti-mouse ATTO-643) was performed at a dilution of 1:250 in 2 % BSA/PBS for 1 h at RT in the dark. After removing unbound antibodies by washing 3 × for 5 min in PBS, DRG neurons were embedded in ProLong™ Glass Antifade Mountant.

2.4.2.5 Structured illumination microscopy

In light microscopy, resolution is diffraction-limited to about 200 nm because of the wave nature of light which has first been described by Ernst Abbe in the nineteenth century (Abbe, 1873). However, over the last decades, different methods have been developed to overcome this limit. One of these methods is SIM which uses structured illumination of the sample, a principle already known since 1963 (Lukosz and Marchand, 1963). Years later, the technique was developed and applied to biological samples (Gustafsson et al., 2003). In SIM, excitation laser light passes an optical grating (Fig. 2.6, A) leading to sinusoidal striped illumination patterns of high spatial frequencies (Schermelleh et al., 2010; Wegel et al., 2016). The interaction of the sample's fluorescence emission and the excitation pattern produces moiré fringes (Fig. 2.6, B). Those coarser moiré fringes have a lower spatial frequency than the finer high frequency sample and illumination patterns and therefore can be transmitted by a normal objective lens. Multiple images are acquired while rotating and shifting the optical grating. Subsequently, all images are processed by a complex computer algorithm capable of recalculating the information of the moiré patterns to the original highly resolved information of the specimen. With this method a two-fold higher resolution in lateral as well as in axial direction can be achieved compared to conventional wide-field microscopy (Schermelleh et al., 2008).

In order to investigate CNTN1 and sodium channel distribution in DRGs after incubation with serum or PE material of anti-CNTN1 positive patients or serum of healthy controls, double stainings (see 2.4.2.4) were recorded on a commercial SIM Zeiss ELYRA S.1 system. The system was equipped with a Plan-Apochromat 63x/1.40 oil immersion objective and four excitation lasers where the 488 nm OPSL laser was used for excitation of AF488 and the 642 nm diode laser for excitation of ATTO-643. Image stacks were recorded with structured illumination of five rotational and five phase variations. System operation and processing of the obtained image stacks was performed with the ZEN 2.1 black software.

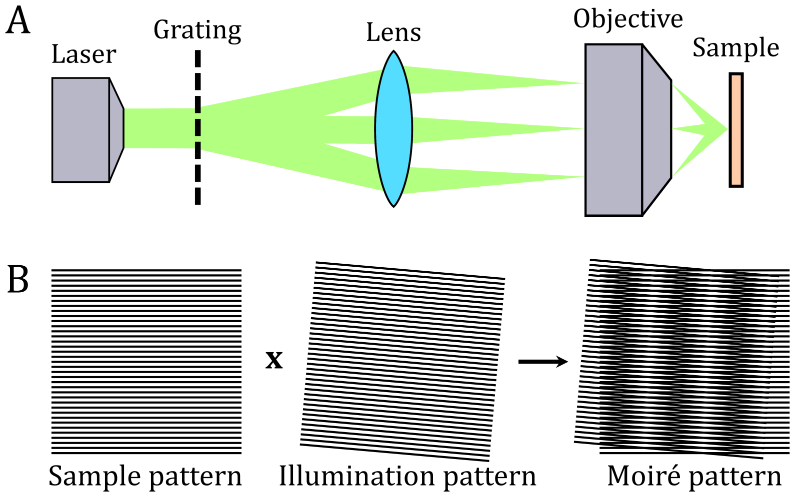

Figure 2.6: Principle of SIM. (A) Simplified scheme of a SIM setup. An optical grating in front of the lens leads to sinusoidal striped illumination of the sample. (B) Superposition of two fine patterns with high spatial frequencies results in a coarser moiré pattern with lower spatial frequencies.

2.4.3 Epitope mapping of anti-CNTN1 autoantibodies

A previous study showed that the epitope of CNTN1 autoantibodies is located at *N*-linked glycans which represent posttranslational modifications of the protein (Labasque et al., 2014). In contrast, another study identified the protein core of CNTN1 as the binding site of autoantibodies and not the *N*-glycans (Miura et al., 2015). In order to find the epitope for anti-CNTN1 positive patients in this cohort, the CNTN1 DNA was modified by polymerase chain reaction (PCR) mutagenesis to remove specific glycosylation sites. In addition, digestion of the CNTN1 protein with peptide-*N*-glycosidase F (PNGase F) was used to determine if *N*-linked glycans play a role in the protein recognition by autoantibodies. Furthermore, whole immunoglobulin (Ig) domains were deleted from the protein to detect the binding site of patients' autoantibodies.

2.4.3.1 Site-directed mutagenesis

All primers used for PCR mutagenesis and sequencing are shown in 2.1.8. In general, primers for introducing mutations were about 25 nucleotides long, primers for deletion of whole domains were 45 nucleotides long.

For PCR mutagenesis rat CNTN1 DNA (GenBank™ accession number D38492) was used. A sequence similarity of 95 % between rat CNTN1 and human CNTN1 at the amino acid level makes the DNA suitable for the experiments. As the expression vector was unknown, CNTN1 was first cloned into a pRK5 vector by introducing a SalI restriction site at the end of the CNTN1 DNA. This was achieved by running a PCR (Tables 2.14 and 2.15) with the forward primer "pRK5_forward" and the reverse primer "CNTN1_SalI_AS" containing the desired restriction site sequence. Then, the DNA was cut at the restriction sites EcoRI at the beginning of the cDNA and SalI at the end of the cDNA and ligated into the vector pRK5 which was cut with the same restriction enzymes. Transformation into *E. coli* and plasmid preparation led to high amounts of DNA used for site-directed mutagenesis experiments.

To remove specific *N*-linked glycosylation sites from CNTN1 the DNA sequence was modified via PCR mutagenesis. As *N*-linked glycosylations are always attached to an asparagine (Asn–X–Ser/Thr) of the protein, specific recognition signals of the DNA sequence were changed in a way that not asparagine but glutamine was integrated in the polypeptide chain. Glutamine is chemically similar to asparagine and therefore does not affect the overall structure of the protein. To introduce a mutation, site-directed mutagenesis was performed by using custom designed forward and reverse primers containing the desired mutation in a two-step PCR (Fig. 2.7, A).

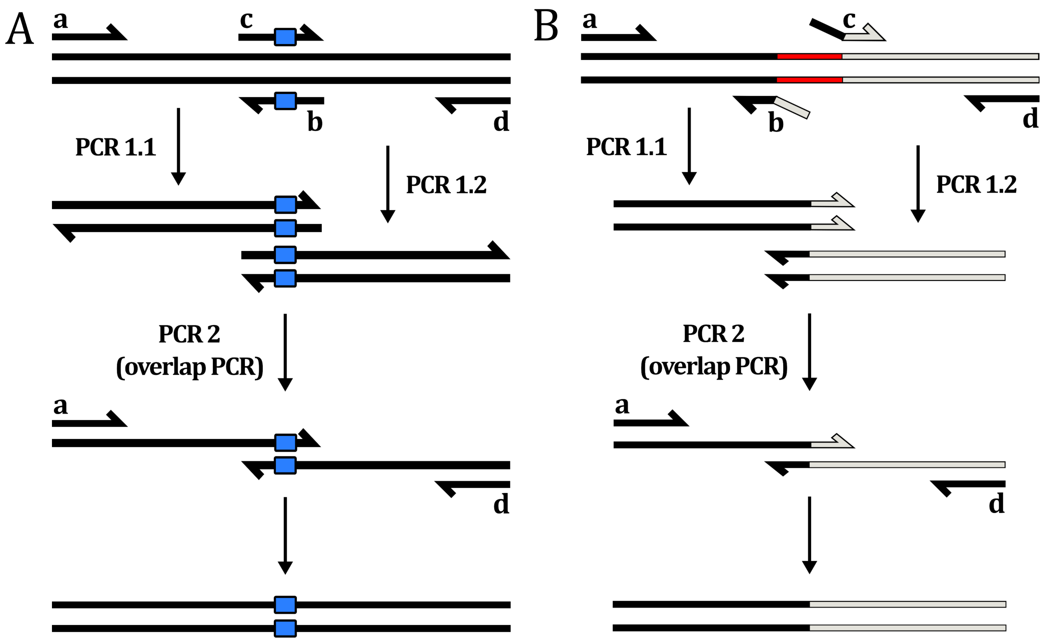

Figure 2.7: Principle of site-directed mutagenesis. (A) Integration of a mutation is achieved in a two-step PCR. In the first PCR a forward and a reverse primer containing the desired mutation (c and b, respectively) are annealed to the DNA template in two different PCR reactions (PCR 1.1 and 1.2). The DNA fragment is amplified by using appropriate flanking primers (a, d). The overlapping products of PCR 1.1 and 1.2 are annealed in the second PCR (PCR 2, overlap PCR) and amplified by adding the flanking primers a and d. The generated DNA sequence contains the desired mutations. (B) Deletion of a specific part from the DNA was performed by using forward and reverse primers complementary to the DNA region before and after the sequence to be deleted (c and b) in two PCR reactions (PCR 1.1 and 1.2). Again, the DNA fragments were amplified by flanking primers (a and d) and overlapping DNA fragments were combined in a second PCR step.

In the first step, forward and reverse mutant primers are used in two different PCR reactions to generate two DNA fragments with overlapping ends. For introducing a mutation at the glyosylation site at position 457 (amino acid level), the forward mutant primer “CNTN1_S1357_N1” was used with the reverse flanking primer “CNTN1_SalI_AS” at the end of the cDNA in the PCR 1.1. For PCR 1.2 the reverse mutant primer “CNTN1_AS1383_N1” was used with the forward primer “pRK5_forward_long” (Fig. 2.8). In an overlap extension PCR, which is the second step, the overlapping ends of the products from PCR 1.1 and PCR 1.2 were annealed. Amplification of the product with flanking primers “pRK5_forward_long” and “CNTN1_SalI_AS” led to the complete DNA sequence containing the desired mutation. Introduction of the mutation for deleting the N-linked glycosylation site at position 473 was achieved in the same way but using mutagenic primers “CNTN1_S1405_N2” together with “pRK5_reverse” and “CNTN1_AS_1431_N2” together with “pRK5_forward”. For introducing a mutation at site 494 (amino acid level), the mutagenic primers “CNTN1_S1468_N3” together with “CNTN1_SalI_AS” and “CNTN1_AS1494_N3” together with “pRK5_forward_long” were used. Amplification of the PCR products was performed in an overlap extension PCR with primers “pRK5_forward_long” and “CNTN1_-

SalI_AS" as described before. Introduction of further mutations was performed by using the produced mutagenic CNTN1 DNA with the same mutagenic and flanking primers in order to establish the constructs of CNTN1 with two mutated glycosylation sites (CNTN1_N457,473Q; CNTN1_N457,494Q; CNTN1_N457,473,494Q) and the triple mutant CNTN1_N457,473,494Q (Fig. 2.9, A).

Figure 2.8: Sequence of CNTN1 with mutagenic primers. PCR mutagenesis was performed by using forward and reverse primers containing the desired mutation at the glycosylation sites 457, 473 and 494 (amino acid level)

PCR mutagenesis was also used for deletion of Ig domains from the CNTN1 protein in the same way as described before but, instead of primers containing mutations, forward and reverse primers complementary to the region before and after the desired deletion were used (Fig. 2.7, B). Before deleting whole domains from CNTN1, the insert was cloned into a peGFP-N1 vector to verify expression of the protein in the transfected cells by eGFP co-expression. Therefore, the stop codon at the end of the CNTN1 DNA was removed by using the primer "CNTN1_delSTOP" and a mutation was inserted at the beginning of the gene with the primer "CNTN1_sense_GT" in one PCR in order to ensure in-frame cloning into the new vector.

Deletion of the first Ig domain was then achieved by using the primers "CNTN1_S121_Ig1" together with "CNTN1_AS5" in the PCR reaction 1.1 and the primers "CNTN1_AS408_Ig1" with "CNTN1_S7" in the PCR 1.2. Again, the two PCR products were annealed and amplified in an overlap extension PCR with the flanking primers "CNTN1_S7" and "CNTN1_AS5". Deletion of the other Ig domains was performed in the same way with appropriate mutagenic primers (see 2.1.8). After site-directed PCR mutagenesis, the constructs CNTN1_del_Ig1, CNTN1_del_Ig1,2, CNTN1_del_Ig1,2,3, CNTN1_del_Ig1-4, CNTN1_del_Ig1-5 and CNTN1_del_Ig1-6 were available for further investigation (Fig. 2.9, B). All PCRs for mutagenesis were performed with the HotStar HiFidelity DNA polymerase possessing proofreading activity. The PCR reaction mixture and the PCR program are shown in Tables 2.14 and 2.15.

Table 2.14: Standard PCR reaction mixture

Reagent	Volume [µl]
5x HotStar HiFidelity PCR Buffer (incl. dNTPs)	10
5x Q-solution	10
Forward primer (10 pmol/µl)	5
Reverse primer (10 pmol/µl)	5
HotStar HiFidelity DNA polymerase (2.5 Units/µl)	1
RNase free water	18
Template DNA (100 ng/µl)	1

Table 2.15: PCR standard protocol

Step	Temperature [°C]	Time [min:s]
Initial activation step	95	02:00
Denaturation	94	00:10
Annealing	depending on primer	01:00
Extension	68	02:00
Final extension step	72	10:00
End of PCR cycling	4	indefinite
30 cycles of steps 2-4		

Overlap extension PCRs for combining the two DNA fragments generated in the first PCRs were performed with Pfu DNA polymerase which has proofreading activity. The overlap extension PCR was executed with the reaction mixture (Table 2.16) in three cycles each consisting of 5 min at 95 °C, 5 min at 55 °C and 5 min at 72 °C. Afterwards, 1 µl of the forward and 1 µl of the reverse flanking primer were added to the mixture and the PCR standard protocol (see Table 2.15) was started.

Table 2.16: Overlap Extension PCR reaction mixture

Reagent	Volume [µl]
DNA fragment I	5
DNA fragment II	5
dNTPs (10 mM)	2
10x Pfu buffer	10
Pfu polymerase	6.6
RNase free water	69.4

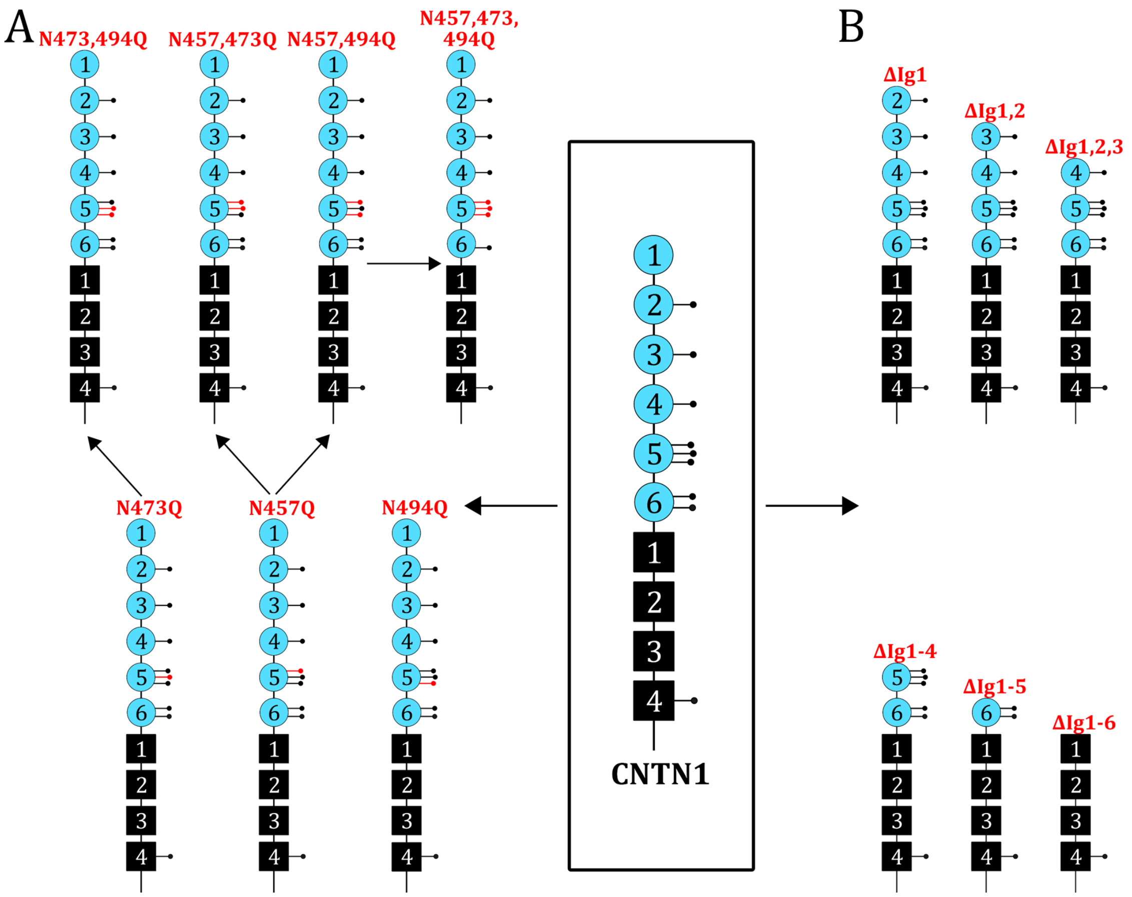

Figure 2.9: Constructs of CNTN1 established by PCR mutagenesis. Rat CNTN1 was used for site directed mutagenesis. (A) Specific *N*-glycosylation sites (red) were removed from the protein by PCR mutagenesis using mutagenic primers harboring the desired mutation. At the amino acid level glutamine instead of asparagine gets incorporated into the protein at the mutagenic site which is not glycosylated posttranslationally. (B) Deletion of whole Ig domains was achieved by using mutagenic primers complementary to the region before and after the Ig domain to be deleted.

2.4.3.2 Agarose gel electrophoresis

To separate DNA fragments, a 1 % agarose gel was prepared by dissolving 1.5 g agarose in 150 ml Tris-borate-EDTA (TBE) buffer in a microwave. After adding 10 µl Midori Green to the liquid gel to stain the DNA, the agarose gel was poured into a gel tray and a comb was added to produce sample loading wells. After cooling down and hardening of the gel, it was transferred into a horizontal gel electrophoresis chamber which was filled with TBE buffer. A color marker was added to the DNA samples prior to loading. Additionally, a DNA ladder was loaded for size comparison. After the electrophoresis was performed at 140 V for 40 min, bands were visualized under UV light. For purification of PCR products, samples were loaded in duplicates where the first desired DNA band was cut out of the gel under UV light and the second one was cut out at the same position in order to eliminate risk of DNA damage caused by UV radiation.

2.4.3.3 DNA purification

Purification of DNA fragments from agarose gels was performed by using the NucleoSpin™ Gel and PCR Clean-up Kit according to the manufacturer´s instructions. For 100 mg gel containing the DNA, 200 µl buffer NTI were added and heated to 50 °C until the complete gel was dissolved. 700 µl were then loaded on a NucleoSpin™ Gel and PCR Clean-up column placed in a 1.5 ml tube prior to centrifugation for 1 min at 11 000 x *g*. In this step, the DNA binds to the silica membrane of the column. The membrane was then washed twice each time with 700 µl buffer NT3 and centrifugation at 11 000 x *g* for 1 min after each step. To dry the silica membrane another centrifugation step is added. Then, the DNA was eluted from the membrane by incubation with 30 µl buffer NE for 2 min followed by centrifugation for 1 min at 11 000 x *g*. The buffer was preheated to 70 °C to improve DNA recovery. 2 µl of the purified DNA were analyzed by agarose gel electrophoresis (see 2.4.3.2).

2.4.3.4 Restriction digest

Insertion of amplified DNA into the desired vector was achieved by restriction enzyme digest of both, the DNA and the vector, with the same restriction enzymes in order to produce overlapping "sticky ends". High fidelity restriction enzymes (EcoRI-HF® and SalI-HF®) were used because of 100 % activity in CutSmart buffer and reduced star activity. Each DNA was digested with 1-5 Units of restriction enzyme for 1 h at 37 °C. Thereafter, agarose gel electrophoresis was performed (2.4.3.2) and the digested DNA and vector fragments were cut out of the gel and purified (2.4.3.3).

2.4.3.5 Ligation

Ligation of the digested vector and the DNA fragment was performed in a 1:7 ratio. The reaction mix containing 7 µl digested DNA fragment, 1 µl digested vector, 1 µl 10 x T4 DNA ligase buffer and 1 µl T4 DNA ligase was incubated for 1 h at RT.

2.4.3.6 Transformation

Subsequently after ligation (2.4.3.5), the generated plasmid DNA was used for transformation of competent NEB5-alpha *E. coli* cells. 5 µl of the ligation mixture were added to 200 µl competent cells and incubated for 30 min on ice before heat-shocked for 45 s at 42 °C. After 2 min on ice, 500 µl prewarmed 2x YT medium was added and the mixture was incubated for 1 h at 37 °C and 400 rpm. Depending on the resistance of the plasmid 50 µl or 200 µl of the cells were plated on 2x YT plates containing the appropriate antibiotic (100 mg/ml, ampicillin or kanamycin) and incubated overnight at 37 °C. For plasmid preparation, 4 ml 2x YT medium with the appropriate antibiotic (100 mg/ml) was inoculated with single colonies and grown overnight at 37 °C and 180 rpm.

2.4.3.7 Plasmid preparation

In order to extract plasmid DNA out of the bacterial culture, cells were lysed under alkaline conditions where plasmid DNA remains stable but chromosomal DNA and protein are denatured. 3 ml of each culture were centrifuged for 3 min at 13 000 rpm and the supernatant was removed from the cell pellet. Afterwards, 200 µl of cold buffer P1 and 4 µl of RNase A (10 mg/ml) was added, cells were resuspended by shortly vortexing, and the mixture was incubated for 5 min on ice. Thereafter, 400 µl of buffer P2 were added. The mixture was gently inverted and incubated for 5 min on ice. Then, 300 µl of buffer P3 were added which was again incubated for 5 min on ice. Lysed cells were centrifuged for 5 min at 15 000 rpm and 4 °C and 800 µl of the supernatant were transferred into a new reaction tube. 800 µl isopropanol were added, gently mixed and incubated for 5 min at RT. Centrifugation at 13 000 rpm for 5 min led to a pellet of the plasmid DNA which was washed once with 300 µl 70 % EtOH. After drying the pellet for about 15 min at 37 °C, it was resuspended in 40 µl TE buffer (pH 8.0). 2 µl were used for control digestion (2.4.3.4) following agarose gel electrophoresis (2.4.3.2).

Higher amounts of DNA were produced by inoculating 250 ml 2x YT medium containing the appropriate antibiotic (1:100) with a small amount of the bacterial culture and growing the cells overnight at 37 °C. Plasmid DNA was extracted from the bacteria with the NucleoBond® Xtra Maxi kit according to the manufacturer's instructions. In short, cells were centrifuged for 20 min at 4000 x *g* and the supernatant was discarded. Then, the pellet was resolved in 12 ml buffer RES + RNase before adding 12 ml lysis buffer. The sample was inverted five times and incubated for 5 min at RT. Afterwards, 12 ml buffer NEU were added and the sample was inverted until the color changed from blue to colorless. After equilibrating the column and filter with 25 ml buffer EQU, the lysate was loaded on the column filter and the filter was washed with 15 ml buffer EQU. The filter was then discarded and another washing step of the column with 25 ml buffer WASH followed. Elution of the plasmid DNA from the column was achieved by adding 15 ml buffer ELU. 10.5 ml isopropanol were added for precipitation of the DNA. Subsequently, the sample was centrifuged at 15 000 x *g* at 4 °C for 20 min. After washing with 5 ml 70 % ethanol and centrifuging at 15 000 x *g* and RT for 5 min, the supernatant was discarded and the pellet was allowed to dry. The dried pellet was then resuspended in 500 µl buffer TE, the concentration was adjusted to 1 µg/µl and the DNA was stored at −20 °C until further use.

2.4.3.8 Determination of DNA concentration

Plasmid DNA concentration was measured by using a NanoDrop™1000 spectrophotometer. Prior to measurements, a blank (2 µl TE buffer pH 8.0) was loaded and measured to calibrate the system. After removing the blank, 2 µl of the sample were loaded, the concentration was measured and adjusted to 1 µg/µl with TE buffer pH 8.0.

2.4.3.9 Sequencing

To verify if the mutagenesis was successful, samples of the generated plasmid DNA were sent together with custom primers to Eurofins Genomics (Ebersberg, Germany). According to the company's instructions, 15 µl of each plasmid DNA, where the concentration was adjusted to 100 ng/µl with nuclease-free water, and 15 µl of each primer at a concentration of 10 pmol/µl were required for sequencing.

2.4.3.10 Preparation of HEK 293 cell lysates

Lysates of HEK 293 cells transiently transfected with CNTN1 (see 2.4.3.16) were prepared by using the CytoBuster™ Protein Extraction Reagent. In the first step, medium was aspirated and cells were washed once with PBS. Afterwards, 1 ml of the reagent was added and incubated for 5 min at RT. By scraping the cells with a cell scraper, the maximum amount of cells was harvested. The extract was then transferred to a reaction tube and centrifuged at 16 000 x *g* and 4 °C for 5 min. The supernatant was again transferred into a new reaction tube and stored at −80 °C until further use.

2.4.3.11 Bradford method for protein quantification

Quantification of protein amounts in HEK 293 cell lysates (2.4.3.10) was performed using the Bradford assay. This technique relies on the binding of Coomassie Brilliant Blue G-250 to proteins which results in the unprotonated blue form of the dye with an absorbance maximum (A_{max}) at 595 nm. In contrast, unbound Coomassie Brilliant Blue G-250 in the Bradford reagent is red ($A_{max} = 470$ nm). Thus, the protein amount directly correlates with the absorbance of the reagent at 595 nm which can be measured with a photometer. Prior to measurements, protein standards of BSA in the dye reagent with different concentrations (1 µg/ml, 2.5 µg/ml, 5 µg/ml, 10 µg/ml, 15 µg/ml and 25 µg/ml) were prepared to measure a standard curve. 1 ml of undiluted dye reagent was used as blank. For measurements of the protein amount in HEK 293 cell lysates, 1 µl of the sample was mixed with 999 µl of the dye reagent and incubated for 5 min at RT.

2.4.3.12 PNGase F digestion

In order to determine if *N*-linked glycosylations are involved in the recognition of CNTN1 by the autoantibodies of anti-CNTN1 positive patients, all *N*-linked glycosylated sugar chains were removed from the protein using the enzyme PNGase F. This enzyme is an amidase that cleaves between the innermost *N*-acetylglucosamine and asparagine of the protein (Fig. 2.10). Digestion with PNGase F was performed as indicated by the manufacturer. In the first step, 10 µg of protein from HEK 293 cell lysates (2.4.3.10) were incubated with 1 µl glycoprotein denaturing buffer (10x) for 10 min at 100 °C. Afterwards, deglycosylation was performed by adding 2 µl glycobuffer 2 (10x), 2 µl 10 % NP-40, 6 µl H_2O and 1 µl PNGase F. The mixture was incubated for 1 h at 37 °C. The deglycosylated protein was analyzed by Western blot.

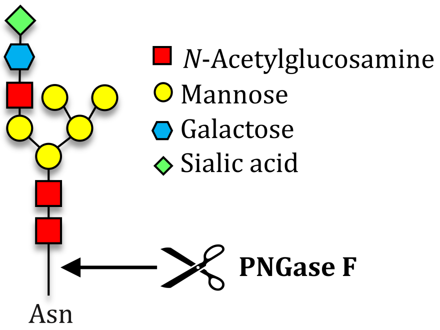

Figure 2.10: Digestion of proteins with PNGase F. The amidase PNGase F is used to remove *N*-linked glycans from the protein core by cleaving between *N*-acetylglucosamine of the *N*-glycan and asparagine of the protein.

2.4.3.13 SDS-PAGE

Sodium dodecyl sulfate-polyacrylamide gel electrophoresis (SDS-PAGE) is a method to separate proteins according to their molecular weight (Laemmli, 1970). Heating and the addition of the detergent SDS causes protein denaturation and results in binding of the negatively charged SDS to the denatured protein chain. The negative charge of the SDS-protein complex correlates with the molecular weight of the protein. To separate the proteins, gels with 9 % acrylamide were placed in the electrophoresis chamber which was then filled up with running buffer. Protein samples were mixed with 6x reducing SDS sample buffer and heated at 95 °C for 5 min before loading into the gel. Additionally, 6 µl Color Prestained Protein Standard were loaded. Electrophoresis was run for 20 min at 80 V and then for about 90 min at 150 V until the band of the Protein Standard at 26 kDa reached the end of the gel.

2.4.3.14 Western blot analysis

After separating the samples by SDS-PAGE, proteins were transferred to a nitrocellulose membrane in order to detect the target proteins. 6 Whatman filter papers, the nitrocellulose membrane and the gel from the SDS-PAGE were incubated in transfer buffer for 10 min prior to the blotting procedure. All components were arranged in the gel holder cassette as follows:

1. 3x Whatman paper
2. Nitrocellulose membrane
3. Polyacrylamide gel
4. 3x Whatman paper

The gel holder cassette was then placed into the wet blotting system which was filled with transfer buffer and blotting was performed for 5 h at 200 mA and 4 °C in order to prevent overheating of the system.

After blotting, the nitrocellulose membrane was cut between the marker bands 46 kDa and 58 kDa into two pieces, one containing the CNTN1 protein and the other one containing the loading control β-actin. Then, the membrane was washed in Tris-buffered saline with Tween 20 (TBST) and unspecific binding sites were blocked with 5 % milk powder in TBST for 45 min at RT. Incubation with primary antibodies (anti-CNTN1, 1:500; patient or control sera, 1:250 or 1:500; anti-β-actin, 1:5000) in 5 % milk powder/TBST was performed overnight at 4 °C. The day after, the nitrocellulose membrane was washed 3 × for 20 min in TBST prior to incubation with appropriate horseradish peroxidase (hrp)-coupled secondary antibodies (1:15 000 in 5 % milk powder/TBST) for 1 h at RT followed by three washing steps (3 × 20 min) in TBST. Detection of the labeled proteins was exhibited by incubating the nitrocellulose membrane with a luminol-based enhanced chemiluminescent (ECL) hrp substrate for 5 min at RT followed by subsequent development of the X-ray film in the dark chamber.

2.4.3.15 HEK 293 cell culture

HEK 293 cells were cultured in minimum essential medium (MEM) supplemented with 1 % Penicillin-Streptomycin (Pen/Strep), 1 % L-glutamine and 10 % FBS. Cells were passaged twice a week before becoming fully confluent. For this, medium was aspirated followed by a washing step with 10 ml PBS. Detachment of the cells was achieved by incubating with 1 ml trypsin-EDTA (0.05 %) for 2 min in the incubator. After trypsinization, 10 ml medium was added to inactivate trypsin and the cell suspension was centrifuged for 5 min at 1500 rpm. The supernatant was removed prior to resuspension of the cell pellet in 10 ml prewarmed medium. In order to achieve the desired confluency, 1 ml of the cell suspension were added to 10 ml medium in a cell culture flask and cells were grown at 37 °C and 5 % CO_2.

2.4.3.16 Transient transfection of HEK 293 cells

Prior to transfection, HEK 293 cells were seeded in 10 cm dishes at a density of 2×10^6 cells/dish for preparing cell lysates (see 2.4.3.10) or directly on 12 mm coverslips at a density of 50 000 cells/coverslip for immunocytochemical analysis. For this, coverslips were coated with poly-D-lysine (0.1 mg/ml) for 1 h at 37 °C and 5 % CO_2, washed twice with ddH_2O and dried. After seeding, cells were grown in medium for 24 h prior to transfection. Transient transfection was performed via the calcium-phosphate precipitation method. DNA, 0.1x TE buffer and 2.5 M $CaCl_2$ were mixed gently before adding 2x HBS buffer dropwise (Table 2.17). The mixture was then incubated for 5 min at 37 °C before adding to the cells drop by drop and placing the cells in the incubator at 37 °C and 5 % CO_2. 16 h after transfection cells were washed twice with medium and placed in the incubator again for 24 h.

Table 2.17: Transient transfection mixture

Reagent	12 mm coverslip	10 cm dish
Plasmid DNA (1 µg/µl)	0.5 µl	10 µl
0.1x TE buffer	22 µl	440 µl
2.5 M $CaCl_2$	2.5 µl	50 µl
2x HBS buffer	25 µl	440 µl

2.4.3.17 Immunocytochemistry of transfected HEK 293 cells

Transiently transfected HEK 293 cells were used for binding assays with patients' sera or PE material. First, unspecific binding sites were blocked in 10 % BSA/PBS at 37 °C and 5 % CO_2. Afterwards cells were incubated with patients' material, control sera or anti-CNTN1 at a dilution of 1:250 in 2 % BSA/PBS for 1 h at 37 °C and 5 % CO_2. Prior to fixation with 4 % PFA for 20 min, cells were washed once with PBS in order to remove unbound antibodies. After fixation, appropriate fluorescent secondary antibodies were added at a dilution of 1:250 in 2 % BSA/PBS and incubated for 1 h at RT in the dark. After washing the HEK 293 cells 3 × 5 min in PBS, they were embedded in VECTASHIELD® Antifade Mounting Medium with DAPI. For long-term storage coverslips were sealed with CoverGrip™ Coverslip Sealant.

2.4.4 Statistical analyses

All data were visualized with the software OriginPro, Version 2020 (OriginLab Corporation, Northampton, MA, USA). Statistical analysis was performed with the software GraphPad Prism version 9.0.0 for Windows (GraphPad Software, San Diego, CA, USA). Normal distribution of data was checked using Shapiro-Wilk tests.

As data from passive transfer experiments were not normally distributed, statistical differences between measurements before and after treatment were evaluated by performing Wilcoxon matched-pairs signed rank tests. Statistical comparisons of post-/preinjection ratios between the healthy control group and the group treated with IgG from seropositive patients were performed by using Mann-Whitney U tests.

Length measurements of the nodal and paranodal region in teased fibers from rats after passive transfer of IgG from a healthy control or anti-NF positive patients were performed in ImageJ, version 1.53c (Wayne Rasband, National Institutes of Health, USA). Normally distributed data of nodal and paranodal lengths were compared between the treatment groups using unpaired two-tailed *t*-tests.

Not-normally distributed data calculated for signal densities of CNTN1 and pan Na_V as well as Pearson correlation coefficients and sodium current densities were compared between the different treatment groups by using Mann-Whitney U tests.

3 Results

3.1 Short-term exposure to anti-NF IgG in a passive transfer rat model

Passive transfer of autoantibodies to animals is a common method to study their pathogenesis *in vivo*. Previously, different studies investigated the effects of autoantibodies directed against the nodal and paranodal proteins contactin 1 (CNTN1) and neurofascin (NF) *in vivo* from seropositive chronic inflammatory demyelinating polyradiculoneuropathy (CIDP) patients (Ng et al., 2012; Yan et al., 2014; Doppler et al., 2019; Manso et al., 2019). In the present study, we aimed to investigate the effects of short-term exposure of anti-NF autoantibodies to the rat sciatic nerve by assessing motor and sensory skills as well as electrophysiological properties after intraneural injection. Purified immunoglobulin G (IgG) from two seropositive patients was used in order to compare pathogenesis of anti-pan-NF autoantibodies (patient 9) and anti-NF155 autoantibodies (patient 10).

3.1.1 Binding of purified IgG from anti-NF positive patients to the node of Ranvier *in vitro*

Binding of anti-NF positive patients' sera to the nodes of Ranvier of rodent teased fibers has been demonstrated in several studies (Querol et al., 2014; Ogata et al., 2015; Cortese et al., 2016; Devaux et al., 2016; Mathey et al., 2017; Stengel et al., 2019). In order to investigate the pathogenesis of purified IgG from seropositive patients in a passive transfer rat model, binding to the nodes of Ranvier of rat nerves is mandatory. We therefore performed binding assays of purified IgG from patients 9 and 10 on rat teased fibers *in vitro* (Fig. 3.1).

IgG from patient 9, who was tested positive against all isoforms of NF (NF140, NF155 and NF186), showed strong reactivity to the nodal and the paranodal region (Fig. 3.1, A). In contrast, IgG of patient 10 only bound to the paranodes (Fig. 3.1, B) demonstrating the specificity to the paranodal NF155 isoform of the protein.

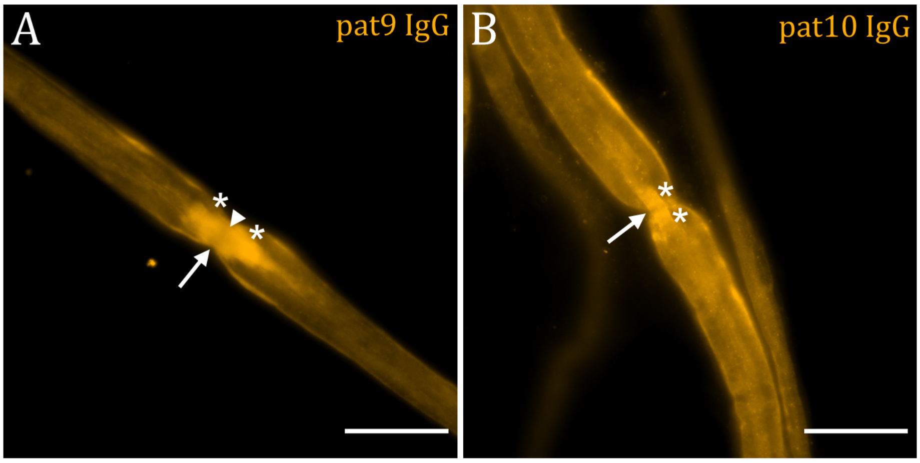

Figure 3.1: Binding of anti-NF positive IgG to the node of Ranvier of rat teased fibers. Immunohistochemistry was performed on rat teased fibers to test the reactivity of purified IgG from patients with anti-NF autoantibody associated CIDP. (A) IgG from the anti-pan-NF positive patient 9 showed binding to the nodal and paranodal region. (B) Anti-NF155 positive IgG from patient 10 reacted against the paranode, but not against the nodal region. White arrows indicate nodes of Ranvier, arrowheads display nodal binding and asterisks mark paranodal binding. Scale bars refer to 20 µm.

3.1.2 Motor and sensory functions are largely maintained after acute exposure to anti-NF IgG

Autoantibodies to NF155 or pan-NF have been detected in a subset of CIDP patients presenting with distinct clinical symptoms. In order to study the pathogenic role of anti-NF autoantibodies *in vivo*, purified IgG from seropositive patients (patient 9: anti-pan-NF IgG3, patient 10: anti-NF155 IgG4) was injected into the sciatic nerve of adult female Lewis rats. Motor and sensory skills were assessed before and after injection to evaluate if acute exposure to anti-NF IgG causes any deficits in the animal model. Table 3.1 and Fig. 3.2 and 3.3 summarize the results from the rotarod performance test, CatWalk™ XT gait analysis as well as the nociception assays.

Motor symptoms like muscle weakness and gait disturbance are common in anti-NF autoantibody associated CIDP. To evaluate the motor abilities and coordination of rats after passive transfer of IgG from seropositive patients (patient 9: anti-pan-NF, patient 10: anti-NF155), the rotarod performance test was used. Therefore, rats were placed on an accelerating rotating drum and the latency until the animal falls down was automatically measured. In the rotarod performance test, the fall latency of animals treated with IgG from the anti-pan-NF positive patient (patient 9) decreased from 275 s before injection to 215 s after injection ($p = 0.0195$, Wilcoxon matched-pairs signed rank test, Table 3.1). In contrast, animals injected with IgG from the anti-NF155 positive patient or from a healthy control did not show any alterations (Table 3.1).

Table 3.1: Summary of data from Rotarod performance test, Catwalk gait analysis and nociception assays of rats injected with IgG from a healthy control or anti-NF positive patients. Values are shown as median (range). Significant differences between pre- and postinjection within the treatment group are marked by an asterisk (*$p < 0.05$, **$p < 0.01$, ***$p < 0.001$).

	HC		**pat9**		**pat10**	
	pre-injection	**post-injection**	**pre-injection**	**post-injection**	**pre-injection**	**post-injection**
Rotarod performance test						
n	15	15	9	9	5	5
Fall latency (s)	156 (86–348)	171 (75–306)	275 (160–368)*	215 (137–197)	112 (65–150)	109 (100–124)
Catwalk gait analysis						
n	18	18	12	12	5	5
Average speed (cm/s)	33 (24–54)	32 (18–43)	35 (30–41)*	28 (23–40)	28 (25–47)	27 (24–37)
Print area (cm^2)	1.3 (0.8–2)	1.4 (0.8–1.7)	1.5 (1.1–2.1)	1.5 (0.9–2)	1.2 (0.7–1.6)	1.3 (1.1–1.7)
Maximum contact area (cm^2)	0.9 (0.6–1.5)	1.1 (0.6–1.3)	1.1 (0.8–1.6)	1.1 (0.7–1.6)	0.9 (0.5–1.2)	1.1 (0.9–1.4)
Maximum intensity (a.u.)	212 (192–224)*	209 (153–219)	218 (209–223)	213 (180–220)	212 (192–215)	209 (200–215)
Standing time (ms)	219 (133–320)	232 (174–395)	209 (193–241)*	249 (198–336)	282 (149–299)	257 (187–294)
Swing time (ms)	131 (112–143)***	144 (120–188)	129 (118–140)**	140 (122–152)	127 (112–158)	153 (125–174)
Stride length (cm)	13 (11–14)	12 (9–15)	13 (12–15)	12 (11–14)	12 (12–13)	12 (11–12)
Step cycle (ms)	349 (240–460)	364 (315–559)	334 (311–386)*	392 (330–475)	384 (266–450)	407 (315–487)
Nociception assays						
n	18	18	12	12	5	5
Von Frey PWT (g)	46 (14–76)	33 (18–46)	39 (21–57)	31 (18–46)	32 (19–46)	26 (14–46)
Hargreaves PWL (s)	9.5 (8.5–13)	8.6 (6.1–13)	9.7 (8.7–11)	9.8 (8.6–13)	10 (9.2–11)	8.4 (7.7–9.8)

HC, healthy control; pat, patient; PWT, paw withdrawal threshold; PWL, paw withdrawal latency

For better comparison of the treatment groups, the post-/preinjection ratios were calculated. A post-/preinjection ratio of 100 % means that animals performed equally before and after injection. However, a ratio below 100 % in the rotarod performance test indicates that the motor coordination is impaired after injection. When comparing the fall latency post-/preinjection ratios between the treatment groups, the decrease detected in animals after injection with IgG from patient 9 did not reach significance compared to the control group (Fig. 3.2, A). This is probably due to the high variability of data in the healthy control group. Post-/preinjection ratios of animals injected with IgG of the anti-NF155 positive patient 10 were comparable with those of the healthy control group (Fig. 3.2, A). In summary, results from the rotarod performance test indicate only slight impairment of motor skills after intraneural injection of anti-pan-NF autoantibodies.

As gait disturbances are frequent in patients with anti-NF autoantibody associated CIDP, we additionally used the CatWalk™ XT system to analyze effects of passive transfer in the rat model. This method allows a more quantitative analysis of the animal's gait. While the rat runs unforced through a walkway, a camera captures all footprints. Calculation of various parameters automatically by the software of the system allows detection of any gait abnormalities.

We first examined the average speed at which the animals traversed the corridor in the CatWalk™ XT system. Analysis revealed a reduced average speed in rats treated with anti-pan-NF IgG from patient 9 compared to baseline values ($p = 0.0161$, Wilcoxon matched-pairs signed rank test, Table 3.1). However, the post-/preinjection ratio (mean: $87 \pm 16\,\%$) did not differ compared to the control group (Fig. 3.2, B) as in this group a slightly reduced average speed was also detectable (mean post-/-preinjection ratio: $92 \pm 17\,\%$). The average speed of animals treated with the anti-NF155 IgG from patient 10 marginally decreased as well (mean post-/preinjection ratio: $95 \pm 25\,\%$). Reduced values after injection in all treatment groups might be due to the short recovery period from the surgical procedure.

Footprint analyses with the CatWalk™ XT system showed neither alterations in the print area nor in the maximum contact area of the left hindpaw, where the IgG was administered, in any of the treatment groups (Table 3.1, Fig. 3.2, C-D). The maximum intensity of the left hindpaw was reduced in animals after treatment with IgG from a healthy control compared to baseline ($p = 0.0385$, Wilcoxon matched-pairs signed rank test, Table 3.1). This indicates that the rat avoids putting weight on the affected paw, another evidence of limping. As the post-/preinjection ratio of the maximum intensity measured in the control group did not differ compared to the patient groups (Fig. 3.2, E), the effect is only mild. A possible explanation is an iatrogenic damage of the sciatic nerve occuring during intraneural injection. Animals treated with IgG from the anti-

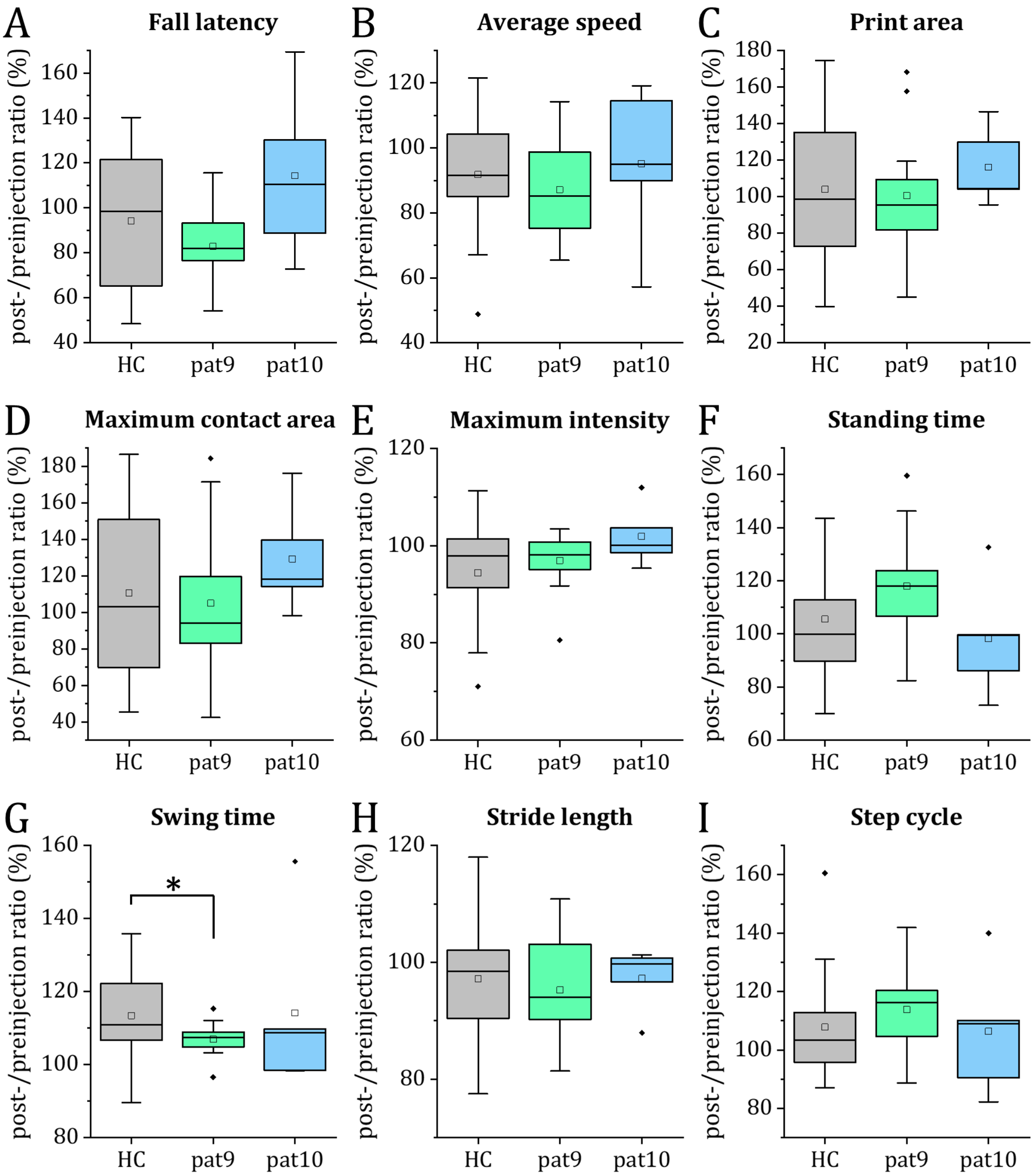

Figure 3.2: Post-/preinjection ratios of different parameters for motor skill assessment in passive transfer experiments. Ratios (%) of motor skill testings after two injections with purified IgG from a healthy control (HC), patient 9 (pat9) or patient 10 (pat10) compared to baseline values determined prior to injection. (A) Post-/preinjection ratios of fall latencies assessed by accelerated rotarod performance test showed no differences between the treatment groups. (B-I) Post-/preinjection ratios of different parameters determined by CatWalk™ XT gait analysis. No differences between the treatment groups were detected for the average speed of animals (B), print area (C), maximum contact area (D), maximum intensity (E) or standing time (F) of the left hindpaw. The post-/preinjection ratio of the swing time of the left hindpaw (G) was reduced in animals treated with IgG of patient 9 compared to the control group. Stride length (H) and step cycle (I) of the left hindpaw showed no differences between the treatment groups. Boxplots show medians as horizontal line within the box and means as white squares. 25th and 75th percentiles are given by the top and bottom of the box. Whiskers show the 1.5 times interquartile range and black squares represent outliers. Significant differences between the treatment groups tested by Mann-Whitney U are marked by an asterisk (*$p < 0.05$).

pan-NF positive patient or the anti-NF155 positive patient did not show alterations in intensity measurements of the left hindpaw (Table 3.1).

Furthermore, foot print analysis with the CatWalk™ XT system showed increased values for the standing time of the left hindpaw in animals injected with IgG from the anti-pan-NF positive patient 9 compared to baseline values (p = 0.0210, Wilcoxon matched-pairs signed rank test, Table 3.1). In contrast, as shown previously, standing time decreased in animals after acute passive transfer of CNTN1 IgG3, which is another evidence for limping (Doppler et al., 2019). As the swing time of the affected hindpaw was also increased in this treatment group (p = 0.0015, Wilcoxon matched-pairs signed rank test, Table 3.1), this is probably caused by the decreased average speed at comparable number of steps during one run. This hypothesis is further supported by the stride length which did not show any differences meaning that the distance between two footprints of the same paw was similar before and after intraneural injection of anti-pan-NF IgG. The swing time was also increased in the control group after injection (p = 0.0003, Wilcoxon matched-pairs signed rank test, Table 3.1) with only a slight increase of the standing time and no differences in the stride length (Table 3.1). In contrast, animals treated with the anti-NF155 positive IgG4 from patient 10 did not show any differences neither in the standing time nor in the swing time nor in the stride length after injection compared to baseline values (Table 3.1). Regarding the post-/preinjection ratios, there were no differences in the standing time (Fig. 3.2, F) but the swing time ratio for animals injected with IgG from patient 9 was lower compared to the control group (p = 0.0479, Mann-Whitney U test, Fig. 3.2, G). The post-/preinjection ratios of the stride length were comparable in all treatment groups (Fig. 3.2, H).

Matching these findings, the step cycle was also increased in animals treated with IgG from the anti-pan-NF patient 9 (p = 0.0122, Wilcoxon matched-pairs signed rank test, Table 3.1). This again indicates that the steps were longer in time but not in distance as the stride length was similar before and after injection. However the post-/preinjection ratios did not show any differences as for the other treatment groups a slight increase in the step cycle was detectable, too (Fig. 3.2, I).

Besides motor symptoms, patients with autoantibodies against NF also show sensory symptoms. We used IgG from two patients in a passive transfer rat model, one with anti-pan-NF autoantibodies and the other one with anti-NF155 autoantibodies. Both patients presented with sensory symptoms like pallanesthesia and hypoesthesia or neuropathic pain.

To test if the sensory function is affected by intraneural injection of anti-NF IgG to the rat sciatic nerve, the paw withdrawal thresholds to mechanical or thermal stimuli were determined by von Frey and Hargreaves assays, respectively. In the von Frey test, nylon filaments of different diameters are applied consecutively to the plantar surface of an animal's paw. As a result, the 50 % paw withdrawal threshold (PWT) can be calculated, i.e., the force of the von Frey hair to which an animal reacts in 50 % of the stimuli. Thus, decreased values in the von Frey test are indicative for allodynia. The von Frey assay did neither reveal any differences in the 50 % PWT after injection of anti-pan-NF IgG nor after treatment with anti-NF155 IgG compared to baseline values (Table 3.2). Additionally, the 50 % PWT in the healthy control group were comparable before and after injection (Table 3.2). Furthermore, no differences for the 50 % PWT between the treatment groups were detectable neither for the treated left hindpaw (Fig. 3.3, A) nor for the untreated right hindpaw (Fig. 3.3, B).

To test the effects of anti-NF autoantibodies on the thermal sensitivity of rats, a plantar test with the Hargreaves Apparatus was performed. In this assay, a heat stimulus is applied to the plantar surface of the hindpaw and the latency until the animal withdrawals its paw is automatically measured. Here again, no differences in the paw withdrawal latency (PWL) were detectable after injection compared to baseline values, neither in the control group nor in both patient groups (Table 3.2). However, the post-/preinjection ratio of animals treated with anti-NF155 positive IgG was lower compared to the ratio of anti-pan-NF injected animals ($p < 0.01$, Mann-Whitney U test, Fig. 3.3, C) but did not differ from the control group. No differences of the post-/preinjection ratios of the untreated right hindpaw between the treatment groups were detectable (3.3, D).

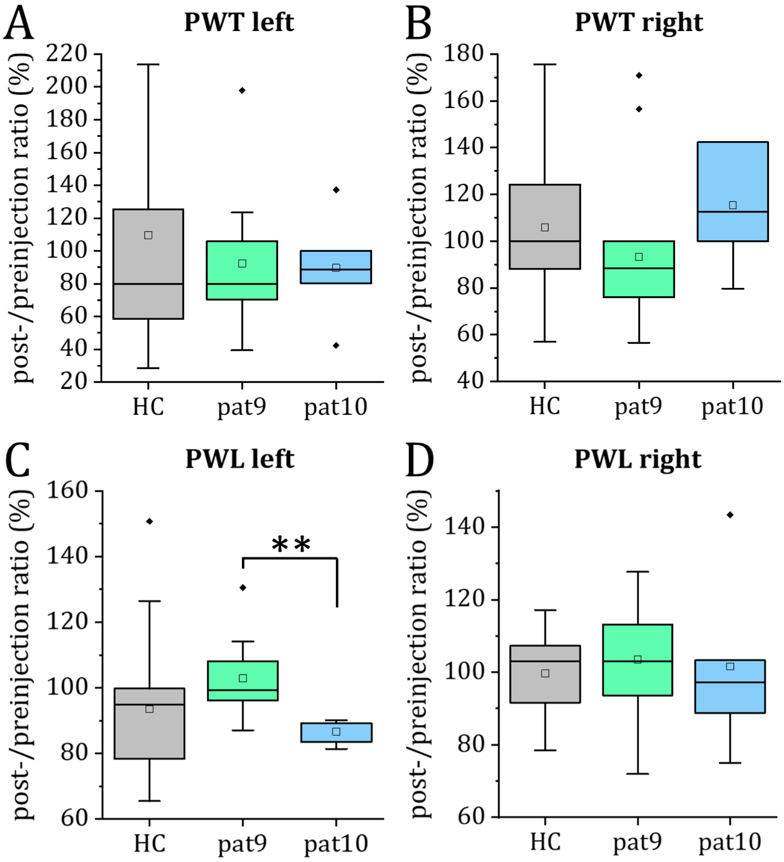

Figure 3.3: Post-/preinjection ratios of different parameters for sensory function assessment in passive transfer experiments. Ratios (%) of sensory function testings after two injections with purified IgG from a healthy control (HC), patient 9 (pat9) or patient 10 (pat10) compared to baseline values determined prior to injection. (A-B) Post-/preinjection ratios of the paw widthdrawal threshold (PWT) evaluated in von Frey assays did not differ between the treatment groups neither for the left hindpaw (A) nor for the right hindpaw (B). (C-D) The paw withdrawal latency (PWL) evaluated by the Hargreaves method was reduced for the left hindpaw of animals treated with purified IgG from patient 10 compared to those treated with IgG from patient 9 (C), whereas the latency for the right hind paw did not differ between the treatment groups (D). Boxplots show medians as horizontal line within the box and means as white squares. 25th and 75th percentiles are given by the top and bottom of the box. Whiskers show the 1.5 times interquartile range and black squares represent outliers. Significant differences between the treatment groups tested by Mann-Whitney U are marked by an asterisk (**$p <$ 0.01).

3.1.3 Acute passive transfer of anti-NF IgG does not cause substantial electrophysiological deficits

Previously, nerve conduction studies (NCS) of patients with anti-NF155 autoantibodies revealed prolonged distal and F-wave latencies as well as decreased compound muscle action potential (CMAP) amplitudes and sensory conduction velocities compared to seronegative CIDP patients (Ogata et al., 2015; Fujita et al., 2018). For patients with anti-pan-NF autoantibodies, NCS demonstrated conduction blocks, prolonged distal motor latencies (dml) and reduced nerve conduction velocities (NCV) as well as decreased CMAP and sensory nerve action potential (SNAP) amplitudes (Delmont et al., 2017; Stengel et al., 2019).

In the present study, NCS were performed to evaluate nerve damage induced by the passive transfer of anti-NF autoantibodies to the sciatic nerve of rats. CMAPs were recorded at the hind paw muscles after distal stimulation at the tibial nerve and after proximal stimulation at the sciatic nerve. Representative recordings of CMAPs as well as exemplary F-wave recordings after repetitive supramaximal stimulations at 0.3 Hz, 1 Hz or 10 Hz are shown in Fig. 3.4. No abnormalities in CMAPs or F-waves were detected neither for the control group (Fig. 3.4, A-B) nor for animals treated with IgG from the anti-pan-NF positive patient 9 (Fig. 3.4, C-D) nor for those treated with IgG from the anti-NF155 positive patient 10 (Fig. 3.4, C-D).

As conduction blocks are frequently present in neuropathy, the distal/proximal CMAP ratio was assessed in animals treated with purified IgG from a healthy control or from anti-NF positive patients before and after injection. Conduction blocks were defined as a distal/proximal ratio of more than 1.5 as performed in Doppler et al. (2019). No conduction blocks were found prior to injection in any of the treatment groups (Fig. 3.5, A). Strikingly, two animals of the control group showed a conduction block after injection whereas no conduction block was detectable in animals treated with patient's IgG (Fig. 3.5, B). The distal CMAP amplitude was comparable before and after injection in all treatment groups (Table 3.2) and the post-/preinjection ratios did not differ between the treatment groups (Fig. 3.5, C). The proximal CMAP amplitude was reduced after injection in the control group compared to the baseline values before injection but not in animals treated with IgG from anti-NF positive patients ($p = 0.0146$, Wilcoxon matched-pairs signed rank test, Table 3.2). This correlates with the conduction block seen in two animals after treatment with IgG from a healthy control. As the IgG was injected directly into the sciatic nerve, we cannot exclude iatrogenic nerve damage as an explanation for these findings. However, the post-/preinjection ratios were not different between the treatment groups (Fig. 3.5, D).

Animals treated with anti-pan-NF IgG from patient 9 showed a reduced dml after injection compared to baseline values ($p = 0.0352$, Wilcoxon matched-pairs signed rank test) whereas animals treated with IgG from patient 10 and the control group did not show any differences before and after injection (Table 3.2). As nerve damage usually leads to a prolonged dml, the finding of a reduced dml after passive transfer of anti-pan-NF autoantibodies was unexpected. However, when comparing the dml post-/preinjection ratio with the control group, no significant difference was observable arguing for only a slight reduction (Fig. 3.5, E).

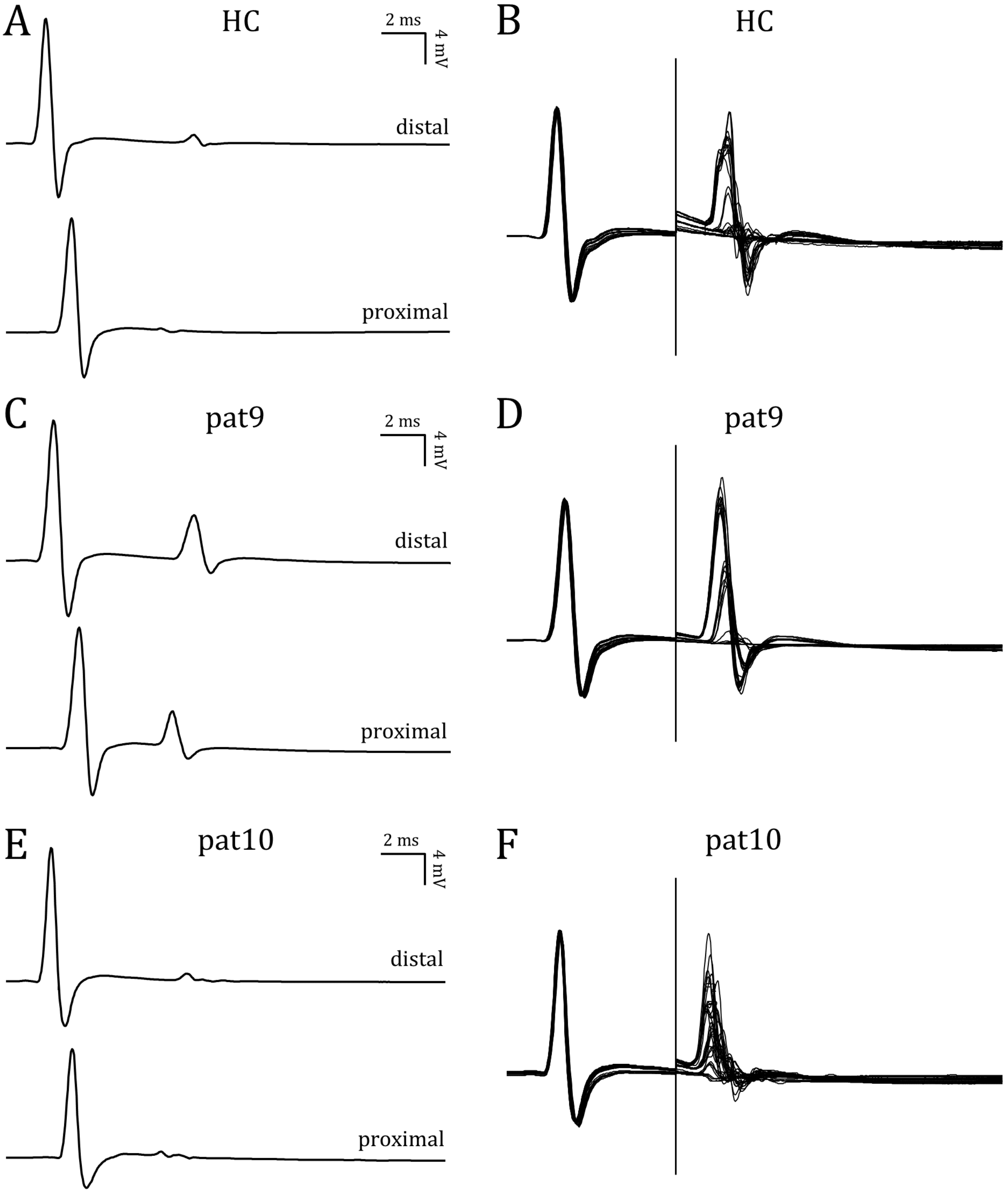

Figure 3.4: Exemplary recordings of compound muscle action potentials and F-waves. Compound muscle action potentials (CMAPs) were measured after distal and proximal supramaximal stimulation and F-waves were recorded after ten repetitive supramaximal distal stimulations at frequencies of 0.3 Hz, 1 Hz and 10 Hz in animals treated with purified IgG of a healthy control (HC, A-B), patient 9 (pat9, C-D) or patient 10 (pat10, E-F).

Table 3.2: Summary of data from nerve conduction studies of rats injected with IgG from a healthy control or anti-NF positive patients. Values are shown as median (range). Significant differences between pre- and postinjection within the treatment group are marked by an asterisk (*$p < 0.05$, **$p < 0.01$).

	HC		**pat9**		**pat10**	
	pre-injection	**post-injection**	**pre-injection**	**post-injection**	**pre-injection**	**post-injection**
n	15	15	10	10	5	5
Distal CMAP amplitude (mV)	19 (13–27)	17 (15–25)	18 (14–26)	18 (15–25)	21 (20–23)	18 (11–23)
Proximal CMAP amplitude (mV)	16 (12–22)*	13 (6–20)	16 (13–22)	16 (11–22)	17 (17–20)	15 (9–18)
Distal motor latency (ms)	1.3 (1.1–1.6)	1.3 (1.1–1.7)	1.5 (1.3–1.8)*	1.4 (1.2–1.5)	1.3 (1.2–1.4)	1.4 (1–1.4)
Motor NCV (m/s)	40 (31–47)	35 (30–50)	41 (23–49)	35 (32–47)	36 (31–45)	36 (34–56)
F-wave latency (ms)	8.5 (7.8–10)	8.8 (8–11)	8.7 (8–10)	9 (8.1–9.8)	8.9 (8.7–10)	8.5 (7.4–9.7)
SNAP amplitude (µV)	29 (18–109)	28 (12–58)	32 (18–84)	28 (19–65)	25 (20–32)	33 (6.5–51)
Sensory NCV (m/s)	48 (40–59)**	44 (33–51)	50 (33–63)	46 (37–67)	45 (37–83)	47 (43–52)
F-wave persistence 0.3 Hz (%)	100 (100–100)	100 (10–100)	100 (80–100)	100 (100–100)	100 (100–100)	100 (100–100)
F-wave persistence 1 Hz (%)	100 (10–100)	100 (10–100)	100 (40–100)	55 (10–100)	100 (20–100)	50 (30–100)
F-wave persistence 10 Hz (%)	70 (10–100)*	30 (0–100)	50 (20–100)	45 (10–100)	30 (20–100)	30 (10–100)

HC, healthy control; pat, patient; CMAP, compound muscle action potential; NCV, nerve conduction velocity; SNAP, sensory nerve action potential

The motor NCV was calculated by dividing the distance of stimulation and recording electrode by the dml. No abnormalities for the motor NCV were detected neither in the control group nor in the patient groups (Table 3.2, Fig. 3.5, F). In anti-NF155 positive CIDP patients, F-wave latencies are usually prolonged. In our study, F-wave latencies were comparable in all treatment groups after injection compared to baseline values (Table 3.2). However the post-/preinjection ratio was decreased in animals injected with IgG from the anti-NF155 positive patient compared to the control group ($p = 0.0206$, Mann-Whitney U test, Fig. 3.5, G).

No relevant abnormal findings in the SNAP amplitudes were detected in any of the treatment groups (Table 3.2, Fig. 3.5, H). Sensory NCV were reduced in the healthy control group after the injection ($p = 0.0085$, Wilcoxon matched-pairs signed rank test) but not in animals treated with anti-NF positive IgG (Table 3.2). However, the sensory NCV post-/preinjection ratios were not different between the treatment groups (Fig. 3.5, I).

As loss of F-waves is a typical sign of demyelination and proximal conduction block, F-waves were recorded after ten repetitive stimuli at 0.3 Hz, 1 Hz and 10 Hz in every treatment group before and after injection. F-wave persistences (number of F-wave responses per number of stimuli) at 0.3 Hz and 1 Hz were similar before and after injection for all treatment groups (Table 3.2, Fig. 3.6, A-B). At a stimulation frequency of 10 Hz, however, F-wave persistence was reduced in the control group after injection compared to baseline values ($p = 0.0415$, Wilcoxon matched-pairs signed rank test), whereas persistences were not affected in the patient groups (Table 3.2, Fig. 3.6, C).

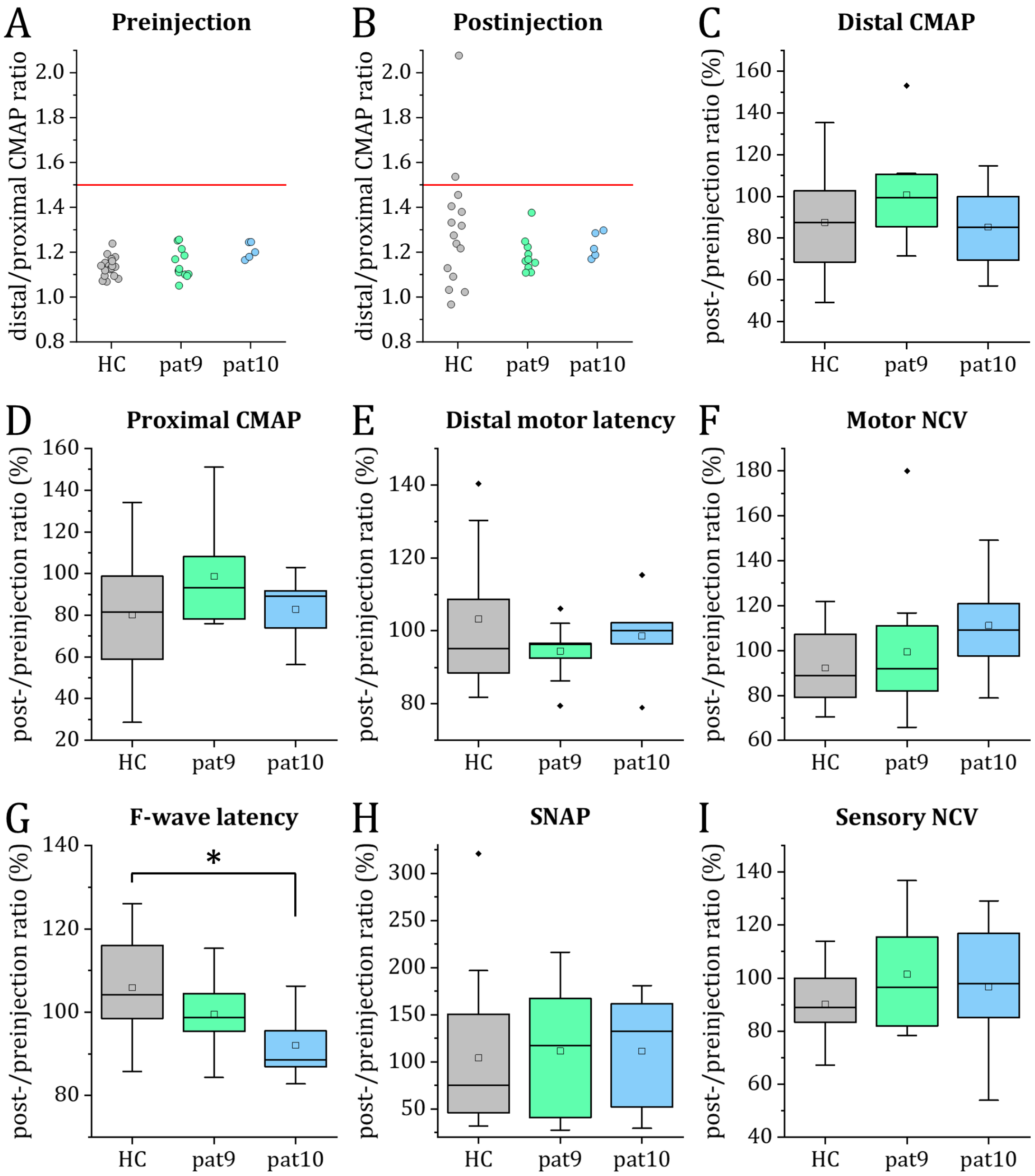

Figure 3.5: Post-/preinjection ratios of different parameters from nerve conduction studies in passive transfer experiments. (A-B) Distal/proximal compound muscle action potential (CMAP) ratios in animals treated with purified IgG from a healthy control (HC), patient 9 (pat9) or patient 10 (pat10). Conduction blocks were defined as a distal/proximal CMAP ratio of > 1.5 (red horizontal line). No conduction blocks were found prior to injection (A). Two animals of the control group showed a conduction block after injection (B). (C-I) Ratios (%) of different parameters from NCS after two injections with purified IgG from a healthy control, patient 9 or patient 10 compared to baseline values determined prior to injection. No differences were found in the ratios between the treatment groups for the distal CMAP amplitude (C), the proximal CMAP amplitude (D), the distal motor latency (E) or the motor nerve conduction velocity (NCV, F). The post-/preinjection ratio of the F-wave latency was reduced after treatment with IgG from patient 10 compared to the control group (G). Post-/preinjection ratios of the sensory nerve action potential amplitude (SNAP, H) and the sensory NCV (I) showed no differences. Boxplots show medians as horizontal line within the box and means as white squares. 25th and 75th percentiles are given by the top and bottom of the box. Whiskers show the 1.5 times interquartile range and black squares represent outliers. Significant differences between the treatment groups tested by Mann-Whitney U are marked by an asterisk ($*p < 0.05$).

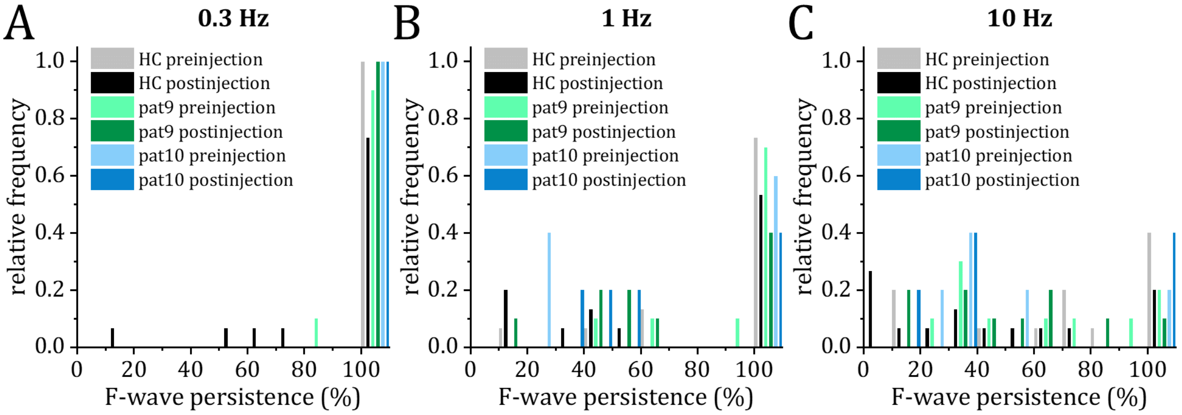

Figure 3.6: Relative frequencies of F-wave persistences in passive transfer experiments. Relative frequencies of F-wave persistences demonstrated no abnormalities at a stimulation frequencies of 0.3 Hz (A) and 1 Hz (B) for animals treated with IgG from a healthy control (HC), patient 9 (pat9) or patient 10 (pat10) neither before nor after injection. At a stimulation frequency of 10 Hz (C) 4 out of 15 animals from the control group showed a complete loss of F-waves after injection. Frequencies of F-wave persistences for animals treated with IgG from anti-NF positive patients showed no abnormalities before and after injection.

3.1.4 The structure of the node of Ranvier is preserved after passive transfer of anti-NF IgG

Binding of anti-paranodal autoantibodies *in vivo* has been demonstrated in previous studies. In the present study, we injected purified IgG from an anti-pan-NF positive patient (patient 9) as well as from an anti-NF155 positive patient intraneurally to the sciatic nerve of adult rats twice with one day in between. The sciatic nerve was dissected two days after the last injection and analyzed immunohistochemically for autoantibody deposition. No binding was detectable in teased fibers of animals injected with IgG from a healthy control (Fig. 3.7, A). In contrast, anti-pan-NF positive IgG labelled the nodal region in some nodes after intraneural injection (Fig. 3.7, B-C). Overall, nodal binding was detected in 50 % of animals treated with anti-pan-NF IgG3. However, we could not detect any binding in teased fiber preparations of animals injected with anti-NF155 IgG4 (Fig. 3.7, D), indicating that the paranodes are not accessible for autoantibodies in an acute passive transfer animal model.

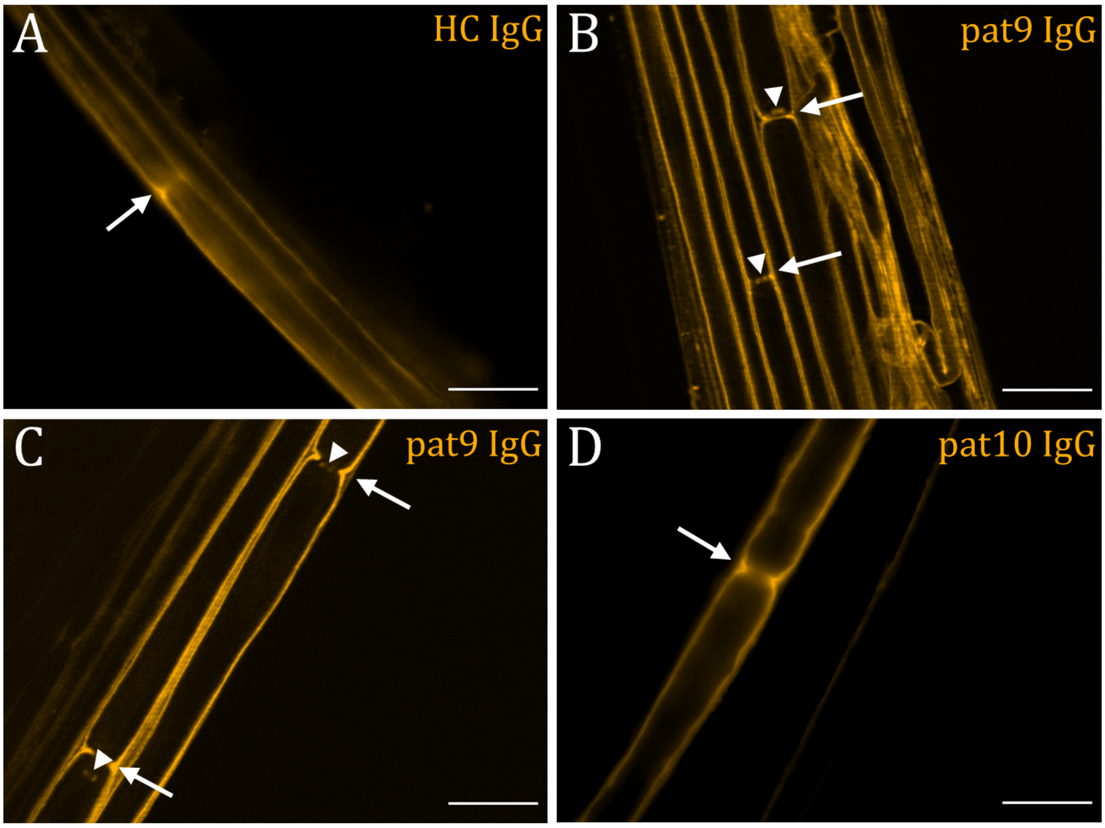

Figure 3.7: Binding of anti-pan-NF IgG is restricted to the node in an acute passive transfer rat model. Teased fiber preparations from the rat sciatic nerve were incubated with anti-human IgG Cy™ 3 after intraneural injection of IgG from a healthy control (HC, A), an anti-pan-NF positive patient (pat9, B-C) or an anti-NF155 positive patient (pat10, D). Binding indicated by white arrowheads to the nodal region of the node of Ranvier (indicated by white arrows) was only detected in animals treated with IgG from the anti-pan-NF positive patient 9. Scale bars refer to 20 µm.

In the present study, we aimed to investigate the nodal organization after acute passive transfer of anti-pan-NF IgG3 or anti-NF IgG4 by immunohistochemical analysis. We therefore labelled the nodal region and the paranodal region with a commercial pan-voltage-gated sodium (Na_V) antibody and a commercial antibody directed against contactin associated protein (Caspr), respectively. Representative images of the different treatment groups are shown in Fig. 3.8, A-C. For analysis, length measurements of the nodal region and the paranodal region were performed in ImageJ.

The mean nodal length (n = 100 nodes/treatment group, Fig. 3.8, D) in animals treated with IgG from a healthy control was 1.2 ± 0.3 µm and did not differ from the mean length measured in animals injected with IgG from the anti-pan-NF positive patient 9 (1.2 ± 0.2 µm, $p > 0.05$, unpaired two-tailed t-test). Similarly, no alterations of the mean nodal length were detectable in teased fibers of animals injected with IgG from the anti-NF155 positive patient 10 compared to the control group (1.2 ± 0.3 µm, $p > 0.05$, unpaired two-tailed t-test).

Analysis of 200 hemiparanodes per treatment group (Fig. 3.8, E) revealed a mean length of $3.4 \pm 0.5\,\mu m$ after passive transfer of IgG from a healthy control. Again, no alterations were detectable neither compared to animals injected with anti-pan-NF IgG3 ($3.5 \pm 0.6\,\mu m$, $p > 0.05$, unpaired two-tailed t-test) nor for animals treated with anti-NF155 IgG4 ($3.4 \pm 0.5\,\mu m$, $p > 0.05$, unpaired two-tailed t-test). Furthermore, we could not detect nodes lacking paranodes in any of the treatment groups.

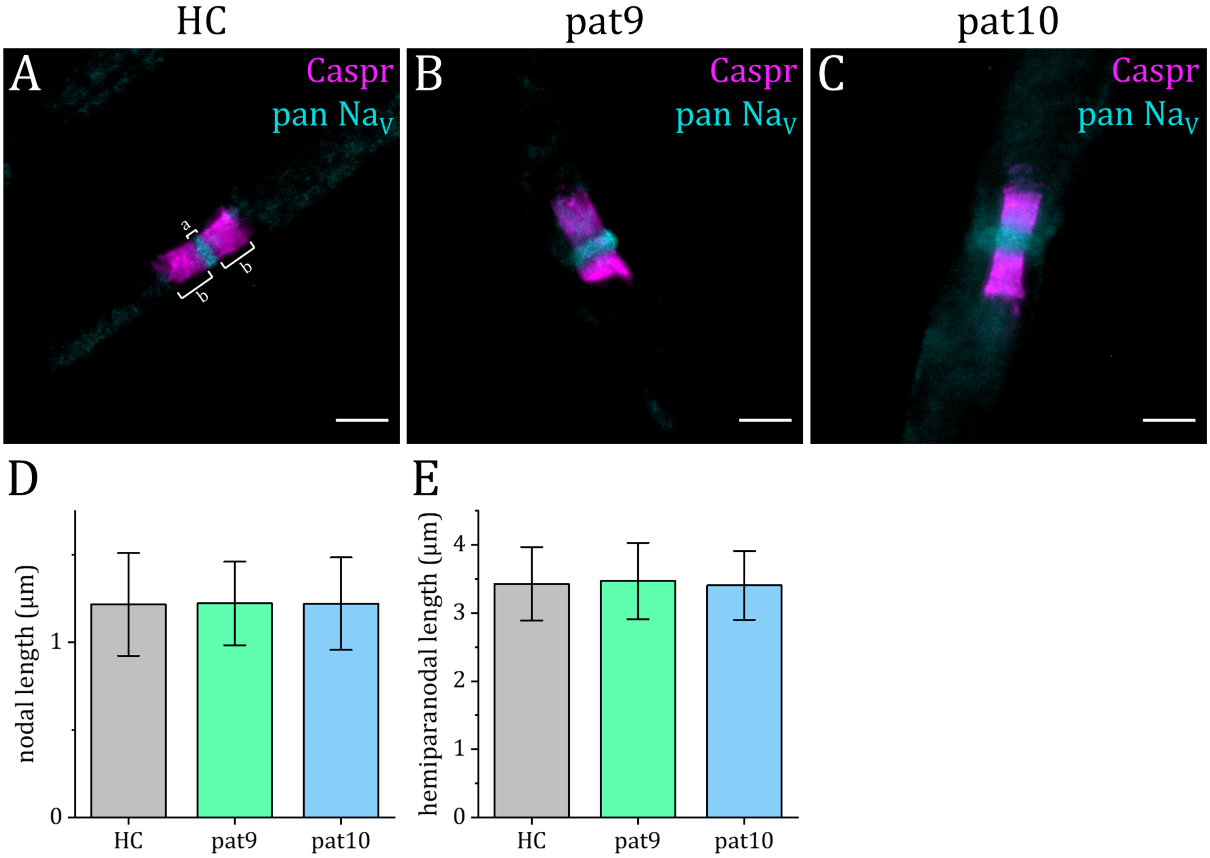

Figure 3.8: No structural alterations of the node of Ranvier after acute passive transfer of anti-NF IgG. Teased fibers of animals treated with IgG from a healthy control (HC, A), the anti-pan-NF positive patient 9 (pat9, B) or the anti-NF155 positive patient 10 (pat10, C) were immunohistochemically stained against Caspr (magenta) to label the paranodes and against pan Na_V (cyan) to detect the nodal region. (D) Length measurements of the nodal region (marked in A with a) did not show any differences between the treatment groups (n = 100 nodes/treatment group). Similarly, the hemiparanodal length (marked in A with b) was comparable in all treatment groups (n = 200 hemiparanodes/treatment group). Scale bars in A-C refer to $5\,\mu m$.

3.2 DRGs as second site of attack in anti-CNTN1 associated polyneuropathy

Previously, several studies reported a high prevalence of sensory ataxia in anti-CNTN1 positive patients (Miura et al., 2015; Appeltshauser et al., 2020; Dubey et al., 2020). However, the pathogenesis causing this symptom has not been investigated yet although an involvement of dorsal root ganglion (DRG) neurons is considered (Miura et al., 2015). In order to study the effect of anti-CNTN1 autoantibodies on DRG neurons, we performed protein localization analysis by super-resolution microscopy and measured sodium current densities in DRG neurons treated with serum of anti-CNTN1 positive patients.

3.2.1 Binding of anti-CNTN1 from seropositive patients to DRG neurons

To investigate possible effects of anti-CNTN1 autoantibodies on DRG neurons, binding to this cell type is a prerequisite. Therefore, double immunofluorescence assays on DRG neurons from adult mice were performed (Fig. 3.9). Neurons were incubated with serum of a healthy control or serum of anti-CNTN1 positive patient 1 (mainly IgG3), plasma exchange (PE) material of patient 2 (mainly IgG4) or serum of patient 3 (mainly IgG4) and co-stained with a commercial antibody to CNTN1. No specific signal was detected in neurons treated with the control serum (Fig. 3.9, A), whereas clear binding of all three patients' sera was observed (Fig. 3.9, B-D). This binding strongly co-localized with the signal of the commercial antibody directed against CNTN1.

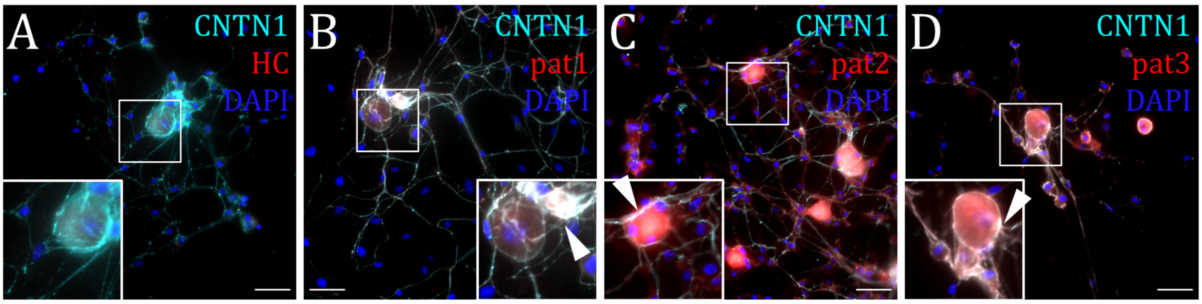

Figure 3.9: Binding of anti-CNTN1 positive patients' sera to adult DRG neurons. Double-immunofluorescence of a commercial antibody directed against CNTN1 (cyan) and sera of a healthy control or anti-CNTN1 positive patients (red). No specific signal was detectable when incubated with a control serum (HC, A). In contrast, sera of patient 1 (pat1, B), patient 2 (pat2, C) and patient 3 (pat3, D) showed strong binding to the neurons. As indicated by the white arrows, this signal overlapped with the staining of a commercial antibody to CNTN1. DAPI (blue) was used to label cell nuclei. Scale bars refer to 50 µm.

3.2.2 Ultrastructural analysis of CNTN1 and pan Na_V in DRG neurons following incubation with anti-CNTN1 positive patients' sera

As CNTN1 interacts with specific sodium channels via their β subunit, effects of anti-CNTN1 autoantibodies on the expression of both proteins in DRG neurons were investigated via super-resolution microscopy. At the time of investigation, another doctoral student from our working group already observed a reduction of CNTN1 signal in immunofluorescent stainings of primary neurons after incubation with CNTN1 autoantibodies from seropositive patients. This reduction was most prominent after three days of incubation. Thus, we incubated DRG neurons with serum of three healthy controls or three anti-CNTN1 positive patients for three days and subsequently immunostained for CNTN1 and pan Na_V.

Exemplary structured illumination microscopy (SIM) recordings are shown in Fig. 3.10. Neurons incubated with serum of a healthy control show co-localization of both proteins in a large overview image (Fig. 3.10, A) as well as in a selected axonal region (Fig. 3.10, B). The level of coincidence is visualized in a plot profile (Fig. 3.10, C) depicting signal intensities of both proteins along a 5 µm long axonal structure from Fig. 3.10, B. DRG neurons incubated with serum of patient 1 (mainly IgG3 anti-CNTN1) for 72 h showed decreased signal intensities for CNTN1 leading to a reduced overlapping of CNTN1 and pan Na_V signal intensities (Fig. 3.10, D-F). A reduction in the CNTN1 signal was also observed in DRG neurons treated with serum of patient 2 (Fig. 3.10, G-I; mainly IgG4) and patient 3 (Fig. 3.10, H-L; mainly IgG4) for 72 h but was not as prominent as for neurons incubated with serum of patient 1.

Quantification of CNTN1 signal densities (sum intensity/summed area in μm^2, Fig. 3.11, A) was in line with the observations made from the SIM recordings. The median CNTN1 signal density of neurons incubated with serum of patient 1 was reduced (8.9×10^5 (7.7×10^5–1.3×10^6) a.u./μm^2, n = 16, $p = 0.0008$, Mann-Whitney U test) compared to the signal density of the control group pooled of three healthy controls (1.5×10^6 (7.7×10^5–2.3×10^6) a.u./μm^2, n = 43). Furthermore, CNTN1 median signal densities of DRG neurons treated with serum of patient 2 (1×10^6 (7.4×10^5–1.7×10^6) a.u./μm^2, n = 14, $p = 0.0086$, Mann-Whitney U test) or patient 3 (9.8×10^5 (6.9×10^5–1.9×10^6) a.u./μm^2, n = 15, $p = 0.0139$, Mann-Whitney U test) were also reduced compared to the control group.

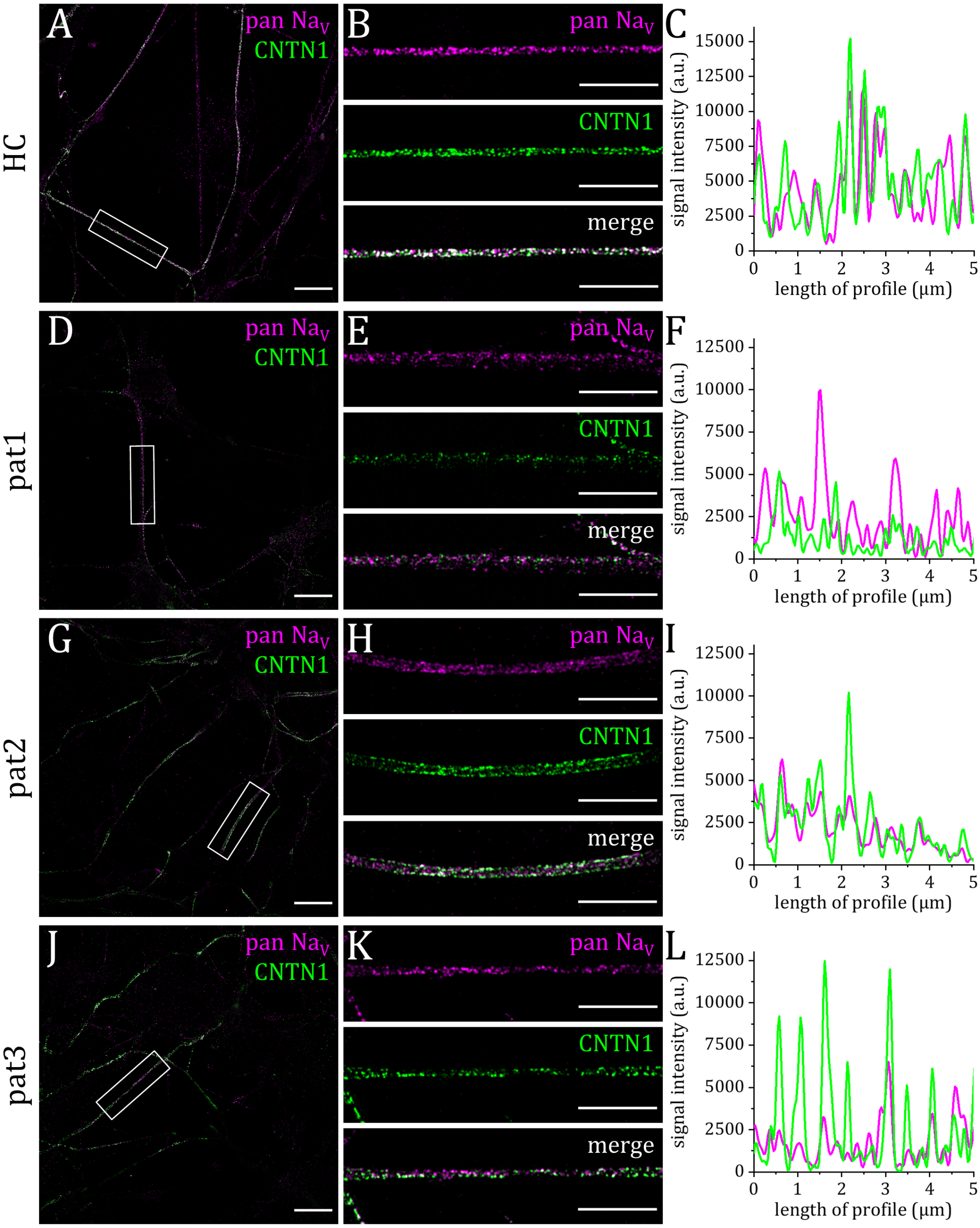

Figure 3.10: Exemplary SIM recordings and plot profiles of DRG neurons incubated with sera of a healthy control or anti-CNTN1 positive patients. SIM recordings of DRG neurons incubated with serum of a healthy control (A), patient 1 (D), patient 2 (G) or patient 3 (J) for 72 h and double immunolabeled for pan Na$_V$ (magenta) and CNTN1 (green). Scale bars refer to 10 µm. Detailed views of insets are given in B, E, H and K, respectively. Scale bars: 5 µm. (C, F, I, L) Plot profiles of single axons taken from B, E, H and K with a length of 6 µm show the overlapping of signals from pan Na$_V$ (magenta) and CNTN1 (green). Note the different y-axis scale.

Additionally, signal densities of pan $\mathrm{Na_V}$ in DRG neurons were analyzed after the treatment with anti-CNTN1 positive patients' sera (Fig. 3.11, B). However, no changes were observable compared to the control group (median signal density (range) for neurons treated with serum of three healthy controls: 1.5×10^6 (2.6×10^5–3.7×10^6) a.u./μm^2, n = 44; patient 1: 1.1×10^6 (1.8×10^5–4.1×10^6) a.u./μm^2, n = 17; patient 2: 1.3×10^6 (4×10^5–3.4×10^6) a.u./μm^2, n = 14; patient 3: 1.4×10^6 (4.8×10^5–4.3×10^6) a.u./μm^2, n = 15).

As CNTN1 is suggested to be a direct interaction partner of specific sodium channels, co-localization of CNTN1 and pan $\mathrm{Na_V}$ signals was analyzed by calculating Pearson correlation coefficients. A Pearson correlation coefficient of 1 would indicate a perfect linear relationship of both signals, whereas a correlation coefficient of 0 means that both signals are not correlated. CNTN1 and pan $\mathrm{Na_V}$ signals of DRG neurons incubated with sera of healthy controls showed a median Pearson correlation coefficient of 0.42 (0.18–0.58, n = 44, Fig. 3.11, C). For neurons incubated with sera of anti-CNTN1 positive patients, Pearson correlation coefficients were reduced compared to the control group (DRG neurons treated with serum of patient 1: 0.35 (0.25–0.58, n = 15, $p = 0.0096$; patient 2: 0.33 (0.19–0.47, n = 14, $p = 0.0172$; patient 3: 0.33 (0.22–0.43, n = 15, $p = 0.003$, Fig. 3.11, C). These results are in line with the findings from the signal density measurements as the overall signal of CNTN1 is dramatically reduced after the treatment with anti-CNTN1 autoantibodies and thus may account for the lower co-localization of the two proteins.

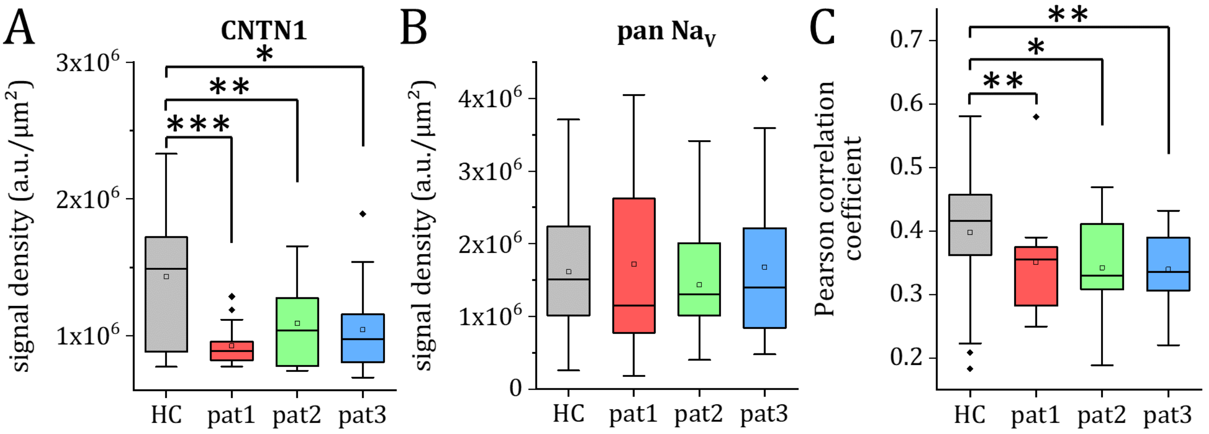

Figure 3.11: Quantification of CNTN1 and pan $\mathrm{Na_V}$ signal densities from SIM recordings of DRG neurons treated with anti-CNTN1 autoantibodies. (A) Reduced signal densities (a.u./μm^2) of CNTN1 in DRG neurons incubated with all three patients' sera (pat1, pat2, pat3) for 72 h compared to the control group pooled of three healthy controls. (B) No differences in pan $\mathrm{Na_V}$ signal densities. (C) Reduced Pearson correlation coefficients calculated from SIM recordings of DRG neurons incubated with anti-CNTN1 positive patients' sera compared to the healthy control group. Boxplots show medians as horizontal line within the box and means as white squares. 25th and 75th percentiles are given by the top and bottom of the box. Whiskers show the 1.5 times interquartile range and black squares represent outliers. Significant differences between the treatment groups tested by Mann-Whitney U are marked by an asterisk ($*p < 0.05$, $**p < 0.01$, $***p < 0.001$).

3.2.3 Reduced sodium currents in DRGs after long-term treatment with anti-CNTN1 autoantibodies

It has been shown that sodium current densities are increased in cells co-transfected with CNTN1, $Na_V1.2\alpha$ and $\beta1$ subunits compared to cells without CNTN1. As we could show a reduction of CNTN1 surface expression in DRG neurons treated with anti-CNTN1 autoantibodies by analyzing SIM measurements, the question of a potential functional effect on sodium current densities arose. To study this hypothesis, whole-cell recordings of Na_V channels were performed on adult DRG neurons incubated for specific time periods (1 h, 2 h, 24 h, 48 h and 72 h) with either control sera or sera from anti-CNTN1 positive patients. A voltage-step protocol from −80 mV to +60 mV at a holding potential of −70 mV was used to record Na_V currents (Fig. 3.12, A).

Exemplary sodium current traces at −40 mV for neurons treated with serum of a healthy control, patient 1, patient 2 or patient 3 for 1 h or 72 h, respectively, are shown in Fig. 3.12, A. Here, amplitudes of current traces from cells incubated with anti-CNTN1 autoantibodies from seropositive patients were decreased compared to those from cells treated with a control serum. Peak current densities were calculated by dividing currents by the cell capacitance (c-slow) which is proportional to the cell size (Golowasch et al., 2009) and thus provides normalization of the values. Numbers of investigated cells, cell capacitances, and peak current densities at −40 mV for the different incubation times with controls' or patients' sera are summarized in Table 3.3.

Current densities of DRG neurons treated with sera of patient 1, patient 2 or patient 3 for 1 h, 2 h, 24 h, and 48 h were not altered compared to those incubated with sera of three healthy controls (Fig. 3.12, B). However, at an incubation time of 72 h with serum of patient 1, median Na_V current densities were reduced compared to the control group (control: 248 (115–688) pA/pF, n = 32; patient 1: 173 (109–395) pA/pF, n = 12, $p = 0.0169$, Mann-Whitney U test). A decrease of current densities was also observed for neurons after long-term treatment (72 h) with serum of patient 3 (174 (90–385) pA/pF, n = 18, $p = 0.007$, Mann-Whitney U test). Current-voltage relationships are consistent with these findings, as no differences were detectable after short-term treatment whereas long-term treatment with sera of patients 1 and 3 led to a decrease of current densities compared to the control group at voltages of −40 mV to 0 mV or −40 mV to +20 mV, respectively (Fig. 3.12, C).

Further analysis of Na_V current densities was performed by differentiation of DRG neurons by size as performed previously (Yudin et al., 2016). In accordance with this, cells with a capacitance of < 15 pF were defined as nociceptive small-diameter neurons, those with a capacitance of > 15 pF as proprioceptive medium-large DRG neurons. Here, a reduction of sodium current densities in medium-large diameter DRG neurons was observable after long-term treatment with anti-CNTN1 positive serum of patient 3 (132 (90–266) pA/pF, n = 18, $p = 0.0438$, Mann-Whitney U test) compared to the control group (213 (115–355) pA/pF, n = 17; Fig. 3.13). Current densities for small DRG neurons or any other treatment condition were indistinguishable from the appropriate control group. Here, interpretations should be made with caution, as the number of investigated cells is relatively low due to the high amount of experimental conditions (see Table 3.3).

Table 3.3: Number of investigated cells (n), cell capacitance (pF) and peak current densities at −40 mV of DRG neurons treated for 1 h, 2 h, 24 h, 48 h and 72 h with serum of healthy controls (HC), patient 1 (pat1), patient 2 (pat2) or patient 3 (pat3). Values are shown as median (range).

	HC			**pat1**			**pat2**			**pat3**		
	n	**capacitance (pF)**	**current density (pA/pF)**	**n**	**capacitance (pF)**	**current density (pA/pF)**	**n**	**capacitance (pF)**	**current density (pA/pF)**	**n**	**capacitance (pF)**	**current density (pA/pF)**
total DRG neurons												
1 h	23	14 (4–21)	270 (119–637)	8	15 (9–24)	241 (170–391)	10	14 (8–32)	270 (135–349)	13	15 (8–21)	255 (130–311)
2 h	18	14 (11–20)	254 (92–465)	11	15 (11–23)	280 (211–425)	9	14 (7–21)	303 (134–556)	24	14 (8–28)	293 (129–542)
24 h	25	15 (6–25)	231 (124–542)	15	14 (6–22)	256 (111–768)	10	15 (11–20)	217 (154–289)	21	16 (11–38)	195 (64–386)
48 h	26	15 (5–30)	242 (124–661)	19	16 (5–23)	243 (143–512)	10	14 (9–21)	282 (172–489)	23	15 (6–20)	318 (137–907)
72 h	32	15 (8–23)	248 (115–688)	12	18 (14–32)	173 (109–395)	5	14 (11–15)	191 (162–272)	18	17 (12–22)	174 (90–385)
small DRG neurons												
1 h	13	9 (4–14)	318 (178–637)	4	11 (9–14)	316 (173–391)	7	12 (8–14)	285 (163–349)	8	13 (8–15)	262 (184–311)
2 h	12	13 (11–15)	273 (225–465)	5	12 (11–14)	317 (211–341)	5	11 (7–14)	348 (134–556)	17	13 (8–14)	336 (172–542)
24 h	12	11 (6–14)	274 (193–542)	9	11 (6–14)	285 (204–768)	4	13 (11–15)	273 (219–279)	5	14 (11–15)	241 (176–386)
48 h	12	12 (5–15)	356 (207–661)	7	13 (5–15)	286 (218–512)	6	11 (9–15)	342 (254–489)	13	12 (6–15)	394 (161–907)
72 h	15	13 (8–15)	278 (154–688)	2	15 (14–15)	271 (147–395)	3	12 (11–14)	164 (162–272)	4	13 (12–15)	234 (203–385)
medium-large DRG neurons												
1 h	10	19 (15–21)	178 (119–303)	4	19 (16–24)	203 (170–257)	3	19 (16–32)	143 (135–148)	5	16 (15–21)	180 (130–259)
2 h	6	16 (15–20)	172 (92–264)	6	16 (15–23)	244 (230–425)	4	17 (15–21)	248 (138–310)	7	18 (15–28)	182 (129–287)
24 h	13	19 (15–25)	196 (124–312)	6	20 (16–22)	241 (111–266)	6	17 (15–20)	183 (154–289)	16	18 (15–38)	188 (64–385)
48 h	14	19 (15–30)	198 (124–311)	12	18 (16–23)	219 (143–470)	4	17 (16–21)	209 (172–232)	10	18 (16–20)	211 (137–301)
72 h	17	19 (15–23)	213 (115–355)	10	19 (16–32)	173 (109–337)	2	15 (15–15)	213 (191–235)	14	18 (15–22)	132 (90–266)

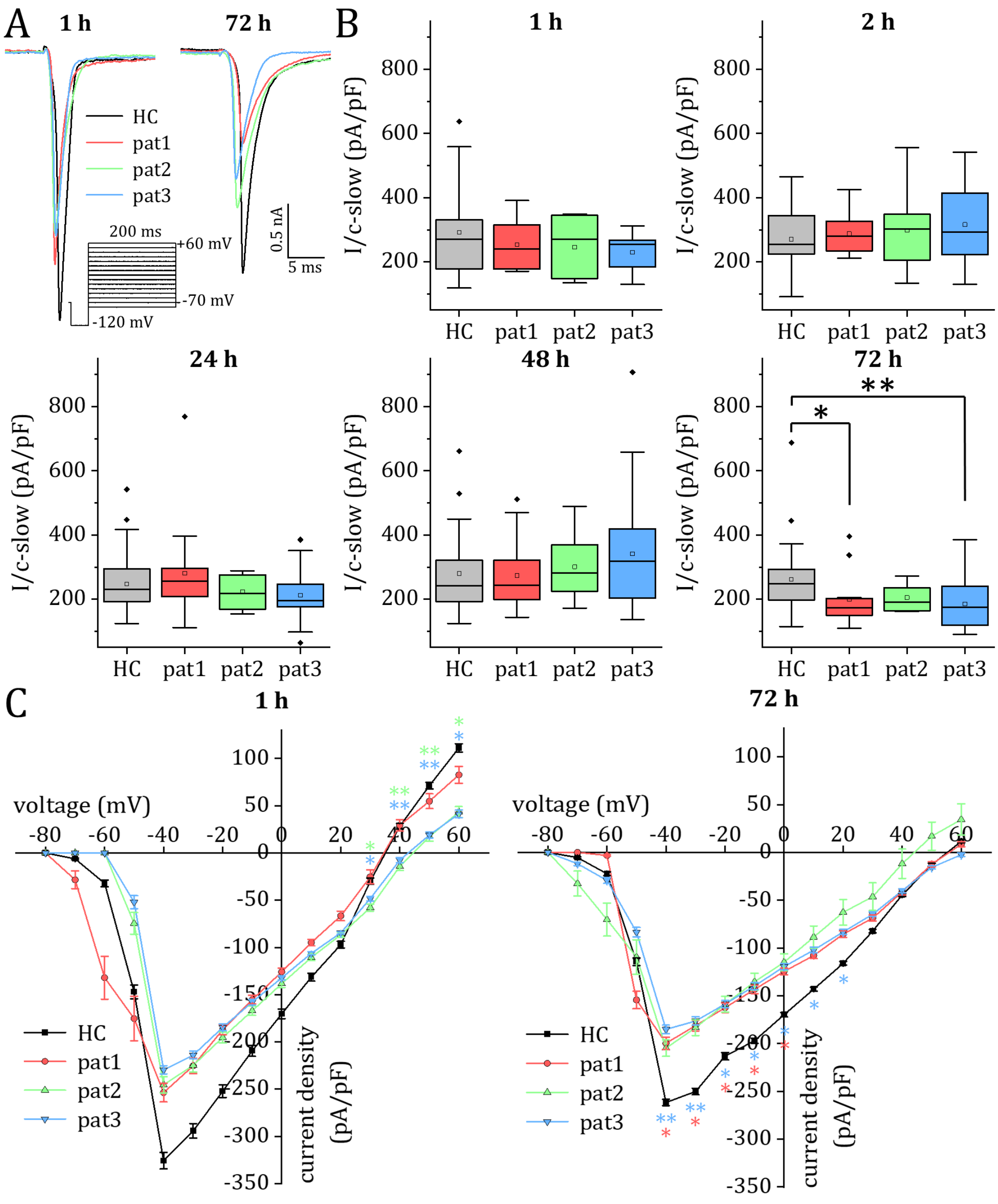

Figure 3.12: Reduced sodium current densities in DRG neurons after long-term exposure to anti-CNTN1 autoantibodies. (A) Exemplary inward sodium current traces of DRG neurons incubated with serum of a healthy control (HC), serum of patient 1 (pat1), PE material of patient 2 (pat2) or serum of patient 3 (pat 3) for 1 h or 72 h, respectively. Current traces were recorded at −40 mV by using a voltage-step protocol from −80 mV to +60 mV in 10 mV increments with a pre-pulse potential of −120 mV and a holding potential of −70 mV. (B) Sodium current densities (pA/pF) of DRG neurons incubated with sera of three healthy controls or serum of patients 1, 2 and 3 for 1 h, 2 h, 24 h, 48 h and 72 h. Decreased sodium current densities were detectable after long-term treatment (72 h) of DRG neurons with sera of patients 1 and 3. Boxplots show medians as horizontal line within the box and means as white squares. 25th and 75th percentiles are given by the top and bottom of the box. Whiskers show the 1.5 times interquartile range and black squares represent outliers. (C) Current-voltage relationships of DRG sodium current densities treated with sera of healthy controls or anti-CNTN1 positive patients' sera for 1 h or 72 h. Error bars represent standard deviation (SD). Levels of significance tested by Mann-Whitney U: $*p < 0.05$, $**p < 0.01$.

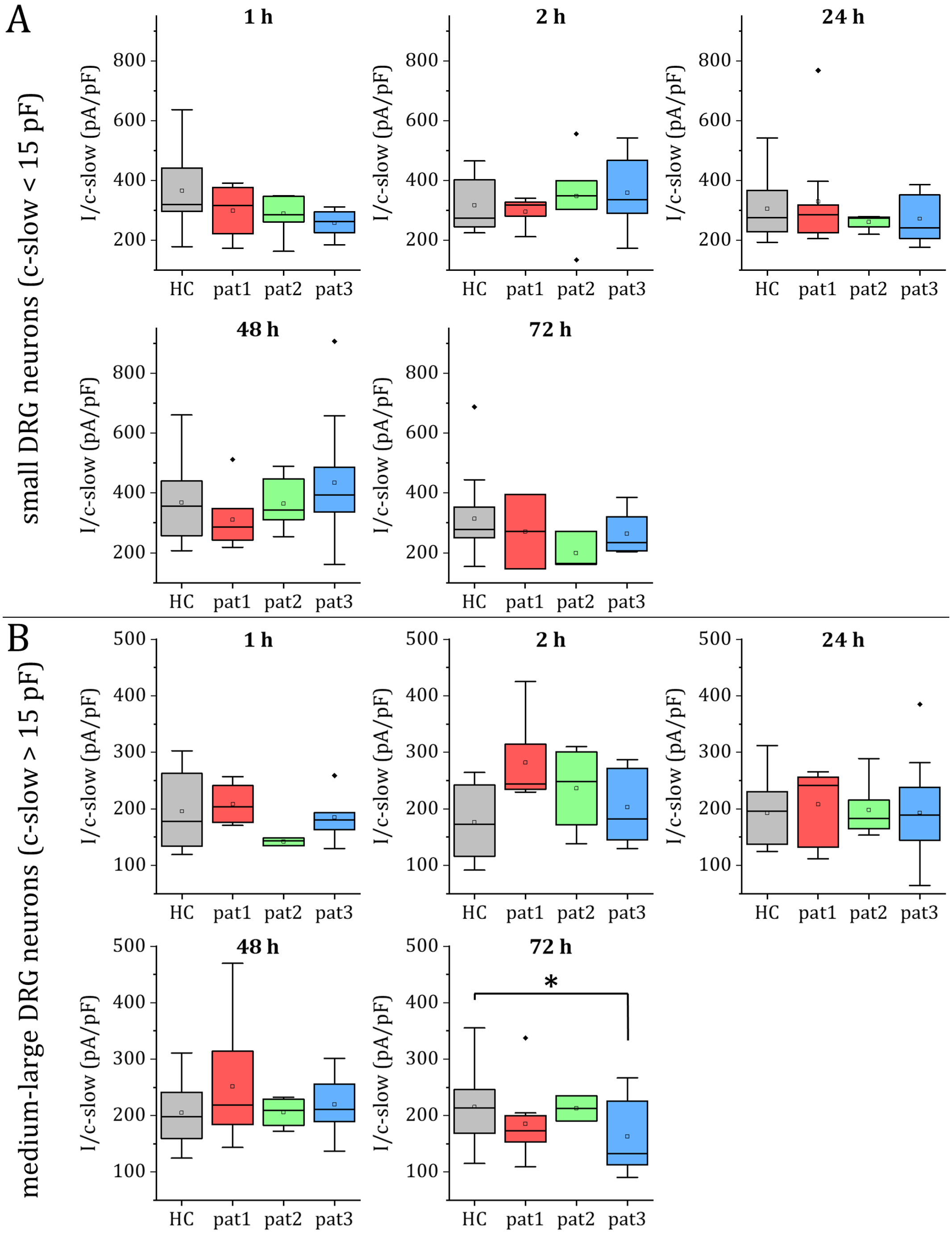

Figure 3.13: Reduction of sodium current densities by treatment with anti-CNTN1 autoantibodies is restricted to medium-large DRG neurons. Sodium current densities pA/pF of DRG neurons treated with sera of three healthy controls (HC), serum of patient 1 (pat1), PE material of patient 2 (pat2) or serum of patient 3 (pat3). (A) No alterations of sodium current densities in small DRG neurons with a cell capacitance of $< 15\,\text{pF}$ were detected for the different treatment groups. (B) Medium-large DRG neurons with a capacitance over 15 pF showed reduced sodium currents after long-term treatment with serum of patient 3 compared to the control group. Boxplots show medians as horizontal line within the box and means as white squares. 25th and 75th percentiles are given by the top and bottom of the box. Whiskers exhibit the 1.5 times interquartile range and black squares represent outliers. Significant differences between the treatment groups tested by Mann-Whitney U are marked by an asterisk ($*p < 0.05$).

3.3 Epitope characterization of anti-CNTN1 autoantibodies

Previously, epitopes of CNTN1 for autoantibodies from anti-CNTN1 positive CIDP patients have been investigated in two studies with contradictory results (Labasque et al., 2014; Miura et al., 2015). In both studies, cell-based assays were used to determine the binding site of autoantibodies at the CNTN1 protein. While Labasque et al. (2014) favored the requirement of *N*-linked glycosylation of CNTN1 within the immunoglobulin (Ig) domains for autoantibody binding, Miura et al. (2015) determined the Ig domains of CNTN1 as binding sites of autoantibodies even if the protein was unglycosylated. These contradictory results lead to the suspicion that anti-CNTN1 autoantibodies from different patients might target different epitopes of CNTN1. In the present study, constructs of CNTN1 where specific *N*-linked glycosylation sites were mutated and deletion mutants of the Ig domains were used in cell-based assays to investigate binding of anti-CNTN1 positive patients' sera. Furthermore, CNTN1 transfected human embryonic kidney (HEK) 293 cell lysates were treated with peptide-*N*-glycosidase F (PNGase F), which removes all *N*-linked glycosylations, in order to determine if autoantibodies recognize the protein core or the glycosylated protein.

3.3.1 Deglycosylation of CNTN1 does not prevent autoantibody binding *in vitro*

We first evaluated if *N*-linked glycosylations are involved in the recognition of CNTN1 by autoantibodies from anti-CNTN1 positive CIDP patients. Therefore, we generated constructs of CNTN1 substituting asparagine (one-letter symbol: N) residues within the typically N-X-S/T glycosylation sites into the structurally similar glutamine residues (Q). Each of the three *N*-glycosylation sites at amino acid residues 457, 473 and 494 were first mutated independently (N457Q, N473Q and N494Q). These constructs were then used to sequentially introduce double (N457,473Q; N457,494Q and N473,494Q) and triple mutations (N457,473,494Q) to the Ig5 domain of CNTN1. In order to detect binding of autoantibodies to the generated constructs, HEK 293 cells were transfected with the appropriate DNA and subsequently incubated with anti-CNTN1 positive patients' sera. As a positive control, we used a commercial antibody directed against CNTN1. As a negative control, transfected HEK 293 cells were incubated with serum of a healthy control. Furthermore, CNTN1 transfected HEK 293 cell lysates were treated with PNGase F to remove all *N*-linked glycosylations from the protein and immunoblotted against CNTN1 or sera of anti-CNTN1 positive patients or a healthy control.

In the HEK 293 cell binding assays, the anti-CNTN1 antibody showed binding to the unmodified CNTN1 protein as well as to all glycosylation mutants (Fig. 3.14, A, B). Using Western blot analysis we were able to detect binding to the glycosylated CNTN1 protein at around 140 kDa as well as to the deglycosylated protein at around 110 kDa (Fig. 3.14, C). Similar to anti-CNTN1, serum of patient 1 and PE material of patient 2 recognized the unmodified protein and all constructs of CNTN1 modified for their glycosylation sites in the Ig5 domain (Fig. 3.14, A, B). However, we could not detect any binding of both patients' samples after immunoblotting neither to the glycosylated nor to the unglycosylated protein treated with PNGase F (Fig. 3.14, C). This may be due to a conformational epitope which is destroyed during sodium dodecyl sulfate-polyacrylamide gel electrophoresis (SDS-PAGE) when the protein is denatured.

Sera of patients 3, 4 and 5 showed binding to HEK 293 cells transfected with the unmodified CNTN1 DNA as well as to HEK 293 cells transfected with single, double and triple glycosylation mutants of CNTN1 (Fig. 3.15, A, B). Sera of patients 3 and 4 reacted against the two glycosylated forms of CNTN1 at around 140 kDa appearing as a protein doublet (Fig. 3.15, C). After removal of all N-glycosylations from the protein by treatment of CNTN1 transfected HEK 293 cell lysates with PNGase F, binding of sera from patients 3 and 4 was still detectable by immunoblotting at around 110 kDa (Fig. 3.15, C). In contrast, serum of patient 5 neither showed binding to the glycosylated nor to the deglycosylated protein (Fig. 3.15, C), suggesting that autoantibodies from this patient are directed against a conformational epitope of CNTN1.

Furthermore, binding of sera from patients 6 and 7 to HEK 293 cells transfected with the unmodified protein as well as to all established glycosylation mutants of CNTN1 was observed (Fig. 3.16, A, B). To investigate if other N-glycans are involved in the recognition of CNTN1 by autoantibodies from these patients, the protein was treated with PNGase F. After immunoblotting, binding to the glycosylated as well as the unglycosylated form of CNTN1 was detected (Fig. 3.16, C). As a negative control, HEK 293 cells expressing either the unmodified protein or CNTN1 lacking specific N-glycans in the Ig5 domain were incubated with serum of a healthy control. No binding was detectable to the unmodified protein or the N-glycosylation mutants (Fig. 3.16, A, B). Additionally, serum of a healthy control was used for immunoblotting of CNTN1 with or without treatment with PNGase F. Here again, we were unable to detect any binding neither to the glycosylated nor to the unglycosylated protein (Fig. 3.16, C).

In summary, samples from all anti-CNTN1 positive patients recognized both the glycosylated form of CNTN1 as well as the protein lacking specific N-glycans. Therefore, the epitope of CNTN1 for our patients' autoantibodies has to be located in the protein core or a conformational epitope is involved in the recognition.

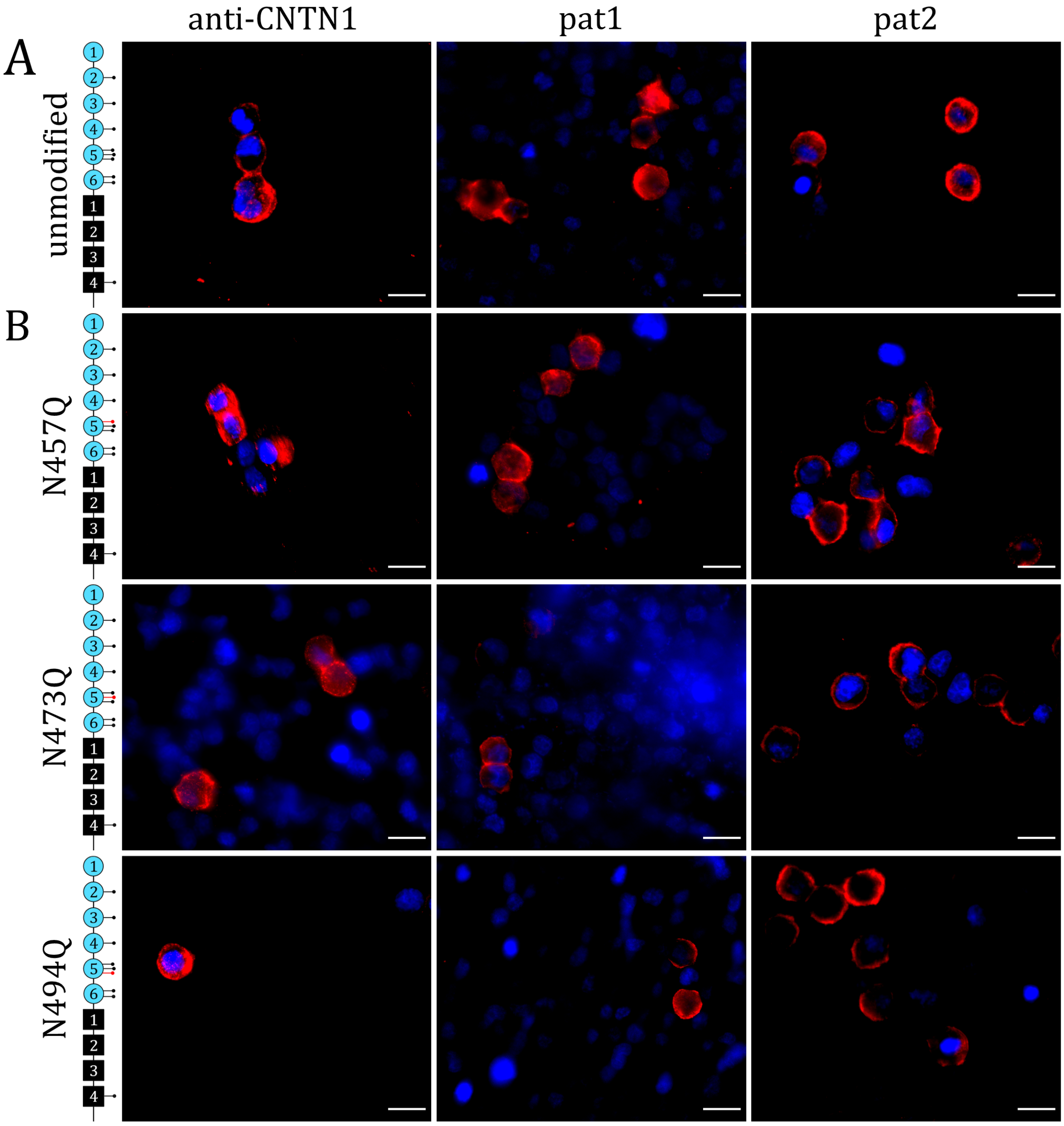

Figure 3.14: Binding assays of anti-CNTN1 and sera of patients 1 and 2 to glycosylation mutants of CNTN1. HEK 293 cells were transfected with unmodified CNTN1 DNA (A) or constructs of CNTN1 with specific mutated *N*-glycosylation sites (B). Living cells were then incubated with a commercial antibody against CNTN1 or sera of the anti-CNTN1 positive patients 1 (pat1) and 2 (pat2). Binding of anti-CNTN1 antibodies and patients' sera to the unmodified protein as well as to all glycosylation mutants of CNTN1 was detectable. DAPI (blue) was used to stain the nucleus. Scale bars refer to 20 µm. (C) To investigate the deglycosylated protein, HEK 293 cell lysates transfected with CNTN1 were treated with PNGase F (+) or untreated (-) and immunoblotted against CNTN1 or sera of anti-CNTN1 positive pat1 and pat2. The anti-CNTN1 antibody recognized the glycosylated protein around 140 kDa as well as the deglycosylated protein (red arrows). No binding was detectable for sera of pat1 and pat2 neither for the native protein nor for the deglycosylated CNTN1. β-actin was used as a loading control.

Figure continued on next page.

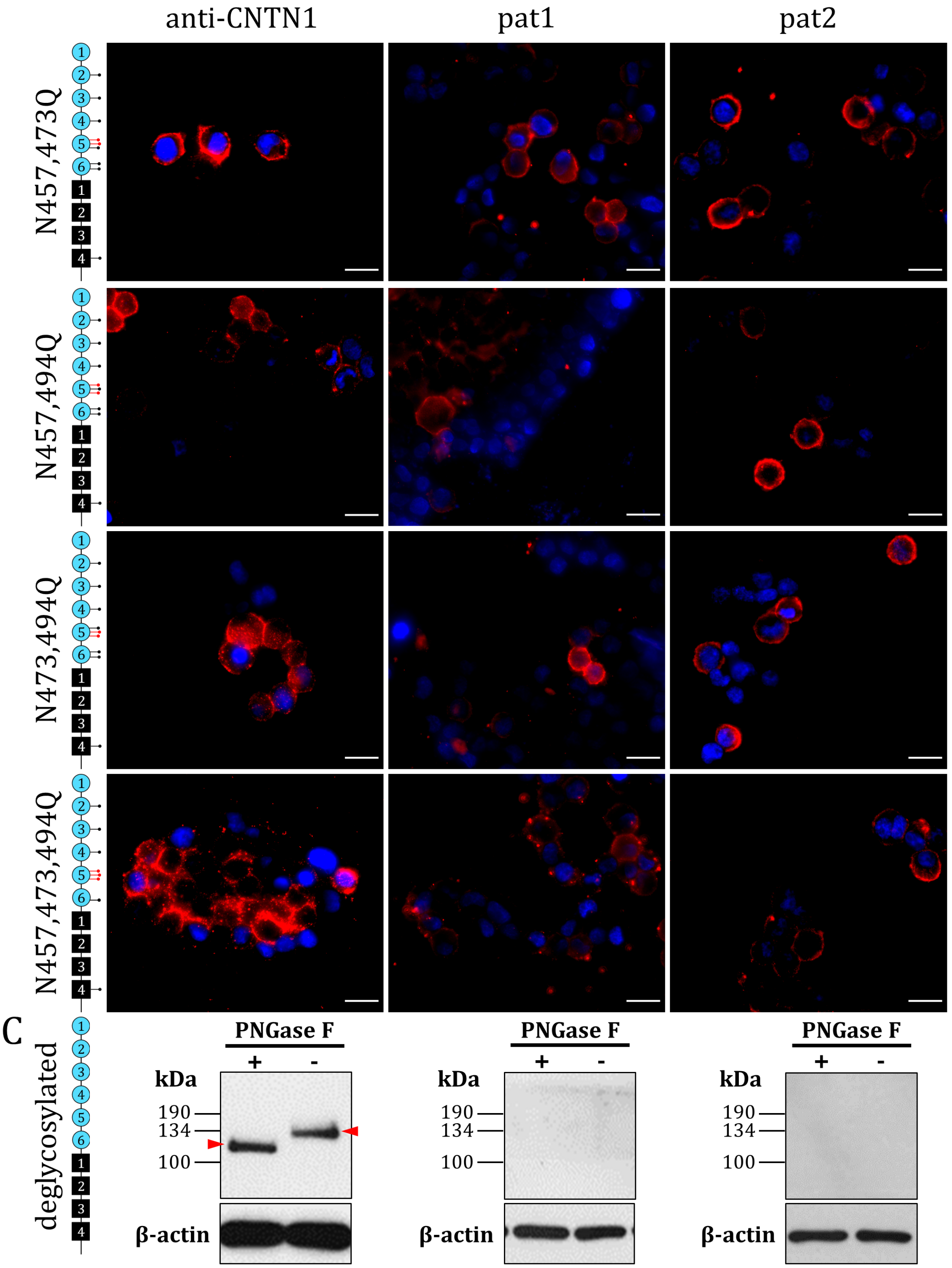

Figure 3.14 *continued*

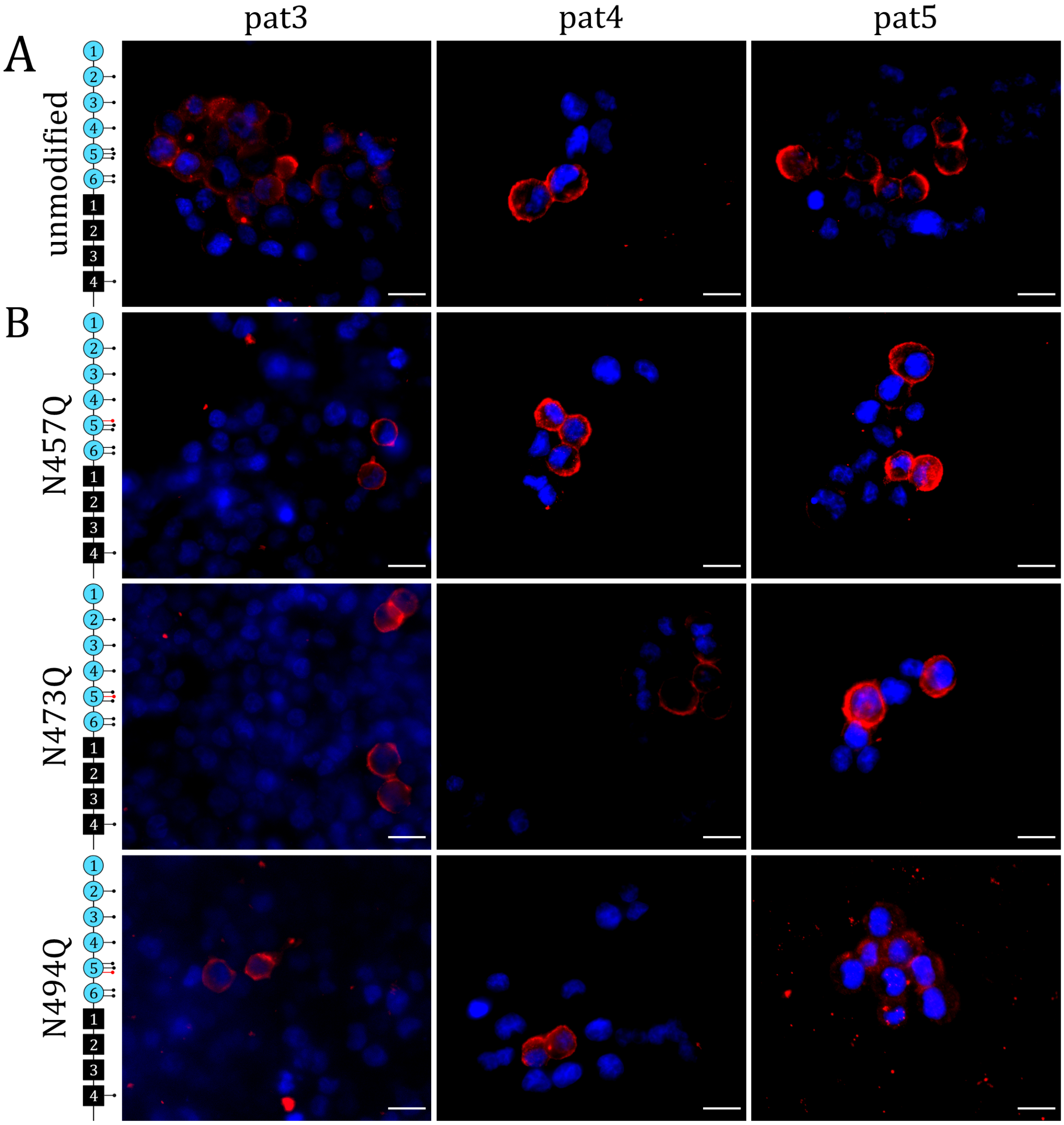

Figure 3.15: Binding assays of sera of patients 3, 4 and 5 to glycosylation mutants of CNTN1. HEK 293 cells were transfected with unmodified CNTN1 DNA (A) or constructs of CNTN1 with specific mutated *N*-glycosylation sites (B). Living cells were then incubated with sera of the anti-CNTN1 positive patients 3 (pat3), 4 (pat4) and 5 (pat5). Binding of patients' sera to the unmodified protein as well as to all glycosylation mutants of CNTN1 was detectable. DAPI (blue) was used to label nuclei. Scale bars refer to 20 µm. (C) To investigate the deglycosylated protein, HEK 293 cell lysates transfected with CNTN1 were treated with PNGase F (+) or untreated (-) and immunoblotted against sera from anti-CNTN1 positive pat3, pat4 and pat5. Sera from pat3 and pat4 recognized the glycosylated protein around 140 kDa as well as the deglycosylated protein (red arrows). No binding was detectable for serum of pat5 neither for the native protein nor for the deglycosylated CNTN1. β-actin was used as a loading control.

Figure continued on next page.

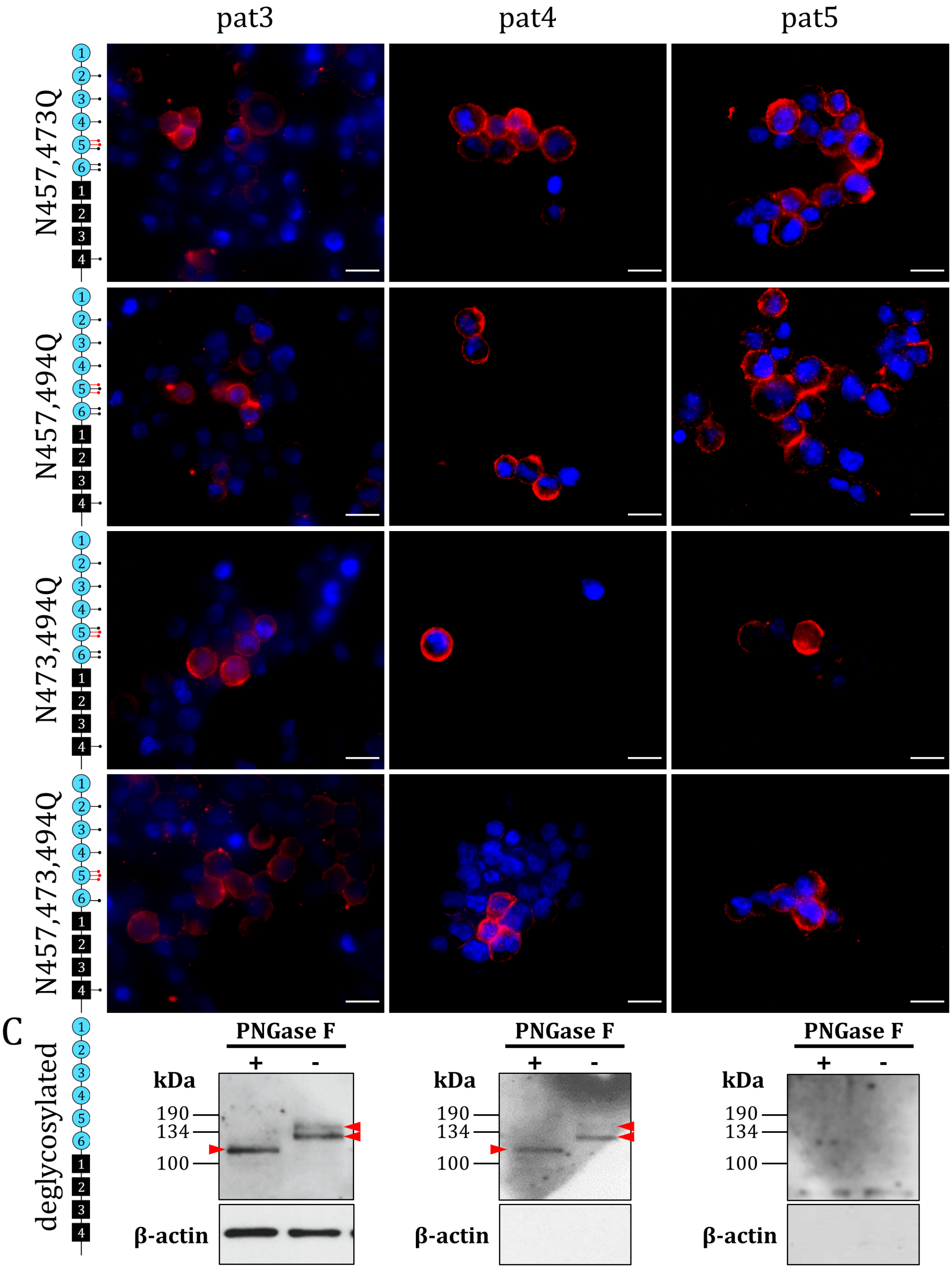

Figure 3.15 *continued*

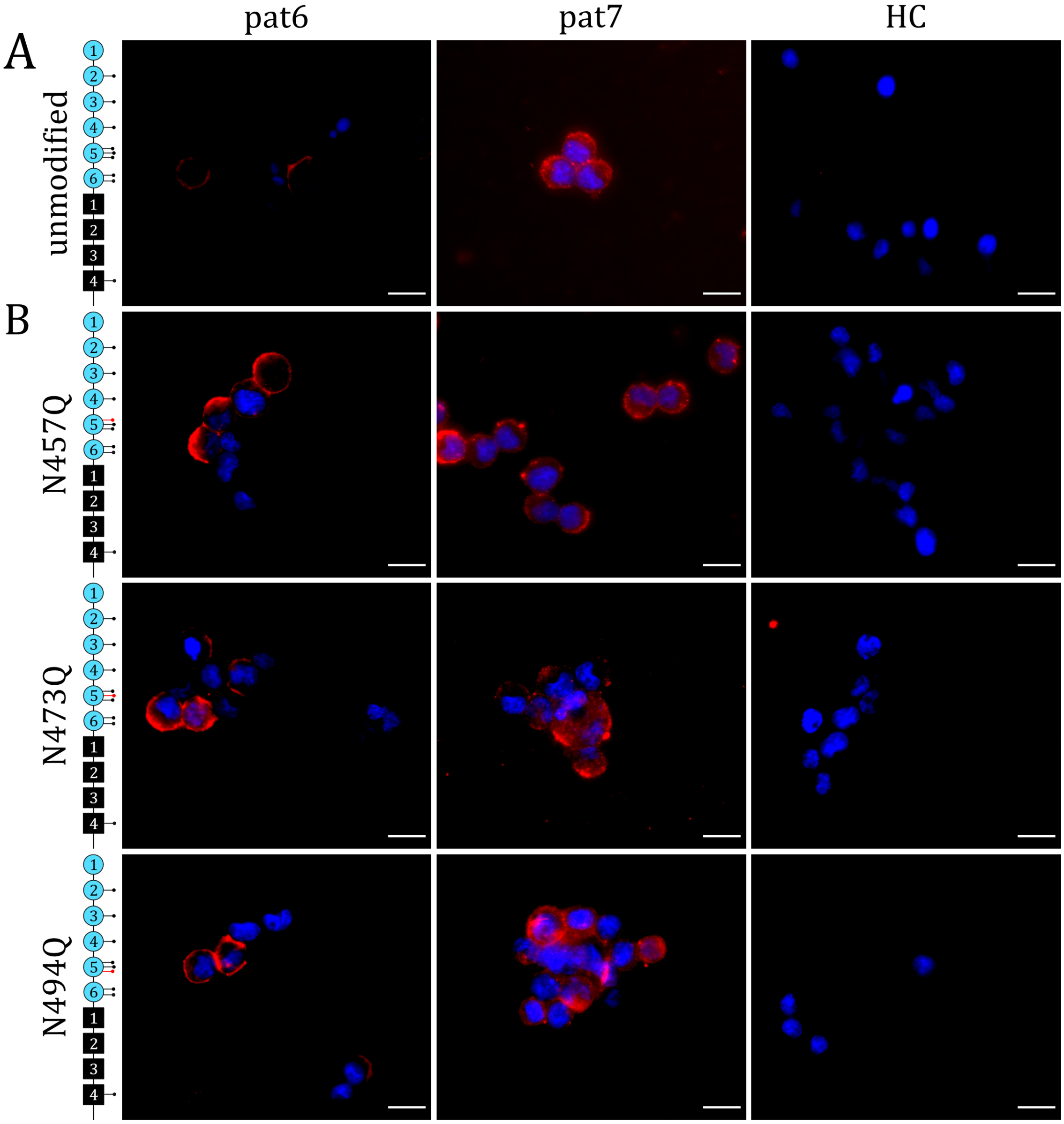

Figure 3.16: Binding assays of sera of patients 6 and 7 or serum of a healthy control to glycosylation mutants of CNTN1. HEK 293 cells were transfected with unmodified CNTN1 DNA (A) or constructs of CNTN1 with specific mutated *N*-glycosylation sites (B). Living cells were then incubated with sera of the anti-CNTN1 positive patients 6 (pat6) and 7 (pat7) or serum of a healthy control (HC). Binding of patients' sera to the unmodified protein as well as to all glycosylation mutants of CNTN1 was detectable. No binding was observed after incubation of a HC. DAPI (blue) was used to stain cell nuclei. Scale bars refer to 20 µm. (C) To investigate the deglycosylated protein, HEK 293 cell lysates transfected with CNTN1 were treated with PNGase F (+) or untreated (-) and immunoblotted sera from anti-CNTN1 positive pat6 and pat7 or serum from a HC. Sera of both patients recognized the glycosylated protein around 140 kDa as well as the deglycosylated protein (red arrows). No binding was detectable for serum of a HC. β-actin was used as a loading control.

Figure continued on next page.

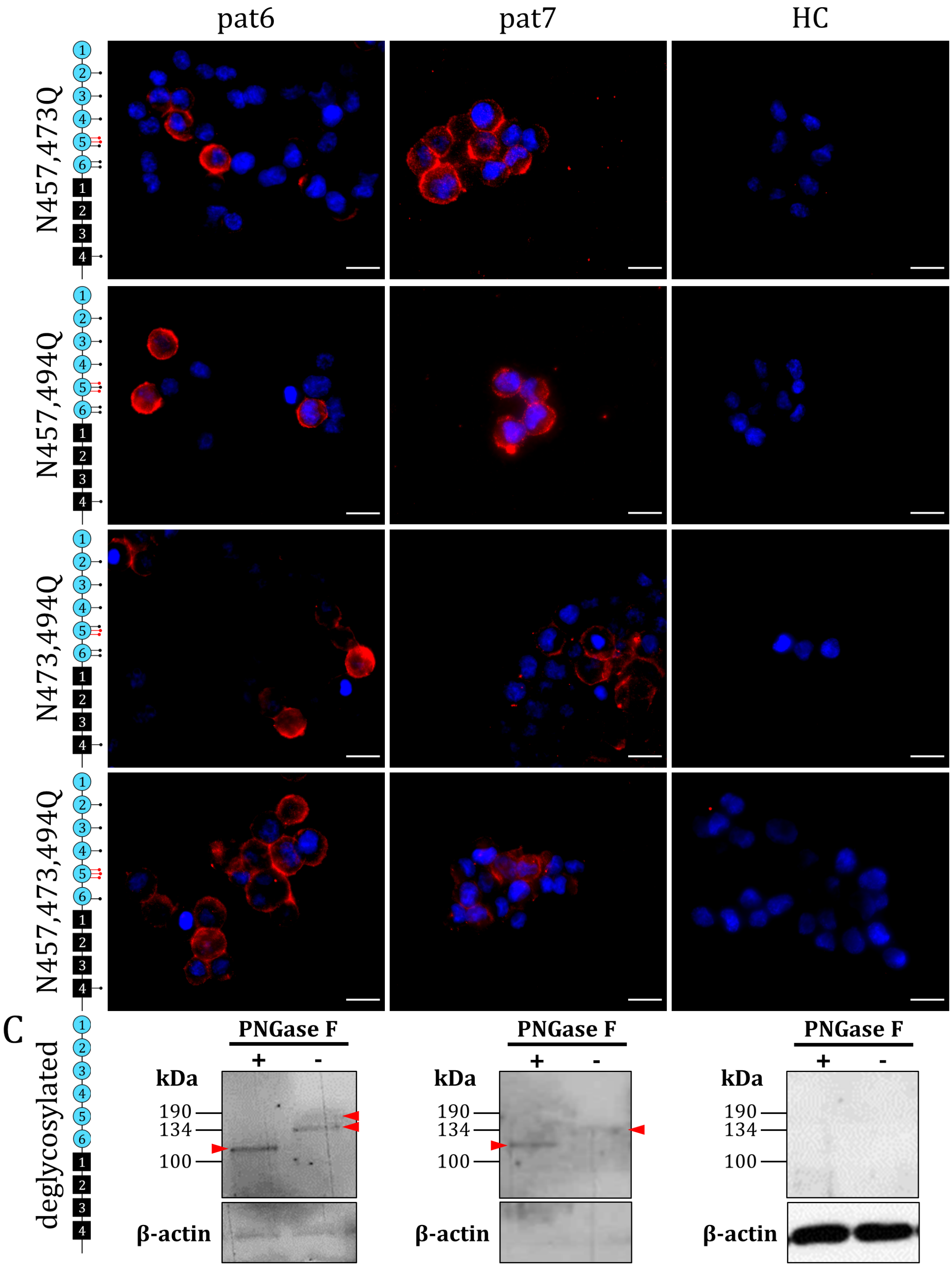

Figure 3.16 *continued*

3.3.2 Anti-CNTN1 autoantibodies recognize different epitopes

We further investigated the protein core to identify the specific binding site in the protein. Therefore, the Ig domains were consecutively truncated from the protein until the fibronectin type III (FnIII) domains were left. To verify if the modified CNTN1 protein is still expressed, fusion constructs with enhanced green fluorescent protein (eGFP) were generated.

Fixed transfected HEK 293 cells were incubated with anti-CNTN1 or patients' sera and appropriate secondary antibodies to analyze binding of antibodies to the modified CNTN1 constructs. Untransfected cells incubated with anti-CNTN1 or patients' samples were used as negative controls. Due to high background signal from patients' sera or PE material, comparisons with untransfected cells were indispensable to differentiate between specific binding and unspecific signal.

Untransfected HEK 293 cells showed only very weak and unspecific signal after incubation with a commercial anti-CNTN1 antibody (Fig. 3.17). In contrast, antibodies bind specifically to cells transfected with the unmodified wild-type CNTN1 DNA. After removing the first Ig domain from the CNTN1 protein, anti-CNTN1 antibodies still recognize the protein (Fig. 3.17). Similarly, anti-CNTN1 binds specifically to all deletion constructs of CNTN1 (Fig. 3.17) indicating that the binding site for the commercial anti-CNTN1 antibody is located in the FnIII domains of the protein.

Incubation of untransfected HEK 293 cells with serum of the anti-CNTN1 positive patient 1 led to a higher background signal compared to the incubation with anti-CNTN1 (Fig. 3.18). In contrast, patient's autoantibodies bind specifically to HEK 293 cells transfected with the unmodified CNTN1 DNA (Fig. 3.18). However, binding gets lost after removing the first Ig domain of the CNTN1 protein (Fig. 3.18) suggesting that the binding site for anti-CNTN1 autoantibodies from patient 1 is located in the first Ig domain or that a conformational epitope is targeted by the autoantibodies. As a control for showing that binding is lost, HEK 293 cells transfected with CNTN1 lacking the first two Ig domains were incubated with serum of patient 1. Here again, only unspecific signal was detectable (Fig. 3.18).

PE material of the anti-CNTN1 positive patient 2 showed a very high unspecific background signal in HEK 293 cell-based assays. However, in contrast to untransfected cells, a specific binding pattern of anti-CNTN1 autoantibodies to cells transfected with the wild-type CNTN1 DNA was detectable (Fig. 3.19). Binding of autoantibodies from patient 2 is not prevented by removing the first Ig domain of the protein (Fig. 3.19). By contrast, after incubation of cells transfected with CNTN1 lacking the first two Ig domains with PE material from patient 2, binding gets lost (Fig. 3.19). In binding assays with HEK 293 cells transfected with CNTN1, where the first three Ig domains were removed, no specific signal was detectable as well (Fig. 3.19) suggesting that the epitope is located in the first two Ig domains.

Untransfected cells did not show any specific signal after incubation with serum of patient 3 (Fig. 3.20). However, at cells transfected with the wild-type CNTN1 DNA, clear binding of autoantibodies was detectable (Fig. 3.20). Interestingly, this binding was not prevented by any of the generated CNTN1 constructs (Fig. 3.20) indicating that the binding site for anti-CNTN1 autoantibodies from patient 3 is located in the FnIII domains and not in the Ig domains of the protein.

Similarly, serum of the anti-CNTN1 positive patient 4 binds specifically to all CNTN1 constructs (Fig. 3.21). Although incubation of HEK 293 cells with serum of patient 4 led to a very high background signal (also in untransfected cells, Fig. 3.21), a specific binding pattern was only detectable at cells transfected with the CNTN1 constructs. Therefore, the epitope for anti-CNTN1 autoantibodies from patient 4 is located in the FnIII domains of CNTN1.

For the anti-CNTN1 positive patient 5, we could only detect a specific binding at HEK 293 cells transfected with the unmodified wild-type CNTN1 DNA (Fig. 3.22). The specific binding pattern was lost after deletion of the first Ig domain from the protein (Fig. 3.22). As a control, cells transfected with CNTN1 lacking the first two Ig domains were incubated with serum of patient 5. No specific staining was detectable (Fig. 3.22). This suggests that the binding site for anti-CNTN1 autoantibodies from patient 5 is located in the first Ig domain of the CNTN1 protein or that autoantibodies react against a conformational epitope which gets lost after removing the first Ig domain.

As patient's material is limited, we were not able to investigate sera from patients 6 and 7 in the cell-based assay. However, serum of patient 8 showed a binding pattern comparable to sera of patients 1 and 5. Thus, specific binding was only detectable at cells transfected with the wild-type CNTN1 DNA and was prevented by removing the first Ig domain of the protein (Fig. 3.23). Therefore, the binding site for autoantibodies of patient 8 has to be at a conformational epitope or it is located in the first Ig domain of CNTN1.

Table 3.4 shows a summary of the results from the epitope characterization for all patients highlighting that there may be two distinct groups of anti-CNTN1 autoantibodies: 1. autoantibodies directed against the Ig domains or a conformational epitope, 2. autoantibodies directed against the FnIII domains.

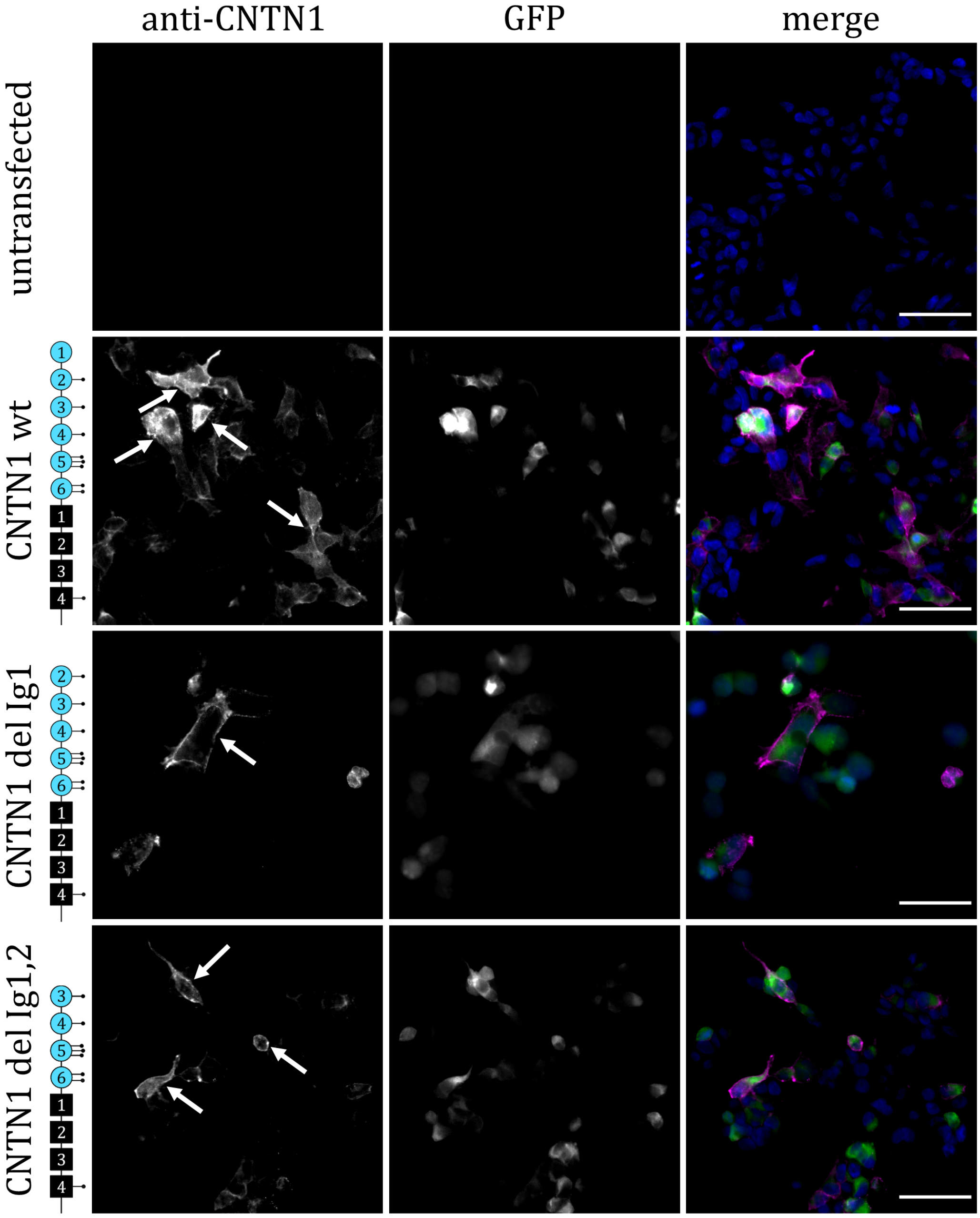

Figure 3.17: Specific binding of anti-CNTN1 to all deletion mutants of CNTN1. HEK 293 cells were transiently transfected with fusion constructs of CNTN1 and eGFP (green), fixed and incubated with anti-CNTN1 (magenta) and appropriate secondary antibodies. Cell nuclei are marked with DAPI. Untransfected cells do not express CNTN1 and no binding of anti-CNTN1 is detectable. In contrast, anti-CNTN1 is specifically directed against the unmodified wild-type (CNTN1 wt) protein. A specific signal of anti-CNTN1 was also detectable at cells transfected with the construct where the first Ig domain is deleted (CNTN1 del Ig1) and the fusion construct lacking the first two Ig domains (CNTN1 del Ig1,2). Deletion of further Ig domains (CNTN1 del Ig1,2,3, CNTN1 del Ig1-4, CNTN1 del Ig 1-5 and CNTN1 del Ig1-6) did not prevent anti-CNTN1 from binding against the protein. White arrows mark specific binding. Scale bars refer to 50 µm.

Figure continued on next page.

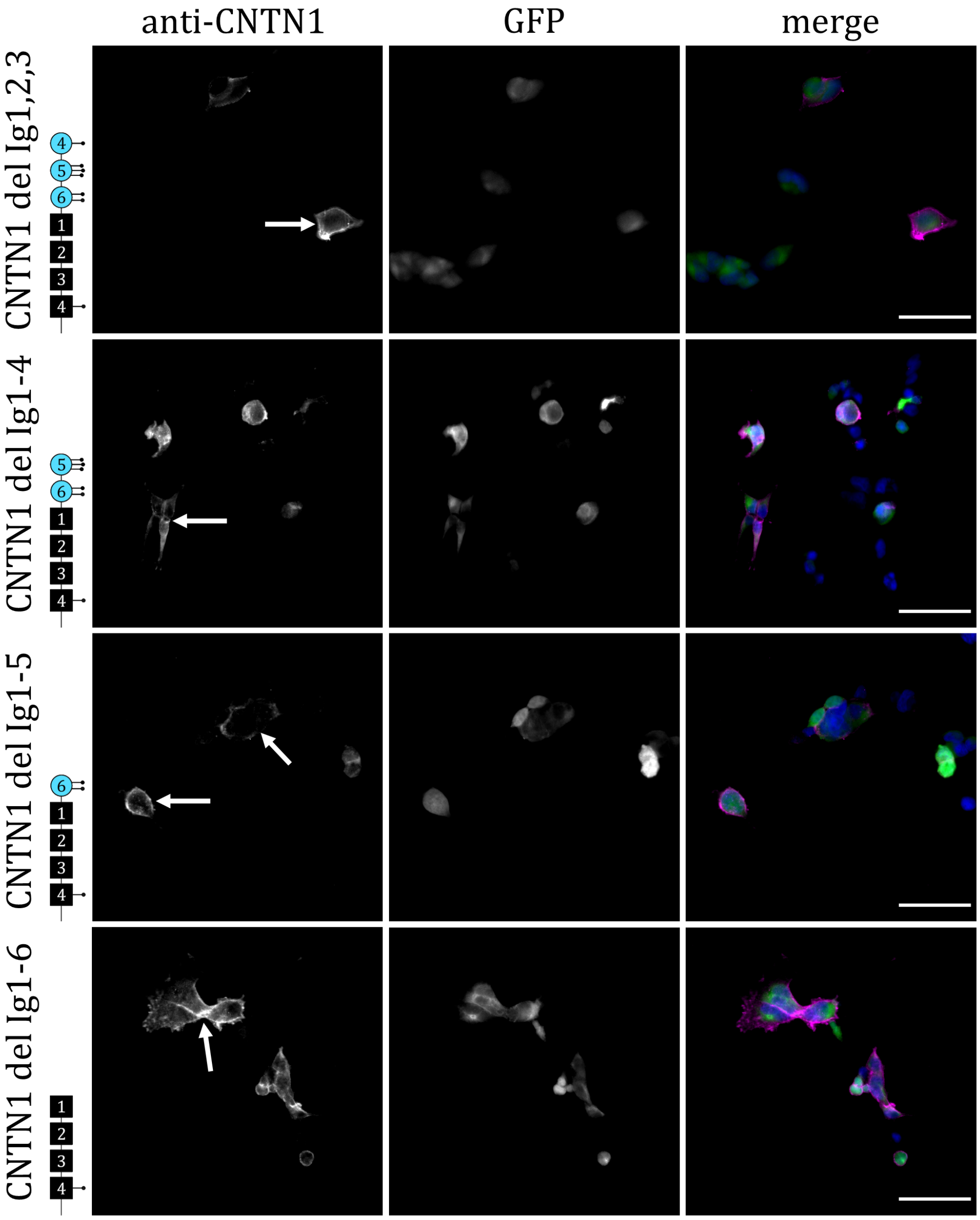

Figure 3.17 *continued*

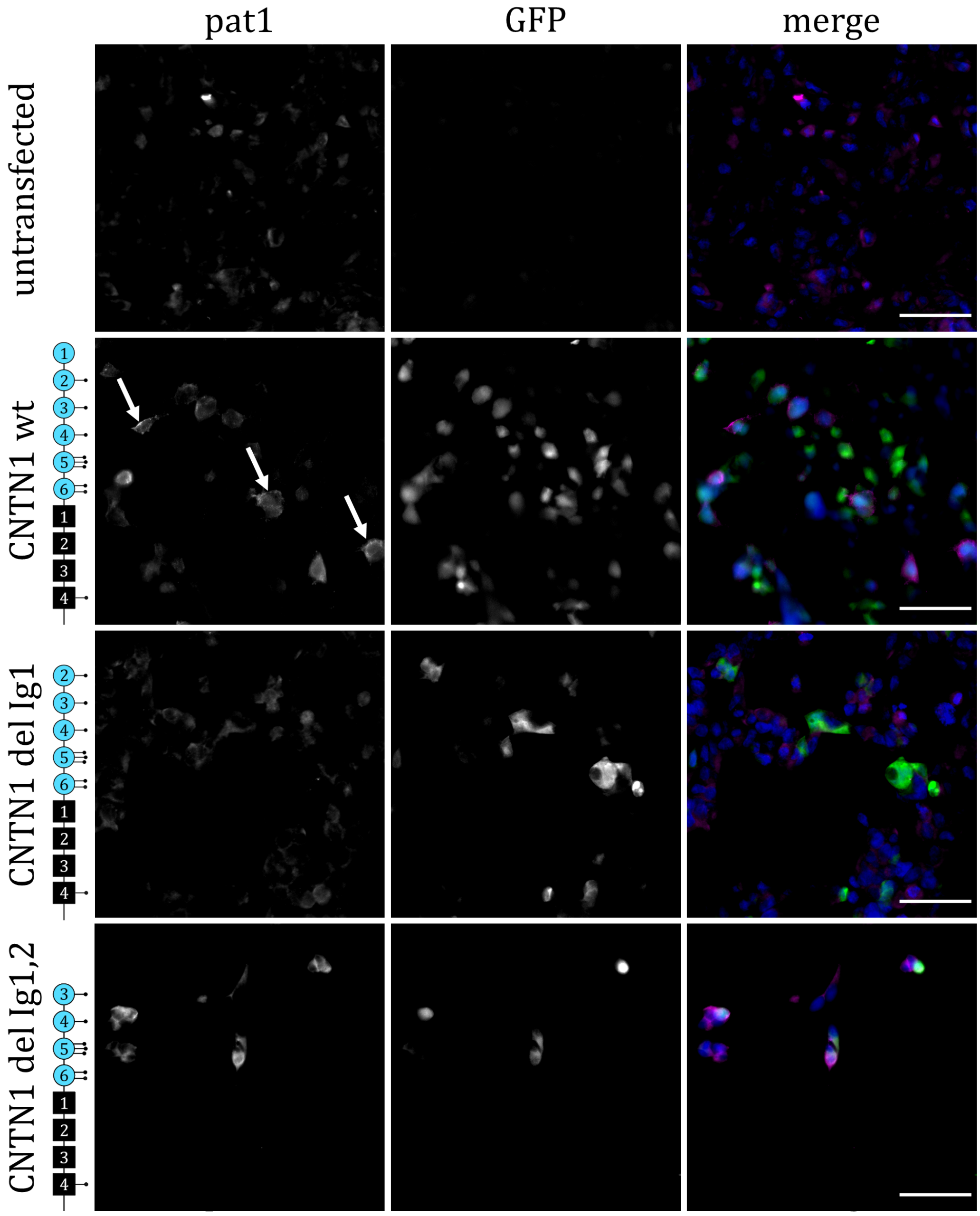

Figure 3.18: Binding assays of serum from the anti-CNTN1 positive patient 1 to deletion mutants of CNTN1. HEK 293 cells were transiently transfected with fusion constructs of CNTN1 and eGFP (green), fixed and incubated with serum of the anti-CNTN1 positive patient 1 (pat1, magenta) and appropriate secondary antibodies. Cell nuclei are marked with DAPI (blue). Untransfected cells do not express CNTN1 and only weak and unspecific staining of serum of pat1 is detectable. By contrast, autoantibodies of pat1 are specifically directed against the unmodified wild-type (CNTN1 wt) protein. However, deletion of the first Ig domain (CNTN1 del Ig1) prevents binding of pat1 autoantibodies against CNTN1. Absence of specific binding was proven on HEK 293 cells transfected with CNTN1 lacking the first two Ig domains (CNTN1 del Ig1,2). White arrows mark specific binding. Scale bars refer to 50 µm.

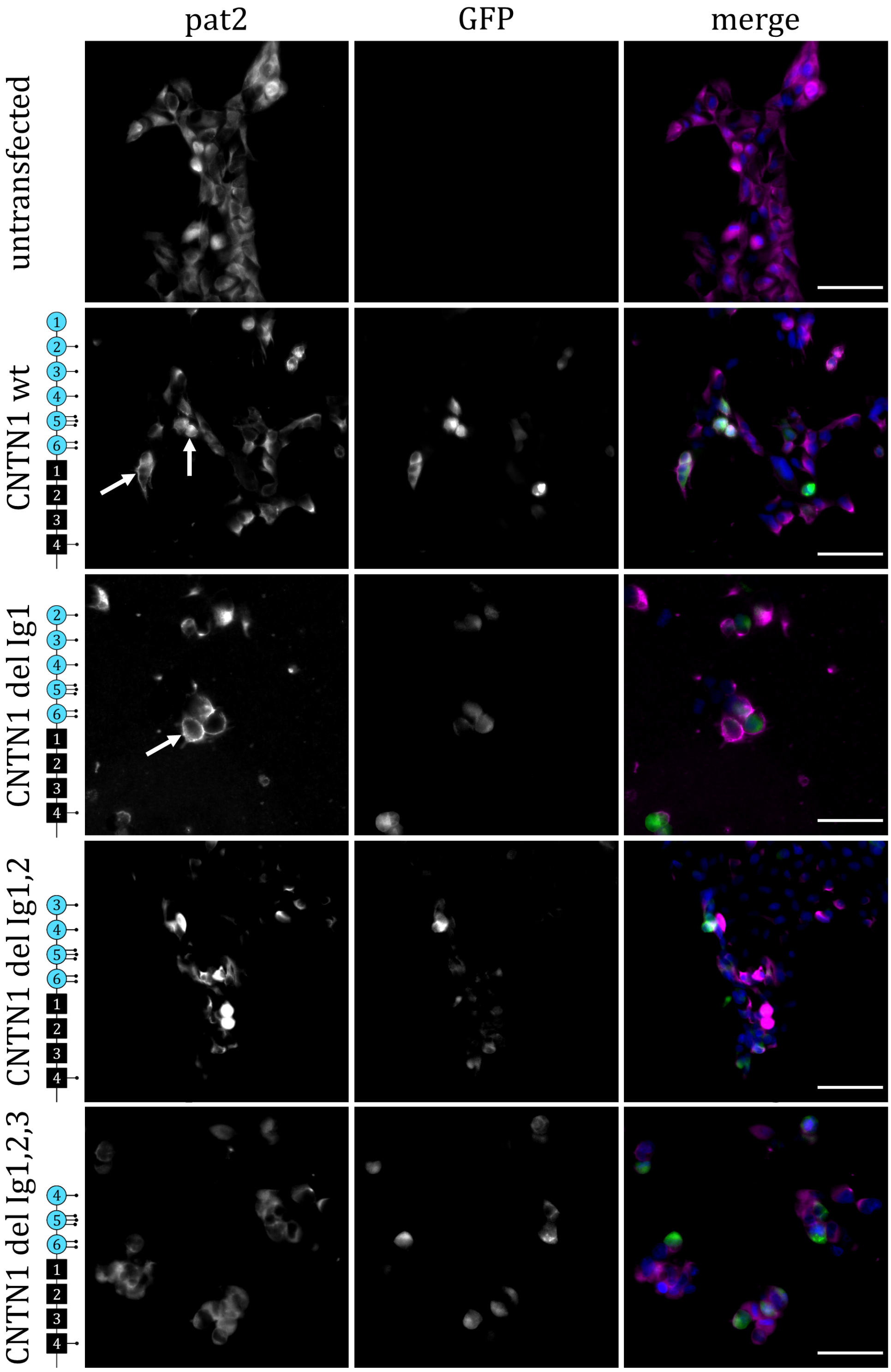

Figure 3.19: Binding of PE material from patient 2 is lost after deletion of the first two Ig domains of CNTN1. HEK 293 cells were transfected with constructs of CNTN1 fused to eGFP (green), fixed and incubated with PE material of patient 2 (pat2, magenta) and appropriate secondary antibodies. Cell nuclei are marked with DAPI (blue). Untransfected cells showed only weak signal from the PE material. By contrast, PE material of pat2 specifically bound to the unmodified protein (CNTN1 wt) and to CNTN1 lacking the first Ig domain (CNTN1 del Ig1). Binding gets lost when the second Ig domain is truncated (CNTN1 del Ig 1,2). Similarly, no specific binding to CNTN1 lacking the first three Ig domains (CNTN1 del Ig1,2,3) is observable. White arrows mark specific binding. Scale bars: 50 µm.

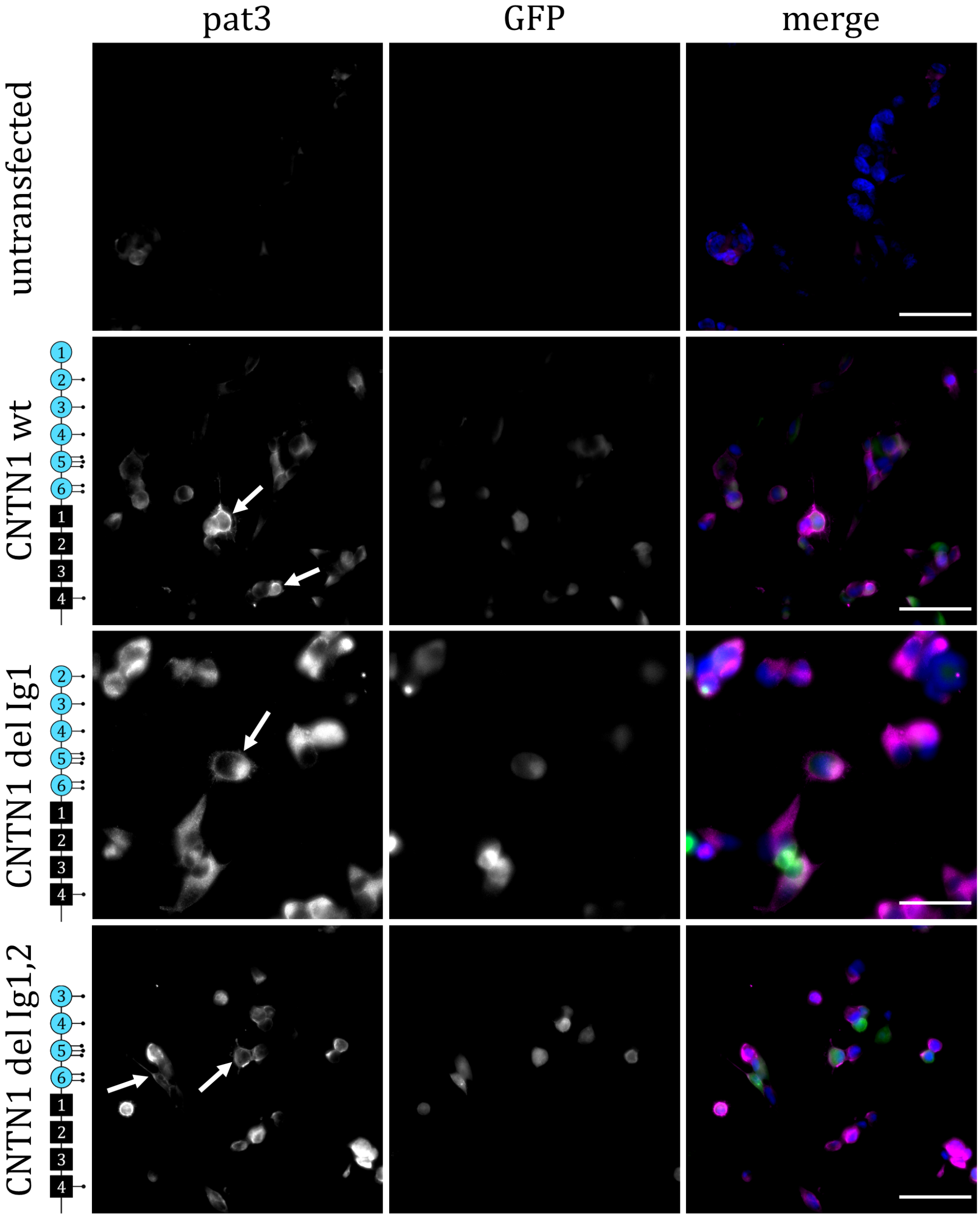

Figure 3.20: Autoantibodies from the anti-CNTN1 positive patient 3 are directed against the FnIII domains of CNTN1. HEK 293 cells were transiently transfected with fusion constructs of CNTN1 and eGFP (green), fixed and incubated with serum of the anti-CNTN1 positive patient 3 (pat3, magenta) and appropriate secondary antibodies. Cell nuclei are marked with DAPI. Untransfected cells showed only a low background signal from the serum. In contrast, autoantibodies from pat4 specifically bound the unmodified wild-type (CNTN1 wt) protein and all deletion constructs of CNTN1 (CNTN1 del Ig1 to CNTN1 del Ig1-6). White arrows mark specific binding. Scale bars refer to 50 µm.

Figure continued on next page.

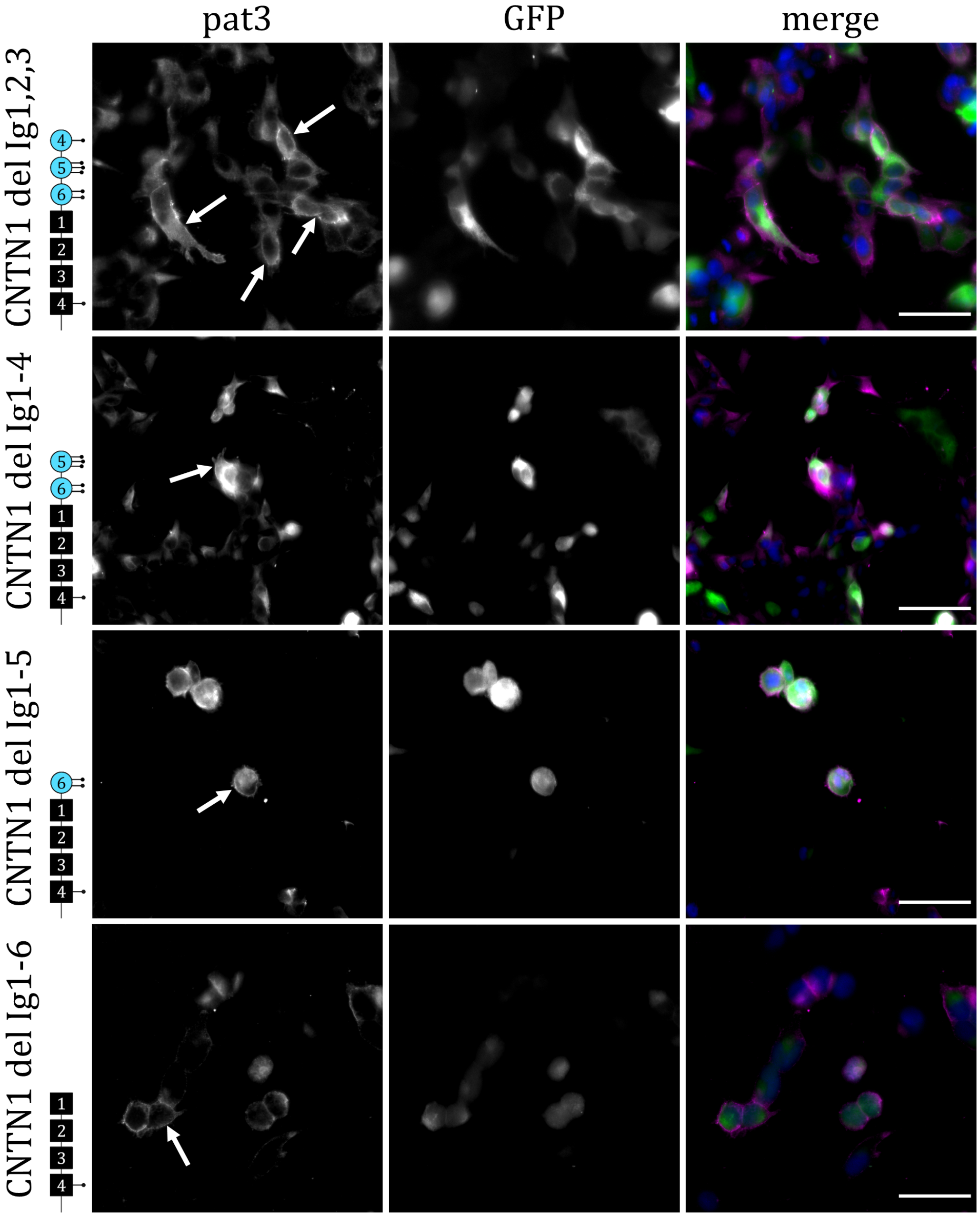

Figure 3.20 *continued*

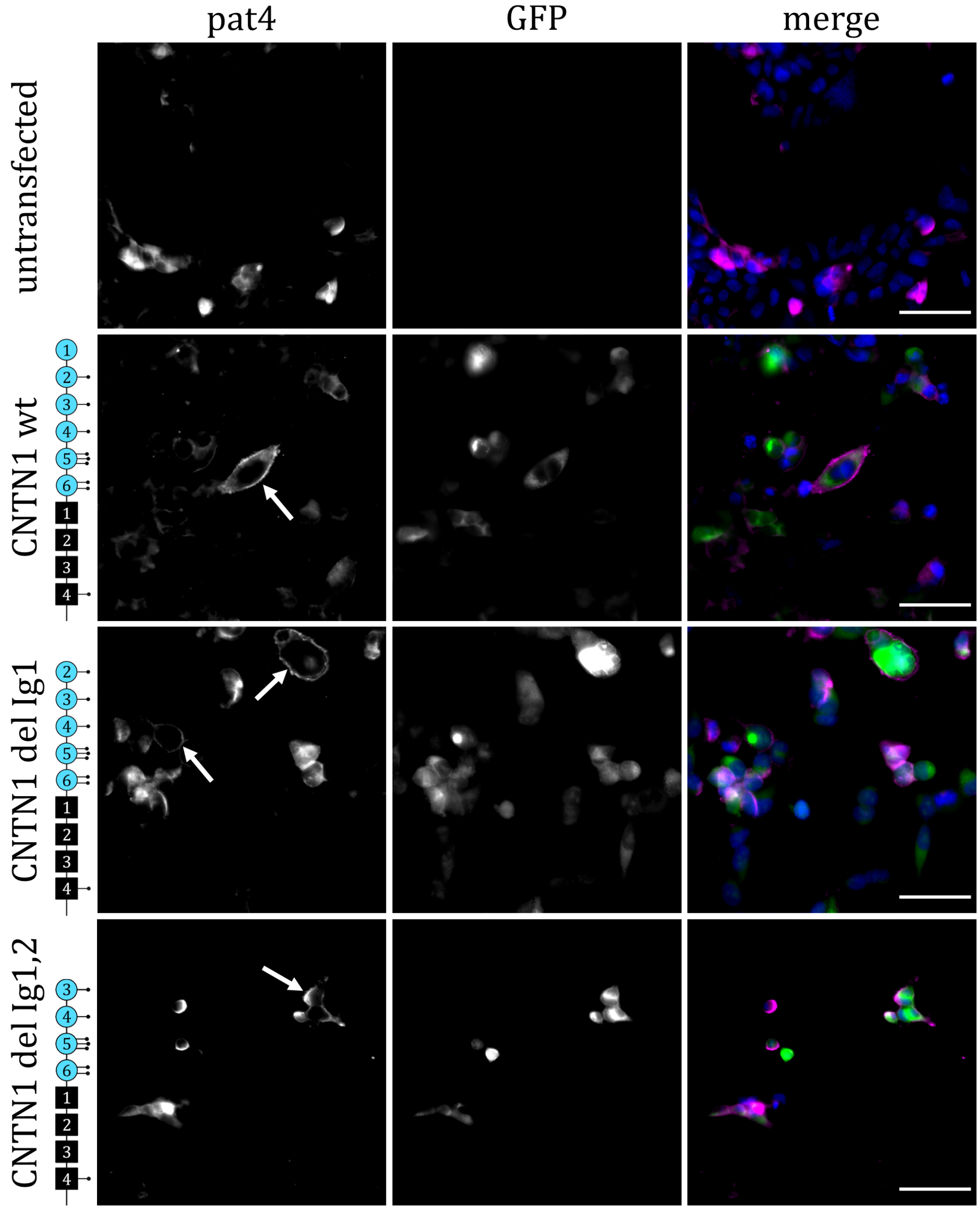

Figure 3.21: Binding site of anti-CNTN1 autoantibodies from patient 4 is not located in the Ig domains of CNTN1. HEK 293 cells were transiently transfected with fusion constructs of CNTN1 and eGFP (green), fixed and incubated with serum of the anti-CNTN1 positive patient 4 (pat4, magenta) and appropriate secondary antibodies. Cell nuclei are marked with DAPI. Untransfected cells do not express CNTN1 and only unspecific signal from the serum is detectable. In contrast, autoantibodies from pat4 are specifically directed against the unmodified wild-type (CNTN1 wt) protein and all analyzed CNTN1 deletion constructs (CNTN1 del Ig1 to CNTN1 del Ig1-6). White arrows mark specific binding. Scale bars refer to 50 µm.

Figure continued on next page.

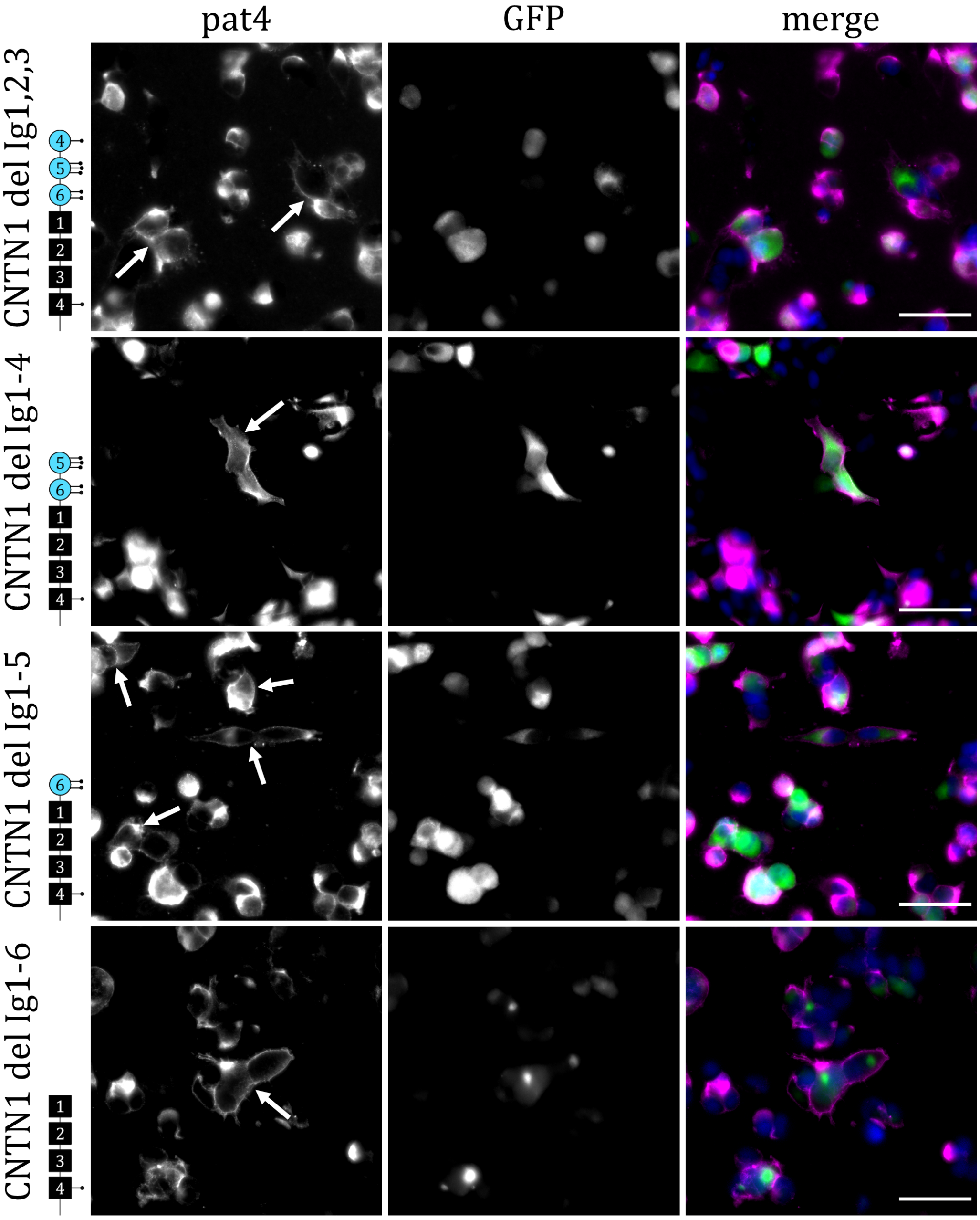

Figure 3.21 *continued*

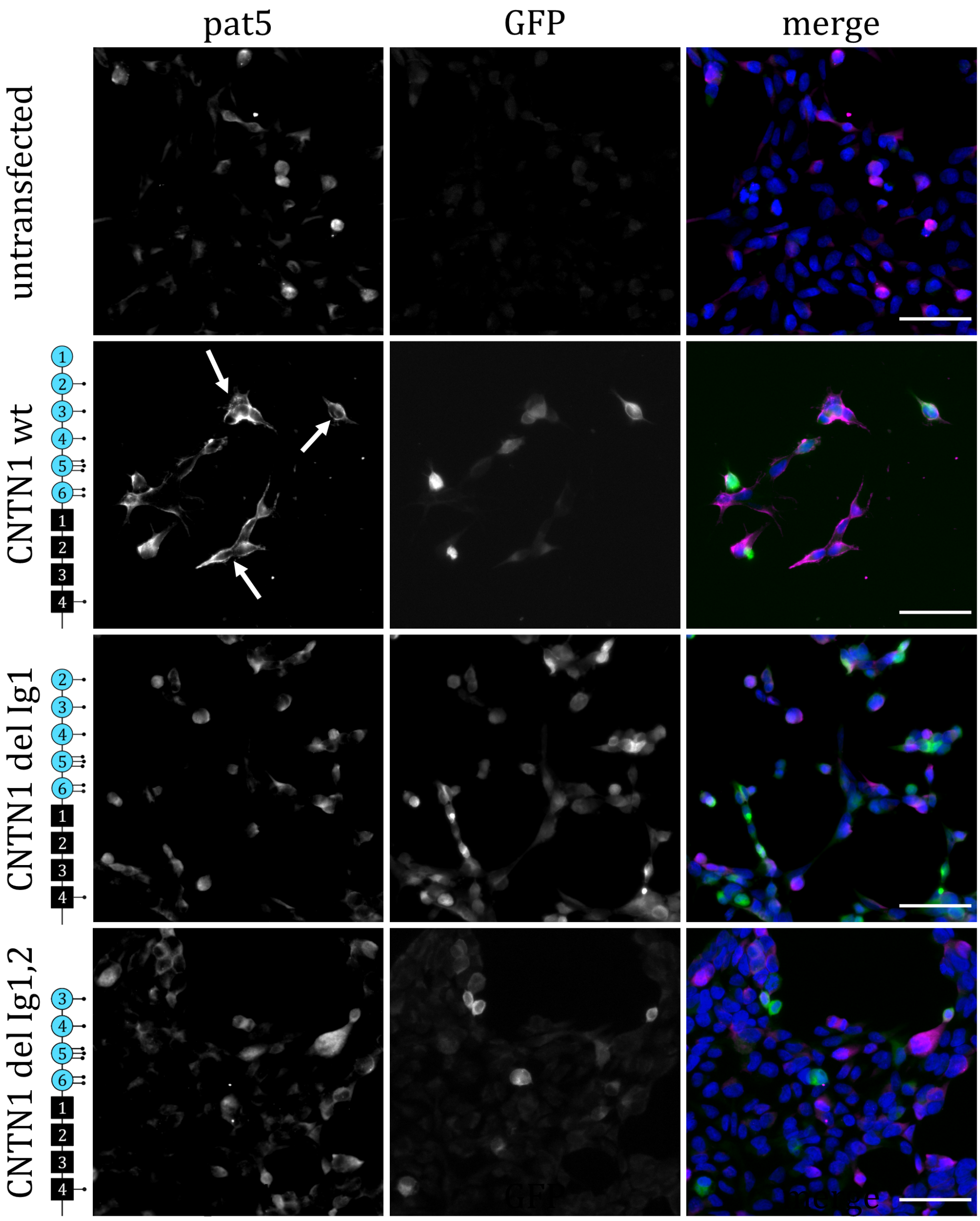

Figure 3.22: Binding of the anti-CNTN1 positive serum from patient 5 is prevented after deletion of the first Ig domain of CNTN1. HEK 293 cells were transiently transfected with fusion constructs of CNTN1 and eGFP (green), fixed and incubated with serum of the anti-CNTN1 positive patient 5 (pat5, magenta) and appropriate secondary antibodies. Cell nuclei are marked with DAPI. In untransfected cells, no expression of CNTN1 and only unspecific background signal from the serum is detectable. In contrast, autoantibodies from pat5 showed a specific binding to the unmodified wild-type (CNTN1 wt) which was lost when the first Ig domain of CNTN1 was truncated (CNTN1 del Ig1). Loss of binding was verified by incubation of HEK 293 cells transfected with CNTN1 lacking the first two Ig domains (CNTN1 del Ig1,2) with serum of pat5. Here again, no specific signal was detectable. White arrows mark specific binding. Scale bars refer to 50 µm.

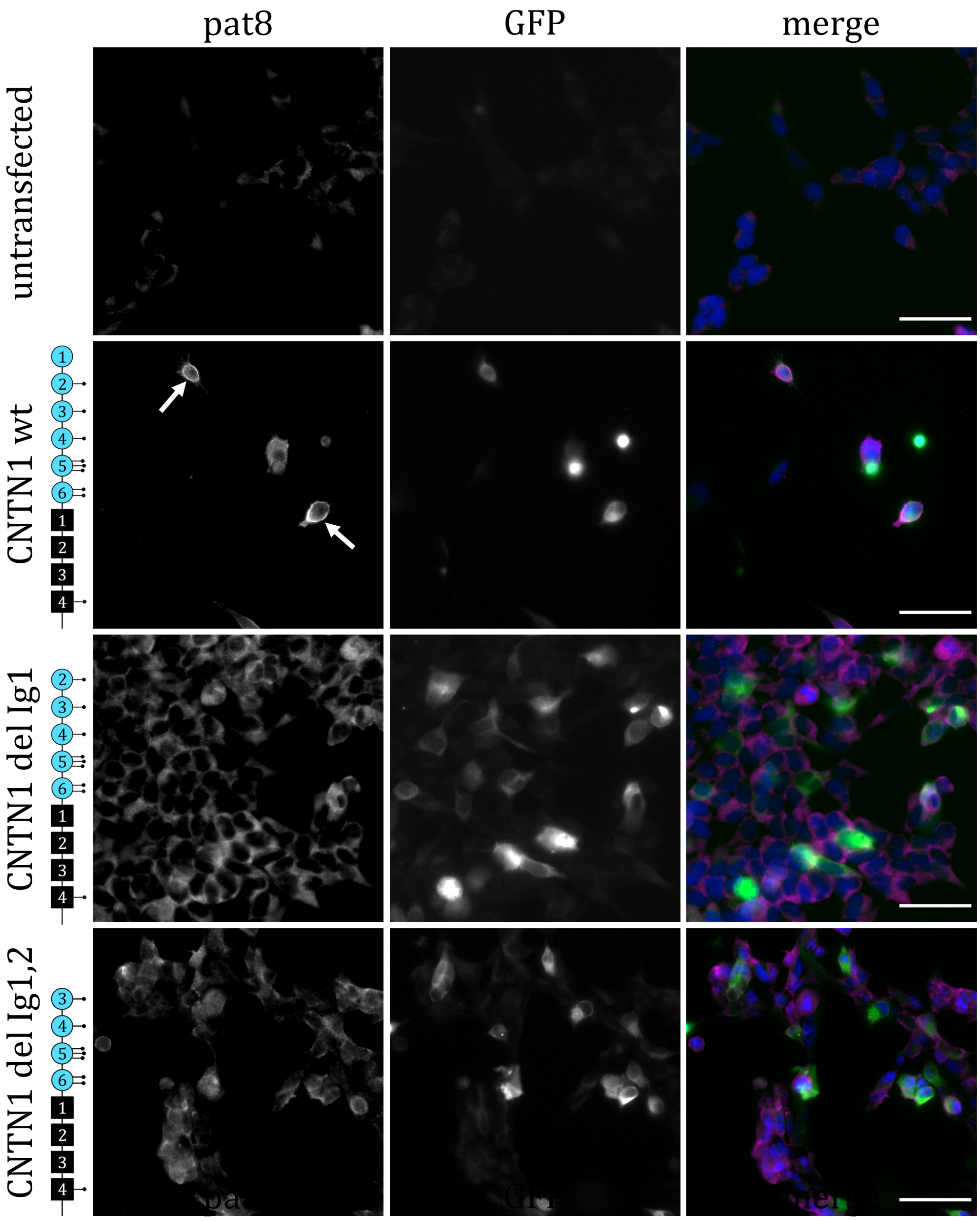

Figure 3.23: Deletion of the first Ig domain of CNTN1 prevents binding of the anti-CNTN1 positive serum of patient 8. HEK 293 cells were transiently transfected with fusion constructs of CNTN1 and eGFP (green), fixed and incubated with serum of the anti-CNTN1 positive patient 8 (pat8, magenta) and appropriate secondary antibodies. Cell nuclei are marked with DAPI. In untransfected cells, only unspecific background signal from the serum is detectable. In contrast, serum from pat8 showed a specific binding to the unmodified wild-type (CNTN1 wt). Binding was lost when the first Ig domain of CNTN1 was deleted from the protein (CNTN1 del Ig1). Incubation of HEK 293 cells transfected with CNTN1 lacking the first two Ig domains (CNTN1 del Ig1,2) with serum of pat8 verified the loss of binding. White arrows mark specific binding. Scale bars refer to 50 µm.

Table 3.4: Summary of epitope mapping assays. Data from binding assays of anti-CNTN1 positive sera from patients (pat) 1 to 8 to HEK 293 cells transfected with CNTN1 wild-type DNA (CNTN1 wt), CNTN1 glycosylation mutants lacking specific *N*-glycans or CNTN1 deletion mutants where specific Ig domains were removed. In addition, binding of sera to the native CNTN1 protein and the deglycosylated CNTN1 treated with PNGase F is shown. ND, not determined.

	pat1	**pat2**	**pat3**	**pat4**	**pat5**	**pat6**	**pat7**	**pat8**
CNTN1 wt	+	+	+	+	+	+	+	+
Glycosylation mutants								
CNTN1 N457Q	+	+	+	+	+	+	+	ND
CNTN1 N473Q	+	+	+	+	+	+	+	ND
CNTN1 N494Q	+	+	+	+	+	+	+	ND
CNTN1 N457,473Q	+	+	+	+	+	+	+	ND
CNTN1 N457,494Q	+	+	+	+	+	+	+	ND
CNTN1 N473,494Q	+	+	+	+	+	+	+	ND
CNTN1 N457,473,494Q	+	+	+	+	+	+	+	ND
Immunoblotting								
Native CNTN1	-	-	+	+	-	+	+	ND
Deglycosylated CNTN1	-	-	+	+	-	+	+	ND
Deletion mutants								
CNTN1 del Ig1	-	+	+	+	-	ND	ND	-
CNTN1 del Ig1,2	-	-	+	+	-	ND	ND	-
CNTN1 del Ig1,2,3	-	-	+	+	-	ND	ND	-
CNTN1 del Ig1-4	-	-	+	+	-	ND	ND	-
CNTN1 del Ig1-5	-	-	+	+	-	ND	ND	-
CNTN1 del Ig1-6	-	-	+	+	-	ND	ND	-
Epitope located in Ig or FnIII domains	**Ig**	**Ig**	**FnIII**	**FnIII**	**Ig**	ND	ND	**Ig**

4 Discussion

4.1 Acute passive transfer of anti-NF autoantibodies does not induce neuropathy

The clinical presentation of patients with autoantibodies against neurofascin (NF) 155 shows remarkable differences compared to those with anti-pan-NF autoantibodies. Hence, the underlying pathogenesis is suggested to differ as well. In the present study, an acute passive transfer rat model was used to study the pathogenesis of anti-NF autoantibodies *in vivo*, thereby focusing on different effects of anti-pan-NF immunoglobulin G (IgG) 3 and anti-NF155 IgG4. We investigated pathogenesis of purified IgG from two patients described in Stengel et al. (2019), one tested positive for anti-pan-NF (present study: patient 9, Stengel et al. (2019): patient 1) and the other one with anti-NF155 autoantibodies (present study: patient 10, Stengel et al. (2019): patient 4). Both patients presented with typical characteristics for the specific NF isoform(s). Thus, the anti-pan-NF positive patient showed a very severe clinical phenotype with tetraplegia and cranial nerve involvement and the anti-NF155 positive patient suffered from a predominantly distal phenotype and tremor (Stengel et al., 2019).

Purified IgG of both patients showed binding at nodes of Ranvier in rat teased fibers *in vitro*. While anti-pan-NF autoantibodies labelled the nodal as well as the paranodal region, anti-NF155 autoantibodies were directed specifically against the paranodes. These binding patterns have already been demonstrated on murine teased fibers using sera of the two patients (Stengel et al., 2019).

In a previous study, chronic intrathecal infusion of anti-NF155 IgG4 in rats led to similar clinical deficits and nerve conduction abnormalities as seen in patients (Manso et al., 2019). After five days of daily intrathecal injections, animals started to show tail weakness or paralysis which worsened over time. Electrophysiology demonstrated decreased compound muscle action potential (CMAP) amplitudes as well as reduced nerve conduction velocities (NCV) in ventral spinal roots but not in dorsal roots indicating a mainly motor involvement. However, we could not detect any deficits in animals after intraneural injection of IgG from the anti-NF155 positive patient 10. Performance in behavioral testings was comparable to the control group and nerve conduction studies (NCS) did not show any abnormalities. The discrepancy between the outcome of our study and the one of Manso et al. (2019) might be explained by the different routes of administration of anti-NF155 IgG4. While Manso et al. (2019) performed daily injections over 20 days intrathecally, we applied IgG by two intraneural injections with one day in between. As patients with anti-NF155 autoantibodies often show an acute or subacute onset of symptoms (Devaux et al., 2016; Burnor et al., 2018), our experimental setup aimed to reveal the pathomechanism of acute onset induced by these autoantibodies.

Recently, the same setup was used to transfer anti-contactin 1 (CNTN1) IgG resulting in reversible conduction blocks and motor deficits of animals (Doppler et al., 2019). The effect was more pronounced after injection of anti-CNTN1 IgG3 than after transfer of anti-CNTN1 IgG4. As we could not detect any alterations in rats treated with anti-NF155 IgG4, the pathomechanism is likely to differ between autoantibodies against CNTN1 and NF155. It is suggested that the pathogenesis of anti-CNTN1 IgG3 is complement-mediated as complement deposition was detectable at the paranodes of treated rats. However, deficits were also observed in animals injected with IgG from a patient with predominantly IgG4 autoantibodies against CNTN1. In these animals, no complement deposition at paranodes of teased fibers was observed although a smaller amount of IgG3 was also present in the injected whole IgG. Alternatively, autoantibodies might cause conduction deficits by functional blocking. Thereby, autoantibody binding to CNTN1 might disrupt axo-glial junctions leading to myelin detachment at the paranodes. The fact that autoantibody deposition was detectable at paranodes after acute exposure of anti-CNTN1 IgG (Doppler et al., 2019) but not after intraneural injection of anti-NF155 IgG might explain why we could not observe any deficits in our animal model. Lack of autoantibody binding to the paranodes in our animal model is most probably caused by inaccessability of the paranodal complex but can also be due to fast degradation of purified IgG *in vivo* or an insufficient concentration of anti-NF autoantibodies. However, the question remains why paranodes seem to be more accessible for autoantibodies directed against the axonal CNTN1 than for those directed against the glial NF155.

Apparently, autoantibodies directed against NF155 cannot access paranodes *in vivo* as shown in the present study as well as well as in a previous study after chronic intrathecal infusion (Manso et al., 2019). In the latter, autoantibody deposition was only detectable at the node vicinity and not at paranodes where NF155 is expressed at the glial side to form the axo-glial junctions together with the neuronal contactin associated protein (Caspr) and CNTN1. Previously, it has been shown that NF155 is constantly renewed during lifetime (Pillai et al., 2009). Thus, chronic infusion of autoantibodies is hypothesized to deplete NF155 prior to incorporation into newly formed paranodal junctions (Manso et al., 2019). In the present study, we chose an acute model of anti-NF155 autoantibody transfer by two intraneural injections with one day in between and behavioral and electrophysiological investigations one day and two days after the last injection, respectively. The short application time of autoantibodies seems to be insufficient to interfere with the process of newly forming paranodal junctions. Indeed, as shown in Manso et al. (2019), first abnormalities were observed as of the fifth day of daily injections and worsened until day 20. Thus, a chronic passive transfer animal model should be preferred to investigate the pathogenesis of anti-NF155 autoantibodies.

Our primary aim was to detect potential differences between the pathomechanism of acute onset after administration of anti-NF155 IgG4 and anti-pan-NF IgG3. Therefore, intraneural injections were not only performed with anti-NF155 IgG4 but also with anti-pan-NF IgG3 from patient 9. After injection of anti-pan-NF IgG3, autoantibody deposition at the nodal region was detectable in 50 % of animals treated with anti-pan-NF IgG3. This binding pattern *in vivo* fits to a previous study where a commercial antibody against pan-NF was transferred to experimental autoimmune encephalomyelitis (EAE) animals (Mathey et al., 2007). Although using an antibody directed against both, the paranodal NF155 and the nodal NF186, autoantibodies specifically bound to the nodal region in the central nervous system (CNS) (Mathey et al., 2007). Another study investigating the deposition of a commercial anti-pan-NF antibody in an experimental autoimmune neuritis (EAN) animal model confirmed this binding pattern also in the peripheral nervous system (PNS) (Yan et al., 2014). However, the present study is the first to show that patient-derived autoantibodies directed against pan-NF can access the nodes of Ranvier, but not the paranodes of naive rats *in vivo*.

Although binding of anti-pan-NF IgG was detectable at some nodes, we could not observe structural alterations as length measurements of the nodal region and paranodes were comparable to those of the healthy control group. Together with the findings from behavioral testings and NCS, a short-term effect of anti-pan-NF autoantibodies *in vivo* seems to be unlikely in our animal model. In contrast, by using an EAN rat model it has been shown that intraperitoneal injection of a commercial antibody against pan-NF exacerbated clinical symptoms already after 48 hours (Yan et al., 2014). However, the same study additionally performed intraneural injections with the commercial anti-pan-NF antibody in naive rats. In this model, first conduction blocks were observed six days after injection (Yan et al., 2014). Thus, the time course of our model might be to short to induce an antibody-mediated effect, as NCS were performed already four days after the first injection.

One day after two intraneural injections of anti-panNF IgG3 we could detect only very mild alterations in behavioral testings. Thus, motor skills evaluated by the rotarod performance test were slightly impaired in animals after the treatment with anti-pan-NF autoantibodies. Anti-pan-NF positive patients described in literature are characterized by severe motor involvement (Burnor et al., 2018; Vallat et al., 2018; Stengel et al., 2019). Only mild effects in the animal model might be explained by the short application time of autoantibodies in our experimental setting.

However, electrophysiological measurements of the sciatic nerve did not reveal any deficits. We could neither detect conduction blocks nor prolonged distal motor latency (dml) nor reduced NCV, which are all features that have been described in patients with anti-pan-NF IgG3 associated neuropathy. Strikingly, we observed slightly reduced dml after injection probably due to a measurement error at baseline. In addition, two animals of the healthy control group showed a conduction block after intraneural injection most likely induced by iatrogenic nerve damage during surgery. As mentioned before, intraneural injection of anti-CNTN1 IgG3 frequently induced conduction blocks and loss of F-waves in rats (Doppler et al., 2019). Similar to acute transfer of anti-NF155 IgG4, we could not detect any of these alterations after transfer of anti-pan-NF IgG3. This again argues for a different pathomechanism of anti-CNTN1 and anti-pan-NF autoantibodies.

In conclusion, autoantibodies directed against NF did not induce clinical symptoms in an acute passive transfer rat model. The glial isoform NF155 seems to be inaccessible for anti-NF155 IgG4 as well as for anti-pan-NF IgG3 as we could not observe antibody deposition at paranodes. In contrast, autoantibody binding to NF186 was detectable at nodes after intraneural injection of anti-pan-NF186 IgG3 indicating that the nodal region is accessible for autoantibodies *in vivo*. However, as there was no evidence of an acute effect, a chronic model should be considered for further studies concerning the pathogenesis of anti-NF autoantibodies.

4.2 Anti-CNTN1 autoantibodies reduce CNTN1 surface expression and sodium currents in DRGs *in vitro*

Autoantibodies directed against CNTN1 have been intensively studied over the last years. These studies mainly focused on the paranodes where anti-CNTN1 autoantibodies disrupt axo-glial junctions resulting in nodal widening and conduction abnormalities (Doppler et al., 2015; Koike et al., 2017; Uncini and Vallat, 2018). However, binding of anti-CNTN1 autoantibodies was also observed in the cerebellum as well as in hippocampal neurons and dorsal root ganglia (DRGs) (Querol et al., 2013; Doppler et al., 2015; Miura et al., 2015; Ricken et al., 2018). As sensory ataxia is a common clinical feature in patients with anti-CNTN1 autoantibodies, involvement of DRGs has been suggested (Miura et al., 2015). Supporting this hypothesis, we show reduced surface expression of CNTN1 along with decreased sodium currents in adult DRG neurons after incubation with sera of anti-CNTN1 positive patients.

Immunocytochemistry of adult cultivated DRG neurons revealed strong binding of anti-CNTN1 positive sera or plasma exchange (PE) material from all patients. As the signal co-localized with a commercial anti-CNTN1 antibody, it can be assumed that patients' sera specifically react against CNTN1. Binding of anti-CNTN1 autoantibodies to DRG sections has previously demonstrated (Miura et al., 2015). In the study by Miura et al. (2015), large DRG neurons showed a stronger CNTN1 signal than small neurons. However, our binding assays revealed an evenly distributed CNTN1 signal indicating that CNTN1 is expressed throughout DRG neurons of any size.

Furthermore, we demonstrated binding of anti-CNTN1 positive patients' sera to cerebellar granule neurons and to human embryonic kidney (HEK) 293 cells transfected with CNTN1 *in vitro* (Grüner et al., 2021). Incubation with patients' autoantibodies against CNTN1 led to a decrease in signal intensities of CNTN1 on the cell surface of cerebellar granule neurons, DRG neurons and HEK 293 cells transfected with CNTN1 (Grüner et al., 2021). In addition, biotinylation experiments in HEK293 cells transfected with CNTN1 showed decreased surface expression of CNTN1 after incubation with anti-CNTN1 positive patients' sera. In contrast, whole cell expression of CNTN1 remained rather stable. The effect of decreased CNTN1 surface expression was more pronounced in a patient with mainly IgG3 autoantibodies against CNTN1, but a slight reduction was also demonstrated after incubation with serum of a patient with predominantly IgG4 autoantibodies (Grüner et al., 2021).

It is known that IgG3 can induce protein cross-linking and subsequent internalization (Koneczny, 2018) which might explain our findings of decreased surface expression of CNTN1 after treatment with anti-CNTN1 IgG3. However, sera of patients 2 and 3 with mainly IgG4 autoantibodies reduced signal intensities of CNTN1 as well. As we used whole sera and not purified IgG fractions, this might be due to coexisting smaller amounts of IgG1-3. It has been shown previously that PE material of all three patients was able to mediate complement deposition and activation (Appeltshauser et al., 2017). In addition, we could show that surface expression of CNTN1 is not reduced in DRG neurons after incubation with monovalent Fab (Fragment antigen-binding) fragments of patients' autoantibodies (Grüner et al., 2021). This further supports the hypothesis of CNTN1 internalization mediated by coexisting IgG1-3 autoantibodies. However, to draw a definite conclusion about the role of different IgG subclasses, purified IgG fractions of patients' autoantibodies to CNTN1 should be used in future experiments.

IgG1-3 mediated internalization has also been demonstrated in other autoimmune diseases where IgG4 is the main subclass of autoantibodies. In anti-IgLON5 syndrome, a disease associated with sleep disturbances and movement disorders, autoantibodies to IgLON5 cause irreversible internalization of the protein *in vitro* (Sabater et al., 2016). Although IgG4 is the main subclass of anti-IgLON5 autoantibodies, the coexisting IgG1 mediates internalization as shown in experiments with purified IgG fractions. Moreover, autoantibodies against dipeptidyl-peptidase-like protein 6 (DPPX), that are associated with autoimmune encephalitis, cause reduced levels of DPPX mediated by IgG1 despite predominance of IgG4 (Hara et al., 2017). In another type of autoimmune encephalitis, Caspr2 autoantibodies induced internalization of the protein which was again attributed to coexisting IgG1 besides mostly IgG4 autoantibodies (Giannoccaro et al., 2019).

Binding of anti-CNTN1 autoantibodies has also been demonstrated in the cerebellar granule layer (Doppler et al., 2015). However, intrathecal synthesis of anti-CNTN1 autoantibodies has not been shown yet. Nevertheless, patients with anti-CNTN1 associated neuropathy often exhibit elevated protein levels in their cerebrospinal fluid (CSF) (Doppler et al., 2015; Cortese et al., 2020; Dubey et al., 2020) possibly due to a breakdown of the blood-brain barrier. Thus, an involvement of cerebellar granule neurons in the pathogenesis of anti-CNTN1 positive chronic inflammatory demyelinating polyradiculoneuropathy (CIDP) remains questionable and needs to be further investigated. In contrast, DRGs are more easily accessible for autoantibodies as the blood-DRG barrier is more permeable than the blood-brain and the blood-nerve barrier (Reinhold and Rittner, 2020). Therefore, we focused on potential effects of anti-CNTN1 autoantibodies on DRG neurons.

A previous study showed by coimmunoprecipitation that CNTN1 interacts with voltage-gated sodium (Na_V)1.2 channels via their β1 subunit (Kazarinova-Noyes et al., 2001). Furthermore, increased Na_V current densities were observed in cells cotransfected with Na_V1.2, β1 and CNTN1 compared to cells transfected with Na_V1.2 alone, Na_V1.2 and β or Na_V1.2 and CNTN1. A correlation between Na_V current densities and saxitoxin binding indicates that CNTN1 increases Na_V channel density which results in higher Na_V currents (Kazarinova-Noyes et al., 2001). Moreover, a direct interaction between CNTN1 and Na_V1.9 has been detected by coimmunoprecipitation from small-diameter DRG neurons (Liu et al., 2001). Similar to its interaction with Na_V1.2, CNTN1 also enhances the surface expression of Na_V1.9. Later, it has been shown that this interaction is dependent on the β1 subunit as CNTN1 and Na_V1.9 do not associate in β1 knockout mice (Chen et al., 2004). In addition, Na_V1.3, a channel predominantly expressed during embryonic development, interacts with CNTN1 as shown by coimmunoprecipitation from rat brain tissue (Shah et al., 2004). Cotransfection of Na_V1.3 and CNTN1 in HEK cells resulted in an almost threefold increase of current densities compared to cells transfected with Na_V1.3 alone. These findings led us to the suspicion that reduced expression of CNTN1 on DRG neurons caused by exposure to anti-CNTN1 autoantibodies might have an impact on associated Na_V channels.

As we observed a reduction of surface CNTN1 after treatment with patients' autoantibodies against CNTN1 already by conventional and confocal microscopy (Grüner et al., 2021), we aimed to investigate the expression changes in more detail by super-resolution microscopy. It has been shown for several proteins such as actin, spectrin and neurofascin that they are distributed homogeneously along axons in periodic patterns with a distance of about 190 nm (Xu et al., 2013; Zhong et al., 2014; D'Este et al., 2015; D'Este et al., 2017). This periodicity has also been found for Na_V channels (Xu et al., 2013). These studies used stochastic optical reconstruction microscopy (STORM) or stimulated emission depletion (STED), which can achieve a lateral resolution of up to 20 nm, to investigate the localization of the analyzed proteins. In contrast, the exact expression pattern of CNTN1 at an ultrastructural level has not been investigated so far. We used structured illumination microscopy (SIM) to analyze how CNTN1 is arranged in axons of DRG neurons and how treatment with anti-CNTN1 autoantibodies from seropositive patients affects this arrangement. SIM measurements revealed reduced CNTN1 surface expression on adult DRG neurons after incubation with anti-CNTN1 positive sera of all patients. Similar to cerebellar granule neurons and HEK 293 cells (Grüner et al., 2021), the signal reduction was most prominent after treatment with serum of patient 1 who had predominantly IgG3 autoantibodies. However, we were not able to identify a periodic pattern in the arrangement of CNTN1 neither for neurons treated with serum of a healthy control nor for those treated with patients' sera. This is most probably due to the lower resolution in SIM compared to STORM and STED although theoretically a lateral resolution of 100 nm can be achieved (Schermelleh et al., 2008).

As we aimed to investigate possible effects of anti-CNTN1 autoantibodies on $\mathrm{Na_V}$ channels that are associated with CNTN1 via their β1 subunit, we additionally analyzed these channels by SIM. The periodic arrangement of $\mathrm{Na_V}$ channels as it is described in Xu et al. (2013) could not be reproduced with SIM measurements, most likely due to the lower resolution compared to STORM. We thus analyzed if the surface expression of $\mathrm{Na_V}$ channels is altered after incubation with anti-CNTN1 positive patients' sera. However, $\mathrm{Na_V}$ channel signal intensities of DRG neurons treated with patients' sera were comparable with those incubated with serum from a healthy control. Thus, anti-CNTN1 autoantibodies do not influence the surface expression of associated $\mathrm{Na_V}$ channels. In contrast, colocalization analysis of CNTN1 and $\mathrm{Na_V}$ channels revealed a lower correlation between both proteins after treatment with anti-CNTN1 autoantibodies. This indicates that the association between CNTN1 and $\mathrm{Na_V}$ channels gets disrupted by autoantibodies directed against CNTN1 which is most probably caused by the internalization of CNTN1.

Although the signal reduction of CNTN1 did not result in a concomitant decrease of $\mathrm{Na_V}$ channel intensities, $\mathrm{Na_V}$ current densities were reduced after incubation with anti-CNTN1 positive patients' sera. The decrease of $\mathrm{Na_V}$ currents was observable after long-term exposure (72 hours) to anti-CNTN1 autoantibodies and not after short incubation times which is in line with the findings of reduced CNTN1 surface expression. As CNTN1 is supposed to be involved in trafficking of $\mathrm{Na_V}$ channels to the plasma membrane, we expected reduced surface expression of $\mathrm{Na_V}$ channels as the underlying mechanism for reduced $\mathrm{Na_V}$ currents. However, signal intensities of $\mathrm{Na_V}$ channels remained stable after incubation with anti-CNTN1 positive sera. As we used a pan-$\mathrm{Na_V}$ antibody for immunocytochemistry, which detects all α subunits, reduced expression of a specific channel might not be detectable but could still account for the observed decreased $\mathrm{Na_V}$ currents.

Another explanation for our findings might be that internalization of CNTN1 influences either the expression or the functional properties of β1 subunits as both proteins interact heterophilically (McEwen et al., 2004). It is known that the β1 subunit modulates expression and activity of α subunits (Calhoun and Isom, 2014). Thus, loss of CNTN1 might influence channel properties indirectly by affecting β1 subunits. Similarly, autoantibodies in anti-DPPX associated limbic encephalitis lead to internalization of DPPX, an auxiliary subunit of voltage-gated potassium ($\mathrm{K_V}$) 4.2 channels which in turn results in reduced surface levels of $\mathrm{K_V}$4.2 channels (Hara et al., 2017). Moreover, anti-leucine-rich glioma inactivated protein 1 (LGI1) autoantibodies in limbic encephalitis have been demonstrated to disrupt protein-protein interactions at the synaptic cleft

(Sonderen et al., 2017). This leads to reduced α-amino-3-hydroxy-5-methyl-4-isoxazolepropionic acid (AMPA) receptor expression in inhibitory neurons. Thus, an indirect effect of anti-CNTN1 autoantibodies on $\mathrm{Na_V}$ channels is plausible.

A previous study on DRG neurons of CNTN1 knockout mice showed that the expression of $\mathrm{Na_V}1.8$ and $\mathrm{Na_V}1.9$ as well as their current densities were reduced compared to wild-type mice (Rush et al., 2005). This study focused on small-diameter DRG neurons and their unmyelinated C-fibers. However, pain as a symptom of small fiber dysfunction is not a main clinical feature in patients with anti-CNTN1 associated CIDP. In contrast, we found reduced current densities predominantly in medium-large size DRG neurons. This fits the clinical picture of anti-CNTN1 associated CIDP as patients often present with sensory ataxia, a symptom where mainly large sensory neurons are affected. Previously, several studies on other autoimmune mediated disorders associated with sensory ataxia reported DRG involvement. As in anti-CNTN1 associated CIDP, autoantibodies against the myelin associated glycoprotein (MAG) cause axoglial detachment at nodes of peripheral nerves (Kawagashira et al., 2010). Additionally, an immunization model of anti-MAG neuropathy demonstrated sensory ganglionitis with inflammatory infiltrates (Ilyas et al., 2008). Moreover, IgG deposition was found in DRGs of patients with paraneoplastic sensory neuronopathy associated with anti-Hu autoantibodies (Dalmau et al., 1990). Only recently, autoantibodies directed against fibroblast growth factor receptor 3 have been detected in a subset of patients with sensory neuropathy (Tholance et al., 2020). The authors of the study also suggest DRGs to be the main target for autoantibodies.

In conclusion, our study is the first to show a pathogenic effect of anti-CNTN1 autoantibodies on DRG neurons besides the well-studied paranodes. Autoantibodies cause loss of surface CNTN1 most probably due to internalization by coexisting IgG1-3 besides the predominant IgG4 subclass. This leads to reduced $\mathrm{Na_V}$ currents which is potentially mediated by the $\beta1$ subunit, a direct interaction partner of CNTN1 (Fig. 4.1). However, to draw a definite conclusion about the mechanisms underlying the decreased $\mathrm{Na_V}$ currents, further studies are required. Those studies should include the use of purified subclass-specific autoantibodies from anti-CNTN1 positive patients. Moreover, studies on the effects of anti-CNTN1 autoantibodies on different $\mathrm{Na_V}$ channel subtypes and their auxiliary $\beta1$ subunits could further contribute to a better understanding of the pathogenesis in anti-CNTN1 associated neuropathy.

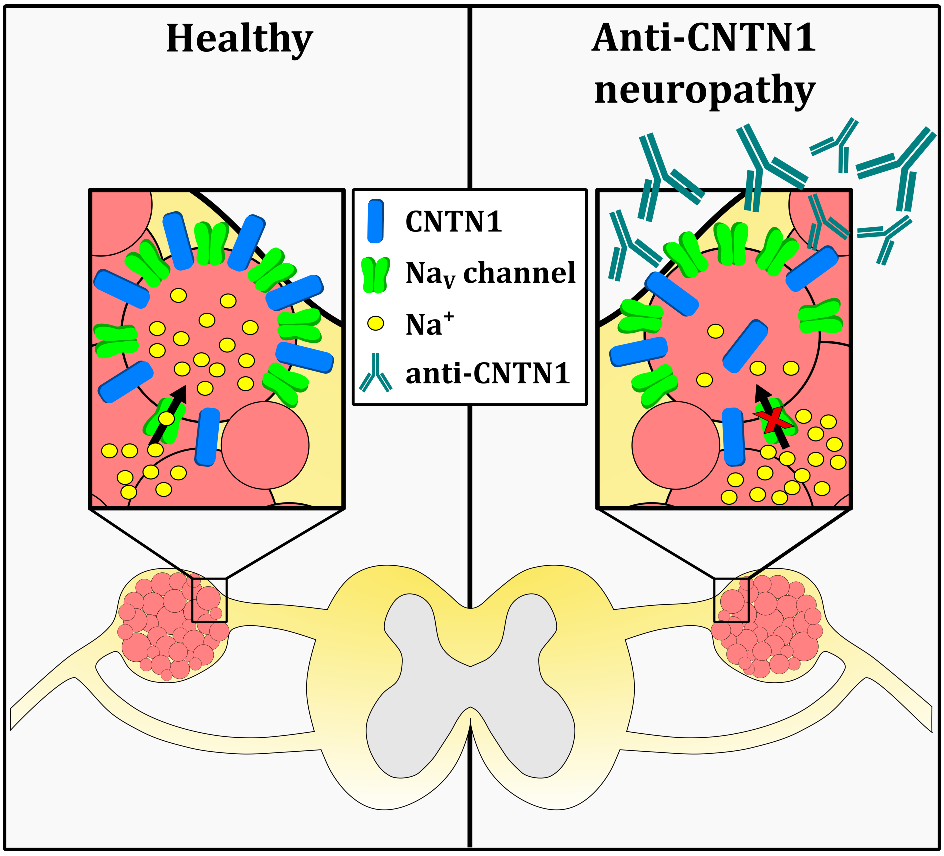

Figure 4.1: Proposed mechanism of action of anti-CNTN1 autoantibodies at DRG neurons. (A) Under normal conditions CNTN1 interacts with Na$_V$ channels via their β1 subunit. During an action potential, Na$_V$ channels get activated and Na$^+$ ions enter the cell. (B) In anti-CNTN1 neuropathy, binding of autoantibodies to CNTN1 and subsequent internalization of the protein result in decreased surface expression of CNTN1. Internalization of CNTN1 leads to reduced Na$_V$ current densities while Na$_V$ surface expression remains stable. This argues for a functional effect on Na$_V$ channels mediated by loss of CNTN1.

4.3 Possible relation between the epitope of CNTN1 and clinical features

Previously, two studies investigated the binding site of anti-CNTN1 autoantibodies from seropositive patients at the CNTN1 protein target. Labasque et al. (2014) showed that specific *N*-glycans are involved in the recognition of CNTN1 by the autoantibodies whereas the study by Miura et al. (2015) identified the protein core as the binding site. In the present study, we aimed to analyze the epitope of CNTN1 for our anti-CNTN1 positive patient cohort by investigating glycosylation of CNTN1. Moreover, CNTN1 deletion constructs were used to define preferred binding sites of the autoantibodies.

First, we could show that binding of sera from our anti-CNTN1 positive patients was independent of *N*-linked glycosylation. This is in contrast to Labasque et al. (2014), where authors identified these posttranslational modifications of the protein as the main target of anti-CNTN1 autoantibodies. In detail, they found that three of four patients' sera reacted against the immunoglobulin (Ig) domains which is dependent on *N*-linked glycans. One of these patients' sera selectively bound to CNTN1 lacking three specific *N*-glycans at amino acid positions 457, 473 and 494, which are all located in the Ig5 domain of the protein. Interestingly, the same *N*-linked glycans have been found to interact with NF155, the binding partner of CNTN1 at the paranodal junction (Labasque et al., 2014). Sera of all our patients still bound to CNTN1 lacking these *N*-linked glycans in the Ig5 domain. Peptide-*N*-glycosidase F (PNGase F) was further used to remove all *N*-linked glycans from the protein. Immunoblotting against sera from seven anti-CNTN1 positive patients revealed that autoantibodies from four patients recognized the glycosylated as well as the unglycosylated protein indicating that the binding site is independent of *N*-glycans and located in the protein core. However, sera from the other three patients did not show any specific binding neither to the glycosylated nor the unglycosylated CNTN1. This might be due to the recognition of a conformational epitope which gets lost after denaturation of the protein in the sodium dodecyl sulfate-polyacrylamide gel electrophoresis (SDS-PAGE).

To deglycosylate proteins, tunicamycin treatment of transfected cells has often been used. Tunicamycin inhibits the glycosylation of proteins at a posttranslational level in the endoplasmic reticulum. Although this method is widely used to investigate the effects of *N*-linked glycans on proteins, it has some disadvantages. Thus, tunicamycin is cytotoxic as it induces endoplasmatic reticulum stress which leads to apoptosis (Yoshida and Sakai, 2009). In addition, by preventing proteins from glycosylation prior to their transport to the membrane, tunicamycin might have an impact on the protein stability as *N*-glycans have been shown to increase the stability (Lee et al., 2015). This might also lead to temporal retention in the endoplasmic reticulum (Liu et al., 2018b). However, as shown in Bonnon et al. (2003), CNTN1 is still expressed at the cell membrane after tunicamycin treatment. In contrast, CNTN1 was retained within the cell in Labasque et al. (2014) and anti-CNTN1 positive patients' sera did not bind to the protein despite permeabilization of the cell membrane. Authors concluded that this is due to the absence of N-glycans. Another theory might be that the tunicamycin treatment affected the protein stability leading to prevention of CNTN1 recognition by the autoantibodies. This could also explain the impaired transport of CNTN1 to the cell membrane.

However, mutations of the three N-linked glycosylation sites in the Ig5 domain by site-directed mutagenesis as mentioned above validated the involvement of N-glycans in one of their patients (Labasque et al., 2014). In contrast, none of the other anti-CNTN1 positive patients' sera showed specificity to any of the generated constructs, although all of the nine glycosylation sites of the protein have been mutated and tested independently. This suggests that the epitope is not necessarily located at the N-glycans or that a combination of glycans is required for autoantibody recognition. Additionally, binding of anti-CNTN1 positive patients' sera was not prevented after preincubation with oligomannose 5 indicating that N-glycans may not be the only target of autoantibodies (Labasque et al., 2014).

Another study investigating the epitope of CNTN1 for anti-CNTN1 autoantibodies from seropositive patients was performed by Miura et al. (2015). In contrast to the study discussed above, binding of autoantibodies from anti-CNTN1 positive patients was independent of N-linked glycans (Miura et al., 2015). This has been proven by tunicamycin as well as PNGase F treatment. Furthermore, sera of all patients selectively bound to the Ig domains of CNTN1 and not to the fibronectin type III (FnIII) domains. In more detail, eight of ten anti-CNTN1 positive sera recognized the Ig5-6 domains. Unfortunately, authors do not report on the epitope of the two remaining patients.

As both of the presented studies showed different results for the epitope of CNTN1 targeted by patients' autoantibodies, it is suggested that different epitopes are involved in the pathogenesis of anti-CNTN1 autoantibodies which might lead to distinct clinical symptoms (Miura et al., 2015). Despite the discrepancies, both studies agree in a predominant involvement of the Ig domains. This is partially consistent with the results of the present study. Thus, binding of sera from four of six patients (67 %) was prevented after deletion of Ig domains. Strikingly, in three of these sera, recognition of CNTN1 was already lost after deletion of the first Ig domain, whereas in the two former studies the epitope was rather located in the Ig5-6 domains (Labasque et al., 2014; Miura et al., 2015). Interestingly, sera of the same patients did not show any binding after immunoblotting neither to the glycosylated nor to the unglycosylated CNTN1 protein. This may indicate that patients' autoantibodies are directed against a conformational epitope which gets lost after denaturation in the SDS-PAGE.

Furthermore, sera of two patients recognized the FnIII domains of CNTN1 as binding was still detectable after deletion of all Ig domains. We therefore compared clinical symptoms of patients with autoantibodies directed against CNTN1 Ig domains with those recognizing FnIII domains. Interestingly, sera of both patients with FnIII specificity had very high titers of anti-CNTN1 autoantibodies (1:10 000 and 1:19 000) compared to those that were directed against the Ig domains (1:500 to 1:7500). In addition, both patients had a chronic progression of the disease, whereas the course in the Ig domain related patients was more relapsing-remitting. Strikingly, membranous glomerulonephritis as a concurrent disease has only been diagnosed in patients with Ig domain specificity, not in those recognizing the FnIII domains. The concurrence of membranous glomerulonephritis in CIDP has been described in several studies (Kohli et al., 1992; Panjwani et al., 1996; Mobbs et al., 2000; Wu et al., 2001; Chen et al., 2006; Smyth and Menkes, 2008; Wong et al., 2015). Therefore, it was assumed that a common pathogenic mechanism might underlie both disorders (Kohli et al., 1992). Interestingly, membranous glomerulonephritis was frequently described in CIDP patients with autoantibodies against CNTN1 (Doppler et al., 2015; Taieb et al., 2019; Cortese et al., 2020; Nazarali et al., 2020). It cannot be excluded that patients from former studies might also be associated with anti-CNTN1 autoantibodies as these antibodies were discovered in 2013 for the first time (Querol et al., 2013) and have not been evaluated until then. However, clinical data of some of these patients would fit well with those described for anti-CNTN1 associated CIDP. Thus, resistance to intravenous immune globulin (IVIg) treatment (Panjwani et al., 1996; Wu et al., 2001; Wong et al., 2015) and characteristic electrophysiological features (Kohli et al., 1992; Mobbs et al., 2000; Wu et al., 2001; Chen et al., 2006) have been presented. Furthermore, IgG4 deposits in renal biopsies have been shown in two patients (Wong et al., 2015). Recently, Fehmi et al. released a preprint investigating the association of membranous glomerulonephritis and anti-CNTN1 associated CIDP in more detail. Here, 16 patients with anti-CNTN1 autoantibodies and concurrent membranous glomerulonephritis were identified. The predominant subclass of autoantibodies was IgG4 in all patients, except for four patients where IgG1 was detectable at similar levels. Deposition of CNTN1 containing immune complexes have been identified in glomeruli of anti-CNTN1 positive patients' kidney tissue (Fehmi et al., 2021a). After successful immunotherapy, symptoms of neuropathy as well as nephropathy ameliorated significantly accompanied by a decrease of anti-CNTN1 autoantibody titers. This highlights the importance of early autoantibody detection and appropriate treatment in order to avoid irreversible kidney damage (Fehmi et al., 2021a)).

Moreover, although to a lesser extent than in anti-CNTN1 mediated CIDP, nephrotic syndrome has also been associated to CIDP patients with anti-NF autoantibodies (Delmont et al., 2017;

Fehmi et al., 2021b). Strikingly, all patients were positive for anti-pan-NF autoantibodies where the epitope is located in the Ig domains of the protein, and not specifically for anti-NF155 autoantibodies. Together with the results from the present study, this may lead to the suspicion that nephrotic syndromes may be associated with autoantibodies directed against the Ig domains of CNTN1 or NF. However, as there are only a few reported cases including the epitope of autoantibodies, this needs to be further validated in future studies. As there is only data for the expression of NF186 in the glomeruli available (Sistani et al., 2013) and not for NF155, it might also be that NF155 is not even expressed in the human kidney.

However, patients with autoantibodies against pan-NF where the epitope is located in the Ig domains show lower titers compared to those positive for anti-NF155 autoantibodies that bind to the FnIII domains (Ng et al., 2012; Burnor et al., 2018; Stengel et al., 2019). This fits to the results in the present study where patients with anti-CNTN1 autoantibodies directed against the FnIII domains also showed very high titers. In addition, similar to our study, the disease course in anti-NF155 associated CIDP with the common epitope in the FnIII domains is chronic (Devaux et al., 2016; Stengel et al., 2019). In contrast, patients with anti-pan-NF autoantibodies usually show a monophasic disease course (Vallat et al., 2018; Stengel et al., 2019).

In summary, the epitope of CNTN1 and NF targeted by autoantibodies from seropositive patients seems to correlate with specific features of the disease. However, as there is limited data especially regarding the specific binding site of autoantibodies, a direct correlation needs to be further validated. Moreover, the results shown in the present should be confirmed by using a different approach other than the HEK 293 cell binding assay. This is due to a very high signal-to-noise ratio where it was difficult to distinguish specific binding from the very high background signal when using patients' material. To overcome this, preincubation assays with HEK 293 cells transfected with the generated deletion mutants of CNTN1 and subsequent analysis of binding or loss of binding should be considered in future.

5 Bibliography

Abbe, E. (1873). “Beiträge zur Theorie des Mikroskops und der mikroskopischen Wahrnehmung.” In: *Archiv für Mikroskopische Anatomie* 9.1, pp. 413–468.

Ahern, C. A., J. Payandeh, F. Bosmans, and B. Chanda (2016). “The hitchhiker’s guide to the voltage-gated sodium channel galaxy.” In: *The Journal of general physiology* 147 (1), pp. 1–24.

Allen, J. A. (2020). “The Misdiagnosis of CIDP: A Review.” In: *Neurology and therapy* 9 (1), pp. 43–54.

Appeltshauser, L., A.-M. Brunder, A. Heinius, P. Körtvélyessy, K.-P. Wandinger, R. Junker, C. Villmann, C. Sommer, F. Leypoldt, and K. Doppler (2020). “Antiparanodal antibodies and IgG subclasses in acute autoimmune neuropathy.” In: *Neurology-Neuroimmunology Neuroinflammation* 7 (5).

Appeltshauser, L., A. Weishaupt, C. Sommer, and K. Doppler (2017). “Complement deposition induced by binding of anti-contactin-1 auto-antibodies is modified by immunoglobulins.” In: *Experimental neurology* 287 (Pt 1), pp. 84–90.

Baumann, N. and D. Pham-Dinh (2001). “Biology of oligodendrocyte and myelin in the mammalian central nervous system.” In: *Physiological reviews* 81 (2), pp. 871–927.

Berg, B. van den, C. Walgaard, J. Drenthen, C. Fokke, B. C. Jacobs, and P. A. van Doorn (2014). “Guillain-Barré syndrome: pathogenesis, diagnosis, treatment and prognosis.” In: *Nature reviews. Neurology* 10 (8), pp. 469–482.

Bonnon, C., C. Bel, L. Goutebroze, B. Maigret, J.-A. Girault, and C. Faivre-Sarrailh (2007). “PGY repeats and N-glycans govern the trafficking of paranodin and its selective association with contactin and neurofascin-155”. In: *Molecular biology of the cell* 18.1, pp. 229–241.

Bonnon, C., L. Goutebroze, N. Denisenko-Nehrbass, J.-A. Girault, and C. Faivre-Sarrailh (2003). “The paranodal complex of F3/contactin and caspr/paranodin traffics to the cell surface via a non-conventional pathway.” In: *The Journal of biological chemistry* 278 (48), pp. 48339–48347.

Boukhris, S., L. Magy, G. Gallouedec, M. Khalil, P. Couratier, J. Gil, and J.-M. Vallat (2005). “Fatigue as the main presenting symptom of chronic inflammatory demyelinating polyradiculoneuropathy: a study of 11 cases.” In: *Journal of the peripheral nervous system : JPNS* 10 (3), pp. 329–337.

Boyle, M. E., E. O. Berglund, K. K. Murai, L. Weber, E. Peles, and B. Ranscht (2001). "Contactin orchestrates assembly of the septate-like junctions at the paranode in myelinated peripheral nerve". In: *Neuron* 30.2, pp. 385–397.

Broers, M. C., C. Bunschoten, D. Nieboer, H. F. Lingsma, and B. C. Jacobs (2019). "Incidence and Prevalence of Chronic Inflammatory Demyelinating Polyradiculoneuropathy: A Systematic Review and Meta-Analysis." In: *Neuroepidemiology* 52 (3-4), pp. 161–172.

Burnor, E., L. Yang, H. Zhou, K. R. Patterson, C. Quinn, M. M. Reilly, A. M. Rossor, S. S. Scherer, and E. Lancaster (2018). "Neurofascin antibodies in autoimmune, genetic, and idiopathic neuropathies." In: *Neurology* 90 (1), e31–e38.

Burton, C., L. S. Chesterton, and G. Davenport (2014). "Diagnosing and managing carpal tunnel syndrome in primary care". In: *British Journal of General Practice* 64.622, pp. 262–263.

Calhoun, J. D. and L. L. Isom (2014). "The Role of Non-pore-Forming β Subunits in Physiology and Pathophysiology of Voltage-Gated Sodium Channels". In: *Voltage Gated Sodium Channels*. Ed. by P. C. Ruben. Berlin, Heidelberg: Springer Berlin Heidelberg, pp. 51–89.

Capasso, M., F. Notturno, C. Manzoli, and A. Uncini (2011). "Involvement of sensory fibres in axonal subtypes of Guillain-Barre syndrome." In: *Journal of neurology, neurosurgery, and psychiatry* 82 (6), pp. 664–670.

Catterall, W. A. (2012). "Voltage-gated sodium channels at 60: structure, function and pathophysiology." In: *The Journal of physiology* 590 (11), pp. 2577–2589.

Chen, C., R. E. Westenbroek, X. Xu, C. A. Edwards, D. R. Sorenson, Y. Chen, D. P. McEwen, H. A. O'Malley, V. Bharucha, L. S. Meadows, G. A. Knudsen, A. Vilaythong, J. L. Noebels, T. L. Saunders, T. Scheuer, P. Shrager, W. A. Catterall, and L. L. Isom (2004). "Mice lacking sodium channel beta1 subunits display defects in neuronal excitability, sodium channel expression, and nodal architecture." In: *The Journal of neuroscience : the official journal of the Society for Neuroscience* 24 (16), pp. 4030–4042.

Chen, K.-H., C.-T. Chang, and C.-C. Hung (2006). "Glomerulonephritis associated with chronic inflammatory demyelinating polyneuropathy." In: *Renal failure* 28 (3), pp. 255–259.

Chen, N., S. He, J. Geng, Z.-J. Song, P.-H. Han, J. Qin, Z. Zhao, Y.-C. Song, H.-X. Wang, and C.-X. Dang (2018). "Overexpression of Contactin 1 promotes growth, migration and invasion in Hs578T breast cancer cells." In: *BMC cell biology* 19 (1), p. 5.

Chiba, A., S. Kusunoki, H. Obata, R. Machinami, and I. Kanazawa (1993). "Serum anti-GQ1b IgG antibody is associated with ophthalmoplegia in Miller Fisher syndrome and Guillain-Barré syndrome: clinical and immunohistochemical studies". In: *Neurology* 43.10, pp. 1911–1911.

Cortese, A., J. J. Devaux, E. Zardini, C. Manso, G. Taieb, C. Carra Dallière, P. Merle, C. Osera, S. Romagnolo, N. Visigalli, G. Piscosquito, E. Salsano, E. Alfonsi, A. Moglia, D. Pareyson, E. Marchioni, and D. Franciotta (2016). "Neurofascin-155 as a putative antigen in combined central and peripheral demyelination." In: *Neurology-Neuroimmunology Neuroinflammation* 3 (4), e238.

Cortese, A., R. Lombardi, C. Briani, I. Callegari, L. Benedetti, F. Manganelli, M. Luigetti, S. Ferrari, A. M. Clerici, G. A. Marfia, et al. (2020). "Antibodies to neurofascin, contactin-1, and contactin-associated protein 1 in CIDP: Clinical relevance of IgG isotype". In: *Neurology-Neuroimmunology Neuroinflammation* 7.1.

D'Este, E., D. Kamin, F. Balzarotti, and S. W. Hell (2017). "Ultrastructural anatomy of nodes of Ranvier in the peripheral nervous system as revealed by STED microscopy." In: *Proceedings of the National Academy of Sciences of the United States of America* 114 (2), E191–E199.

D'Este, E., D. Kamin, F. Göttfert, A. El-Hady, and S. W. Hell (2015). "STED nanoscopy reveals the ubiquity of subcortical cytoskeleton periodicity in living neurons." In: *Cell reports* 10 (8), pp. 1246–1251.

Dalmau, J., H. M. Furneaux, R. J. Gralla, M. G. Kris, and J. B. Posner (1990). "Detection of the anti-Hu antibody in the serum of patients with small cell lung cancer–a quantitative western blot analysis." In: *Annals of neurology* 27 (5), pp. 544–552.

Davis, J. Q., S. Lambert, and V. Bennett (1996). "Molecular composition of the node of Ranvier: identification of ankyrin-binding cell adhesion molecules neurofascin (mucin+/third FNIII domain-) and NrCAM at nodal axon segments." In: *The Journal of cell biology* 135 (5), pp. 1355–1367.

Delmont, E., A. Brodovitch, L. Kouton, T. Allou, S. Beltran, M. Brisset, J. P. Camdessanché, C. Cauquil, J. Cirion, T. Dubard, A. Echaniz-Laguna, A.-M. Grapperon, J. Jauffret, R. Juntas-Morales, L. D. Kremer, T. Kuntzer, C. Labeyrie, L. Lanfranco, T. Maisonobe, N. Mavroudakis, S. Mecharles-Darrigol, G. Nicolas, J.-B. Noury, M. Perie, Y. A. Rajabally, G. Remiche, V. Rouaud, C. Tard, E. Salort-Campana, A. Verschueren, K. Viala, A. Wang, S. Attarian, and J. Boucraut (2020). "Antibodies against the node of Ranvier: a real-life evaluation of incidence, clinical features and response to treatment based on a prospective analysis of 1500 sera." In: *Journal of neurology* 267 (12), pp. 3664–3672.

Delmont, E., C. Manso, L. Querol, A. Cortese, A. Berardinelli, A. Lozza, M. Belghazi, P. Malissart, P. Labauge, G. Taieb, N. Yuki, I. Illa, S. Attarian, and J. J. Devaux (2017).

“Autoantibodies to nodal isoforms of neurofascin in chronic inflammatory demyelinating polyneuropathy.” In: *Brain : a journal of neurology* 140 (7), pp. 1851–1858.

Devaux, J. J., Y. Miura, Y. Fukami, T. Inoue, C. Manso, M. Belghazi, K. Sekiguchi, N. Kokubun, H. Ichikawa, A. H. Y. Wong, et al. (2016). “Neurofascin-155 IgG4 in chronic inflammatory demyelinating polyneuropathy”. In: *Neurology* 86.9, pp. 800–807.

Dimachkie, M. M. and R. J. Barohn (2013a). “Guillain-Barré syndrome and variants.” In: *Neurologic clinics* 31 (2), pp. 491–510.

Dimachkie, M. M. and R. J. Barohn (2013b). “Chronic inflammatory demyelinating polyneuropathy.” In: *Current treatment options in neurology* 15 (3), pp. 350–366.

Dixon, W. J. (1965). “The up-and-down method for small samples”. In: *Journal of the American Statistical Association* 60.312, pp. 967–978.

Doets, A. Y., C. Verboon, B. van den Berg, T. Harbo, D. R. Cornblath, H. J. Willison, Z. Islam, S. Attarian, F. A. Barroso, K. Bateman, L. Benedetti, P. van den Bergh, C. Casasnovas, G. Cavaletti, G. Chavada, K. G. Claeys, E. Dardiotis, A. Davidson, P. A. van Doorn, T. E. Feasby, G. Galassi, K. C. Gorson, H.-P. Hartung, S.-T. Hsieh, R. A. C. Hughes, I. Illa, B. Islam, S. Kusunoki, S. Kuwabara, H. C. Lehmann, J. A. L. Miller, Q. D. Mohammad, S. Monges, E. Nobile Orazio, J. Pardo, Y. Pereon, S. Rinaldi, L. Querol, S. W. Reddel, R. C. Reisin, N. Shahrizaila, S. H. Sindrup, W. Waqar, B. C. Jacobs, and I. G. O. S. Consortium (2018). “Regional variation of Guillain-Barré syndrome.” In: *Brain : a journal of neurology* 141 (10), pp. 2866–2877.

Doppler, K., L. Appeltshauser, C. Villmann, C. Martin, E. Peles, H. H. Krämer, A. Haarmann, M. Buttmann, and C. Sommer (2016). “Auto-antibodies to contactin-associated protein 1 (Caspr) in two patients with painful inflammatory neuropathy.” In: *Brain : a journal of neurology* 139 (Pt 10), pp. 2617–2630.

Doppler, K., L. Appeltshauser, K. Wilhelmi, C. Villmann, S. D. Dib-Hajj, S. G. Waxman, M. Mäurer, A. Weishaupt, and C. Sommer (2015). “Destruction of paranodal architecture in inflammatory neuropathy with anti-contactin-1 autoantibodies.” In: *Journal of neurology, neurosurgery, and psychiatry* 86 (7), pp. 720–728.

Doppler, K., Y. Schuster, L. Appeltshauser, L. Biko, C. Villmann, A. Weishaupt, C. Werner, and C. Sommer (2019). “Anti-CNTN1 IgG3 induces acute conduction block and motor deficits in a passive transfer rat model.” In: *Journal of neuroinflammation* 16 (1), p. 73.

Doppler, K. and C. Sommer (2017). “The new entity of paranodopathies: a target structure with therapeutic consequences”. In: *Neurology International Open* 1.01, E56–E60.

Dubey, D., J. A. Honorat, S. Shelly, C. J. Klein, L. Komorowski, J. R. Mills, S. Brakopp, C. Probst, V. A. Lennon, S. J. Pittock, et al. (2020). “Contactin-1 autoimmunity:

Serologic, neurologic, and pathologic correlates". In: *Neurology-Neuroimmunology Neuroinflammation* 7.4.

Esposito, S. and M. R. Longo (2017). "Guillain-Barré syndrome." In: *Autoimmunity reviews* 16 (1), pp. 96–101.

Faivre-Sarrailh, C. (2020). "Molecular organization and function of vertebrate septate-like junctions". In: *Biochimica et Biophysica Acta (BBA)-Biomembranes* 1862.5, p. 183211.

Faivre-Sarrailh, C., F. Gauthier, N. Denisenko-Nehrbass, A. Le Bivic, G. Rougon, and J.-A. Girault (2000). "The glycosylphosphatidyl inositol-anchored adhesion molecule F3/contactin is required for surface transport of paranodin/contactin-associated protein (caspr)". In: *The Journal of cell biology* 149.2, pp. 491–502.

Fehmi, J., A. J. Davies, M. Antonelou, C. E. Teunissen, S. Keddie, S. Pikkupeura, A. Cortese, L. Querol, E. Delmont, D. Franciotta, S. Persson, J. Barratt, A. Radunovic, T. Minton, G. Fuller, S. M. Murphy, A. S. Carr, M. M. Reilly, L. Wieske, F. Eftimov, I. S. D. Roberts, N. Ashman, A. D. Salama, and S. Rinaldi (2021a). "Contactin-1 Antibodies Link Autoimmune Neuropathies to Nephrotic Syndrome". In: *Preprints with THE LANCET*.

Fehmi, J., A. J. Davies, R. J. Walters, T. Lavin, R. Keh, A. M. Rossor, T. Munteanu, N. Delanty, R. Roberts, D. Bäumer, G. Lennox, and S. Rinaldi (2021b). "IgG1 pan-neurofascin antibodies identify a severe yet treatable neuropathy with a high mortality". In: *medRxiv*.

Fujita, A., H. Ogata, R. Yamasaki, T. Matsushita, and J.-I. Kira (2018). "Parallel fluctuation of anti-neurofascin 155 antibody levels with clinico-electrophysiological findings in patients with chronic inflammatory demyelinating polyradiculoneuropathy." In: *Journal of the neurological sciences* 384, pp. 107–112.

Garg, N., S. B. Park, C. Yiannikas, S. Vucic, J. Howells, Y.-I. Noto, E. K. Mathey, J. D. Pollard, and M. C. Kiernan (2018). "Neurofascin-155 IGG4 neuropathy: pathophysiological insights, spectrum of clinical severity and response to treatment". In: *Muscle & nerve* 57.5, pp. 848–851.

Giannoccaro, M. P., D. A. Menassa, L. Jacobson, E. Coutinho, G. Prota, B. Lang, M. I. Leite, V. Cerundolo, R. Liguori, and A. Vincent (2019). "Behaviour and neuropathology in mice injected with human contactin-associated protein 2 antibodies." In: *Brain : a journal of neurology* 142 (7), pp. 2000–2012.

Goebel, A., B. Lecky, L.-J. Smith, and M. P. Lunn (2012). "Pain intensity and distribution in chronic inflammatory demyelinating polyneuropathy." In: *Muscle & nerve* 46 (2), pp. 294–295.

Golowasch, J., G. Thomas, A. L. Taylor, A. Patel, A. Pineda, C. Khalil, and F. Nadim (2009). "Membrane capacitance measurements revisited: dependence of capacitance value on measurement method in nonisopotential neurons." In: *Journal of neurophysiology* 102 (4), pp. 2161–2175.

Gordon, P. H. and A. J. Wilbourn (2001). "Early electrodiagnostic findings in Guillain-Barré syndrome." In: *Archives of neurology* 58 (6), pp. 913–917.

Grüner, J., H. Stengel, C. Werner, L. Appeltshauser, C. Sommer, C. Villmann, and K. Doppler (2021). "Anti-contactin-1 antibodies affect surface expression and sodium currents in dorsal root ganglia." In: *Neurology-Neuroimmunology Neuroinflammation*, (In Press).

Gustafsson, M. G., J. W. Sedat, and D. A. Agard (2003). *Method and apparatus for three-dimensional microscopy with enhanced resolution.* US Patent App. 09/401,041.

Hadden, R. D., H. Karch, H. P. Hartung, J. Zielasek, B. Weissbrich, J. Schubert, A. Weishaupt, D. R. Cornblath, A. V. Swan, R. A. Hughes, K. V. Toyka, and "Plasma Exchange/Sandoglobulin Guillain-Barré Syndrome Trial Group" (2001). "Preceding infections, immune factors, and outcome in Guillain-Barré syndrome." In: *Neurology* 56 (6), pp. 758–765.

Hafer-Macko, C., K. Sheikh, C. Li, T. Ho, D. Cornblath, G. McKhann, A. Asbury, and J. Griffin (1996). "Immune attack on the Schwann cell surface in acute inflammatory demyelinating polyneuropathy". In: *Annals of Neurology: Official Journal of the American Neurological Association and the Child Neurology Society* 39.5, pp. 625–635.

Hara, M., H. Ariño, M. Petit-Pedrol, L. Sabater, M. J. Titulaer, E. Martinez-Hernandez, M. W. J. Schreurs, M. R. Rosenfeld, F. Graus, and J. Dalmau (2017). "DPPX antibody-associated encephalitis: Main syndrome and antibody effects." In: *Neurology* 88 (14), pp. 1340–1348.

Hernández-Torruco, J., J. Canul-Reich, J. Frausto-Solís, and J. J. Méndez-Castillo (2014). "Feature selection for better identification of subtypes of Guillain-Barré syndrome." In: *Computational and mathematical methods in medicine* 2014, p. 432109.

Hughes, R. A., R. D. Hadden, N. A. Gregson, and K. J. Smith (1999). "Pathogenesis of Guillain-Barré syndrome." In: *Journal of neuroimmunology* 100 (1-2), pp. 74–97.

Hughes, R. A. C. and D. R. Cornblath (2005). "Guillain-Barré syndrome." In: *Lancet (London, England)* 366 (9497), pp. 1653–1666.

Huijbers, M. G., J. J. Plomp, S. M. van der Maarel, and J. J. Verschuuren (2018). "IgG4-mediated autoimmune diseases: a niche of antibody-mediated disorders". In: *Annals of the New York Academy of Sciences* 1413.1, p. 92.

Huxley, A. F. and R. Stämpfli (1949). "Evidence for saltatory conduction in peripheral myelinated nerve fibres." In: *The Journal of physiology* 108 (3), pp. 315–339.

Ilyas, A. A., Y. Gu, M. C. Dalakas, R. H. Quarles, and S. Bhatt (2008). “Induction of experimental ataxic sensory neuronopathy in cats by immunization with purified SGPG.” In: *Journal of neuroimmunology* 193 (1-2), pp. 87–93.

Isom, L. L. and W. A. Catterall (1996). “Na+ channel subunits and Ig domains.” In: *Nature* 383 (6598), pp. 307–308.

Kadoya, M., K. Kaida, H. Koike, H. Takazaki, H. Ogata, K. Moriguchi, J. Shimizu, E. Nagata, S. Takizawa, A. Chiba, et al. (2016). “IgG4 anti-neurofascin155 antibodies in chronic inflammatory demyelinating polyradiculoneuropathy: clinical significance and diagnostic utility of a conventional assay”. In: *Journal of Neuroimmunology* 301, pp. 16–22.

Kaida, K. (2019). “Guillain–Barré Syndrome”. In: *Myelin.* Springer, pp. 323–331.

Kawagashira, Y., H. Koike, M. Tomita, S. Morozumi, M. Iijima, T. Nakamura, M. Katsuno, F. Tanaka, and G. Sobue (2010). “Morphological progression of myelin abnormalities in IgM-monoclonal gammopathy of undetermined significance anti-myelin-associated glycoprotein neuropathy.” In: *Journal of neuropathology and experimental neurology* 69 (11), pp. 1143–1157.

Kazarinova-Noyes, K., J. D. Malhotra, D. P. McEwen, L. N. Mattei, E. O. Berglund, B. Ranscht, S. R. Levinson, M. Schachner, P. Shrager, L. L. Isom, and Z. C. Xiao (2001). “Contactin associates with Na+ channels and increases their functional expression.” In: *The Journal of neuroscience : the official journal of the Society for Neuroscience* 21 (19), pp. 7517–7525.

Kohli, A., P. Tandon, and V. Kher (1992). “Chronic inflammatory demyelinating polyradiculoneuropathy with membranous glomerulonephritis: report of one case.” In: *Clinical neurology and neurosurgery* 94 (1), pp. 31–33.

Koike, H., M. Kadoya, K. Kaida, S. Ikeda, Y. Kawagashira, M. Iijima, D. Kato, H. Ogata, R. Yamasaki, N. Matsukawa, et al. (2017). “Paranodal dissection in chronic inflammatory demyelinating polyneuropathy with anti-neurofascin-155 and anti-contactin-1 antibodies”. In: *Journal of Neurology, Neurosurgery & Psychiatry* 88, pp. 465–473.

Koike, H. and M. Katsuno (2020). “Pathophysiology of Chronic Inflammatory Demyelinating Polyneuropathy: Insights into Classification and Therapeutic Strategy.” In: *Neurology and Therapy.*

Komada, M. and P. Soriano (2002). “βIV-spectrin regulates sodium channel clustering through ankyrin-G at axon initial segments and nodes of Ranvier.” In: *The Journal of cell biology* 156 (2), pp. 337–348.

Koneczny, I. (2018). “A New Classification System for IgG4 Autoantibodies.” In: *Frontiers in immunology* 9, p. 97.

Kuwabara, S., Y. Sekiguchi, and S. Misawa (2017). “Electrophysiology in Fisher syndrome.” In: *Clinical neurophysiology : official journal of the International Federation of Clinical Neurophysiology* 128 (1), pp. 215–219.

Labasque, M., B. Hivert, G. Nogales-Gadea, L. Querol, I. Illa, and C. Faivre-Sarrailh (2014). “Specific contactin N-glycans are implicated in neurofascin binding and autoimmune targeting in peripheral neuropathies.” In: *The Journal of biological chemistry* 289 (11), pp. 7907–7918.

Laemmli, U. K. (1970). “Cleavage of structural proteins during the assembly of the head of bacteriophage T4”. In: *Nature* 227.5259, pp. 680–685.

Latov, N. (2014). “Diagnosis and treatment of chronic acquired demyelinating polyneuropathies.” In: *Nature reviews. Neurology* 10 (8), pp. 435–446.

Laughlin, R. S., P. J. Dyck, L. J. Melton, C. Leibson, J. Ransom, and P. J. B. Dyck (2009). “Incidence and prevalence of CIDP and the association of diabetes mellitus.” In: *Neurology* 73 (1), pp. 39–45.

Lee, H. S., Y. Qi, and W. Im (2015). “Effects of N-glycosylation on protein conformation and dynamics: Protein Data Bank analysis and molecular dynamics simulation study.” In: *Scientific reports* 5, p. 8926.

Lehmann, H. C., D. Burke, and S. Kuwabara (2019). “Chronic inflammatory demyelinating polyneuropathy: update on diagnosis, immunopathogenesis and treatment.” In: *Journal of neurology, neurosurgery, and psychiatry* 90 (9), pp. 981–987.

Lehmann, H. C., G. Meyer zu Horste, B. C. Kieseier, and H.-P. Hartung (2009). “Pathogenesis and treatment of immune-mediated neuropathies”. In: *Therapeutic advances in neurological disorders* 2.4, pp. 261–281.

Levine, T. D. (2018). “Small Fiber Neuropathy: Disease Classification Beyond Pain and Burning.” In: *Journal of central nervous system disease* 10, p. 1179573518771703.

Li, G.-Y., M. Huang, T.-T. Pan, and W.-D. Jia (2016). “Expression and prognostic significance of contactin 1 in human hepatocellular carcinoma.” In: *OncoTargets and therapy* 9, pp. 387–394.

Liu, C. J., S. D. Dib-Hajj, J. A. Black, J. Greenwood, Z. Lian, and S. G. Waxman (2001). “Direct interaction with contactin targets voltage-gated sodium channel Na(v)1.9/NaN to the cell membrane.” In: *The Journal of biological chemistry* 276 (49), pp. 46553–46561.

Liu, P., S. Chen, W. Wu, B. Liu, W. Shen, F. Wang, X. He, and S. Zhang (2012). “Contactin-1 (CNTN-1) overexpression is correlated with advanced clinical stage and lymph node metastasis in oesophageal squamous cell carcinomas.” In: *Japanese journal of clinical oncology* 42 (7), pp. 612–618.

Liu, S., C. Dong, and E. E. Ubogu (2018a). "Immunotherapy of Guillain-Barré syndrome." In: *Human vaccines & immunotherapeutics* 14 (11), pp. 2568–2579.

Liu, Y.-S., X.-Y. Guo, T. Hirata, Y. Rong, D. Motooka, T. Kitajima, Y. Murakami, X.-D. Gao, S. Nakamura, T. Kinoshita, and M. Fujita (2018b). "N-Glycan-dependent protein folding and endoplasmic reticulum retention regulate GPI-anchor processing." In: *The Journal of cell biology* 217 (2), pp. 585–599.

Loshaj-Shala, A., L. Regazzoni, A. Daci, M. Orioli, K. Brezovska, A. P. Panovska, G. Beretta, and L. Suturkova (2015). "Guillain Barré syndrome (GBS): new insights in the molecular mimicry between C. jejuni and human peripheral nerve (HPN) proteins." In: *Journal of neuroimmunology* 289, pp. 168–176.

Lukosz, v. W. and M. Marchand (1963). "Optischen Abbildung unter Überschreitung der beugungsbedingten Auflösungsgrenze". In: *Optica Acta: International Journal of Optics* 10.3, pp. 241–255.

Manso, C., L. Querol, C. Lleixà, M. Poncelet, M. Mekaouche, J.-M. Vallat, I. Illa, and J. J. Devaux (2019). "Anti-Neurofascin-155 IgG4 antibodies prevent paranodal complex formation in vivo." In: *The Journal of clinical investigation* 129 (6), pp. 2222–2236.

Martinez, A. R. M., M. B. Nunes, A. Nucci, and M. C. França (2012). "Sensory neuronopathy and autoimmune diseases." In: *Autoimmune diseases* 2012, p. 873587.

Mathey, E. K., T. Derfuss, M. K. Storch, K. R. Williams, K. Hales, D. R. Woolley, A. Al-Hayani, S. N. Davies, M. N. Rasband, T. Olsson, A. Moldenhauer, S. Velhin, R. Hohlfeld, E. Meinl, and C. Linington (2007). "Neurofascin as a novel target for autoantibody-mediated axonal injury." In: *The Journal of experimental medicine* 204 (10), pp. 2363–2372.

Mathey, E. K., N. Garg, S. Park, T. Nguyen, S. Baker, N. Yuki, C. Yiannikas, C. Lin, J. Spies, R. Ghaoui, et al. (2017). "Autoantibody responses to nodal and paranodal antigens in chronic inflammatory neuropathies". In: *Journal of Neuroimmunology* 309, pp. 41–46.

Mathey, E. K., S. B. Park, R. A. C. Hughes, J. D. Pollard, P. J. Armati, M. H. Barnett, B. V. Taylor, P. J. B. Dyck, M. C. Kiernan, and C. S.-Y. Lin (2015). "Chronic inflammatory demyelinating polyradiculoneuropathy: from pathology to phenotype." In: *Journal of neurology, neurosurgery, and psychiatry* 86 (9), pp. 973–985.

McEwen, D. P., L. S. Meadows, C. Chen, V. Thyagarajan, and L. L. Isom (2004). "Sodium channel beta1 subunit-mediated modulation of Nav1.2 currents and cell surface density is dependent on interactions with contactin and ankyrin." In: *The Journal of biological chemistry* 279 (16), pp. 16044–16049.

Miura, Y., J. J. Devaux, Y. Fukami, C. Manso, M. Belghazi, A. H. Y. Wong, N. Yuki, and C.-C. S. Group (2015). "Contactin 1 IgG4 associates to chronic inflammatory demyelinating polyneuropathy with sensory ataxia." In: *Brain : a journal of neurology* 138 (Pt 6), pp. 1484–1491.

Mobbs, R. J., R. R. Tuck, and B. Hurley (2000). "Chronic inflammatory demyelinating polyneuropathy associated with membranous glomerulonephritis: case report." In: *Journal of clinical neuroscience : official journal of the Neurosurgical Society of Australasia* 7 (5), pp. 454–455.

Mori, M. and S. Kuwabara (2011). "Fisher syndrome". In: *Current treatment options in neurology* 13.1, pp. 71–78.

Mori, M., S. Kuwabara, M. Miyake, M. Noda, H. Kuroki, H. Kanno, K. Ogawara, and T. Hattori (2000). "Haemophilus influenzae infection and Guillain-Barré syndrome." In: *Brain : a journal of neurology* 123, pp. 2171–2178.

Nascimento, O. J. M. and I. R. F. da Silva (2017). "Guillain-Barré syndrome and Zika virus outbreaks." In: *Current opinion in neurology* 30 (5), pp. 500–507.

Nazarali, S., E. K. Mathey, D. Tang, P. J. Margetts, and S. K. Baker (2020). "Chronic Inflammatory Demyelinating Polyneuropathy and Concurrent Membranous Nephropathy." In: *The Canadian journal of neurological sciences. Le journal canadien des sciences neurologiques* 47 (4), pp. 585–587.

Ng, J. K. M., J. Malotka, N. Kawakami, T. Derfuss, M. Khademi, T. Olsson, C. Linington, M. Odaka, B. Tackenberg, H. Prüss, J. M. Schwab, L. Harms, H. Harms, C. Sommer, M. N. Rasband, Y. Eshed-Eisenbach, E. Peles, R. Hohlfeld, N. Yuki, K. Dornmair, and E. Meinl (2012). "Neurofascin as a target for autoantibodies in peripheral neuropathies." In: *Neurology* 79 (23), pp. 2241–2248.

Nowicki, M., P. Baum, J. Kosacka, M. Stockinger, N. Klöting, M. Blüher, I. Bechmann, and K. V. Toyka (2014). "Effects of isoflurane anesthesia on F-waves in the sciatic nerve of the adult rat". In: *Muscle & nerve* 50.2, pp. 257–261.

Ogata, H., R. Yamasaki, A. Hiwatashi, N. Oka, N. Kawamura, D. Matsuse, M. Kuwahara, H. Suzuki, S. Kusunoki, Y. Fujimoto, et al. (2015). "Characterization of IgG4 anti-neurofascin 155 antibody-positive polyneuropathy". In: *Annals of clinical and translational neurology* 2.10, pp. 960–971.

Panjwani, M., L. D. Truong, and G. Eknoyan (1996). "Membranous glomerulonephritis associated with inflammatory demyelinating peripheral neuropathies." In: *American journal of kidney diseases : the official journal of the National Kidney Foundation* 27 (2), pp. 279–283.

Pasangulapati, S. B., T. V. Murthy, A. Sivadasan, L. R. Gideon, A. T. Prabhakar, A. Sanjith, V. Mathew, and M. Alexander (2017). "The Prevalence and Severity of Autonomic Dysfunction in Chronic Inflammatory Demyelinating Polyneuropathy." In: *Annals of Indian Academy of Neurology* 20 (3), pp. 274–277.

Pillai, A. M., C. Thaxton, A. L. Pribisko, J.-G. Cheng, J. L. Dupree, and M. A. Bhat (2009). “Spatiotemporal ablation of myelinating glia-specific neurofascin (Nfasc NF155) in mice reveals gradual loss of paranodal axoglial junctions and concomitant disorganization of axonal domains.” In: *Journal of neuroscience research* 87 (8), pp. 1773–1793.

Poliak, S. and E. Peles (2003). “The local differentiation of myelinated axons at nodes of Ranvier.” In: *Nature reviews. Neuroscience* 4 (12), pp. 968–980.

Poliak, S., D. Salomon, H. Elhanany, H. Sabanay, B. Kiernan, L. Pevny, C. L. Stewart, X. Xu, S.-Y. Chiu, P. Shrager, A. J. W. Furley, and E. Peles (2003). “Juxtaparanodal clustering of Shaker-like K+ channels in myelinated axons depends on Caspr2 and TAG-1.” In: *The Journal of cell biology* 162 (6), pp. 1149–1160.

Pollard, J. D. (2002). “Chronic inflammatory demyelinating polyradiculoneuropathy”. In: *Current opinion in neurology* 15.3, pp. 279–283.

Querol, L., G. Nogales-Gadea, R. Rojas-Garcia, E. Martinez-Hernandez, J. Diaz-Manera, X. Suárez-Calvet, M. Navas, J. Araque, E. Gallardo, and I. Illa (2013). “Antibodies to contactin-1 in chronic inflammatory demyelinating polyneuropathy”. In: *Annals of Neurology* 73.3, pp. 370–380.

Querol, L., G. Nogales-Gadea, R. Rojas-Garcia, J. Diaz-Manera, J. Pardo, A. Ortega-Moreno, M. J. Sedano, E. Gallardo, J. Berciano, R. Blesa, et al. (2014). “Neurofascin IgG4 antibodies in CIDP associate with disabling tremor and poor response to IVIg”. In: *Neurology* 82.10, pp. 879–886.

Querol, L., R. Rojas-García, J. Diaz-Manera, J. Barcena, J. Pardo, A. Ortega-Moreno, M. J. Sedano, L. Seró-Ballesteros, A. Carvajal, N. Ortiz, et al. (2015). “Rituximab in treatment-resistant CIDP with antibodies against paranodal proteins”. In: *Neurology-Neuroimmunology Neuroinflammation* 2.5.

Ranscht, B. (1988). “Sequence of contactin, a 130-kD glycoprotein concentrated in areas of interneuronal contact, defines a new member of the immunoglobulin supergene family in the nervous system.” In: *The Journal of cell biology* 107 (4), pp. 1561–1573.

Rasband, M. N. and E. Peles (2015). “The Nodes of Ranvier: Molecular Assembly and Maintenance.” In: *Cold Spring Harbor perspectives in biology* 8 (3), a020495.

Reid, R. A., D. D. Bronson, K. M. Young, and J. J. Hemperly (1994). “Identification and characterization of the human cell adhesion molecule contactin.” In: *Brain research. Molecular brain research* 21 (1-2), pp. 1–8.

Reinhold, A. K. and H. L. Rittner (2020). “Characteristics of the nerve barrier and the blood dorsal root ganglion barrier in health and disease.” In: *Experimental neurology* 327, p. 113244.

Ricken, G., C. Schwaiger, D. De Simoni, V. Pichler, J. Lang, S. Glatter, S. Macher, P. S. Rommer, P. Scholze, H. Kubista, I. Koneczny, and R. Höftberger (2018). "Detection Methods for Autoantibodies in Suspected Autoimmune Encephalitis." In: *Frontiers in neurology* 9, p. 841.

Roggenbuck, J. J., J. Boucraut, E. Delmont, K. Conrad, and D. Roggenbuck (2018). "Diagnostic insights into chronic-inflammatory demyelinating polyneuropathies." In: *Annals of translational medicine* 6 (17), p. 337.

Rush, A. M., M. J. Craner, T. Kageyama, S. D. Dib-Hajj, S. G. Waxman, and B. Ranscht (2005). "Contactin regulates the current density and axonal expression of tetrodotoxin-resistant but not tetrodotoxin-sensitive sodium channels in DRG neurons." In: *The European journal of neuroscience* 22 (1), pp. 39–49.

Sabater, L., J. Planagumà, J. Dalmau, and F. Graus (2016). "Cellular investigations with human antibodies associated with the anti-IgLON5 syndrome." In: *Journal of neuroinflammation* 13 (1), p. 226.

Salzer, J. L. (1997). "Clustering sodium channels at the node of Ranvier: close encounters of the axon-glia kind." In: *Neuron* 18 (6), pp. 843–846.

Salzer, J. L. (2015). "Schwann cell myelination." In: *Cold Spring Harbor perspectives in biology* 7 (8), a020529.

Samukawa, M., M. Kuwahara, M. Morikawa, R. Ueno, Y. Hamada, K. Takada, M. Hirano, Y. Mitsui, M. Sonoo, and S. Kusunoki (2016). "Electrophysiological assessment of Guillain-Barre syndrome with both Gal-C and ganglioside antibodies; tendency for demyelinating type". In: *Journal of Neuroimmunology* 301, pp. 61–64.

Saperstein, D. S., J. S. Katz, A. A. Amato, and R. J. Barohn (2001). "Clinical spectrum of chronic acquired demyelinating polyneuropathies." In: *Muscle & nerve* 24 (3), pp. 311–324.

Schafer, D. P., A. W. Custer, P. Shrager, and M. N. Rasband (2006). "Early events in node of Ranvier formation during myelination and remyelination in the PNS." In: *Neuron glia biology* 2 (2), pp. 69–79.

Schermelleh, L., P. M. Carlton, S. Haase, L. Shao, L. Winoto, P. Kner, B. Burke, M. C. Cardoso, D. A. Agard, M. G. Gustafsson, et al. (2008). "Subdiffraction multicolor imaging of the nuclear periphery with 3D structured illumination microscopy". In: *Science* 320.5881, pp. 1332–1336.

Schermelleh, L., R. Heintzmann, and H. Leonhardt (2010). "A guide to super-resolution fluorescence microscopy." In: *The Journal of cell biology* 190 (2), pp. 165–175.

Sejvar, J. J., A. L. Baughman, M. Wise, and O. W. Morgan (2011). "Population incidence of Guillain-Barré syndrome: a systematic review and meta-analysis." In: *Neuroepidemiology* 36 (2), pp. 123–133.

Shah, B. S., A. M. Rush, S. Liu, L. Tyrrell, J. A. Black, S. D. Dib-Hajj, and S. G. Waxman (2004). “Contactin associates with sodium channel Nav1.3 in native tissues and increases channel density at the cell surface.” In: *The Journal of neuroscience : the official journal of the Society for Neuroscience* 24 (33), pp. 7387–7399.

Shimizu, S., M. Iijima, Y. Fukami, N. Tamura, M. Nakatochi, M. Ando, R. Nishi, H. Koike, K. Kaida, M. Koga, et al. (2020). “Efficacy and safety of rituximab in refractory CIDP with or without IgG4 autoantibodies (RECIPE): protocol for a double-blind, randomized, placebo-controlled clinical trial”. In: *JMIR Research Protocols* 9.4, e17117.

Shirahata, E., H. Iwasaki, M. Takagi, C. Lin, V. Bennett, Y. Okamura, and K. Hayasaka (2006). “Ankyrin-G regulates inactivation gating of the neuronal sodium channel, Nav1.6.” In: *Journal of neurophysiology* 96 (3), pp. 1347–1357.

Sistani, L., P. Q. Rodriguez, K. Hultenby, M. Uhlen, C. Betsholtz, H. Jalanko, K. Tryggvason, A. Wernerson, and J. Patrakka (2013). “Neuronal proteins are novel components of podocyte major processes and their expression in glomerular crescents supports their role in crescent formation.” In: *Kidney international* 83 (1), pp. 63–71.

Sleigh, J. N., G. A. Weir, and G. Schiavo (2016). “A simple, step-by-step dissection protocol for the rapid isolation of mouse dorsal root ganglia”. In: *BMC research notes* 9, p. 82.

Smyth, S. and D. L. Menkes (2008). “Coincident membranous glomerulonephritis and chronic inflammatory demyelinating polyradiculoneuropathy: questioning the autoimmunity hypothesis.” In: *Muscle & nerve* 37 (1), pp. 130–135.

Sommer, C., A. Weishaupt, J. Brinkhoff, L. Biko, C. Wessig, R. Gold, and K. V. Toyka (2005). “Paraneoplastic stiff-person syndrome: passive transfer to rats by means of IgG antibodies to amphiphysin.” In: *Lancet (London, England)* 365 (9468), pp. 1406–1411.

Sonderen, A. van, M. Petit-Pedrol, J. Dalmau, and M. J. Titulaer (2017). “The value of LGI1, Caspr2 and voltage-gated potassium channel antibodies in encephalitis.” In: *Nature reviews. Neurology* 13 (5), pp. 290–301.

Stengel, H., A. Vural, A.-M. Brunder, A. Heinius, L. Appeltshauser, B. Fiebig, F. Giese, C. Dresel, A. Papagianni, F. Birklein, et al. (2019). “Anti–pan-neurofascin IgG3 as a marker of fulminant autoimmune neuropathy”. In: *Neurology-Neuroimmunology Neuroinflammation* 6.5, e603.

Susuki, K., Y. Otani, and M. N. Rasband (2016). “Submembranous cytoskeletons stabilize nodes of Ranvier.” In: *Experimental neurology* 283 (Pt B), pp. 446–451.

Taheraghdam, A., P. Pourkhanjar, M. Talebi, M. Bonyadi, A. Pashapour, E. Sharifipour, and R. Rikhtegar (2014). “Correlations between cytomegalovirus, Epstein-Barr virus, anti-ganglioside antibodies, electrodiagnostic findings and functional status in Guillain-Barré syndrome.” In: *Iranian journal of neurology* 13 (1), pp. 7–12.

Taieb, G., M. Le Quintrec, A. Pialot, I. Szwarc, H. Perrochia, P. Labauge, and J. J (2019). "'Neuro-renal syndrome' related to anti-contactin-1 antibodies." In: *Muscle & nerve* 59 (3), E19–E21.

Tang, L., Q. Huang, Z. Qin, and X. Tang (2020). "Distinguish CIDP with autoantibody from that without autoantibody: pathogenesis, histopathology, and clinical features." In: *Journal of neurology.*

Tasaki, I. (1939). "The electro-saltatory transmission of the nerve impulse and the effect of narcosis upon the nerve fiber". In: *American Journal of Physiology-Legacy Content* 127.2, pp. 211–227.

Taylor, A. M., J. Saifetiarova, and M. A. Bhat (2017). "Postnatal Loss of Neuronal and Glial Neurofascins Differentially Affects Node of Ranvier Maintenance and Myelinated Axon Function." In: *Frontiers in cellular neuroscience* 11, p. 11.

Thaxton, C., A. M. Pillai, A. L. Pribisko, J. L. Dupree, and M. A. Bhat (2011). "Nodes of Ranvier act as barriers to restrict invasion of flanking paranodal domains in myelinated axons." In: *Neuron* 69 (2), pp. 244–257.

Tholance, Y., C. P. Moritz, C. Rosier, K. Ferraud, F. Lassablière, E. Reynaud-Federspiel, M. C. França, A. R. M. Martinez, J.-P. Camdessanché, J.-C. Antoine, and a.-F. antibody Study Group (2020). "Clinical characterisation of sensory neuropathy with anti-FGFR3 autoantibodies." In: *Journal of neurology, neurosurgery, and psychiatry* 91 (1), pp. 49–57.

Thomas, S., S. Ajroud-Driss, M. M. Dimachkie, C. Gibbons, R. Freeman, D. M. Simpson, J. R. Singleton, A. G. Smith, P. S. Group, and A. Höke (2019). "Peripheral Neuropathy Research Registry: A prospective cohort." In: *Journal of the peripheral nervous system : JPNS* 24 (1), pp. 39–47.

Tubbs, R. S., E. Rizk, M. M. Shoja, M. Loukas, N. Barbaro, and R. J. Spinner (2015). *Nerves and Nerve Injuries: Vol 1: History, Embryology, Anatomy, Imaging, and Diagnostics.* Academic Press.

Uncini, A. and S. Kuwabara (2018). "The electrodiagnosis of Guillain-Barré syndrome subtypes: Where do we stand?" In: *Clinical neurophysiology : official journal of the International Federation of Clinical Neurophysiology* 129 (12), pp. 2586–2593.

Uncini, A. and S. Kuwabara (2012). "Electrodiagnostic criteria for Guillain-Barrè syndrome: a critical revision and the need for an update." In: *Clinical neurophysiology : official journal of the International Federation of Clinical Neurophysiology* 123 (8), pp. 1487–1495.

Uncini, A., K. Susuki, and N. Yuki (2013). "Nodo-paranodopathy: beyond the demyelinating and axonal classification in anti-ganglioside antibody-mediated neuropathies."

In: *Clinical neurophysiology : official journal of the International Federation of Clinical Neurophysiology* 124 (10), pp. 1928–1934.

Uncini, A. and J.-M. Vallat (2018). “Autoimmune nodo-paranodopathies of peripheral nerve: the concept is gaining ground.” In: *Journal of neurology, neurosurgery, and psychiatry* 89 (6), pp. 627–635.

Vallat, J.-M., S. Mathis, L. Magy, P. Bounolleau, M. Skarzynski, A. Heitzmann, C. Manso, J. Devaux, and A. Uncini (2018). “Subacute nodopathy with conduction blocks and anti-neurofascin 140/186 antibodies: an ultrastructural study.” In: *Brain : a journal of neurology* 141 (7), e56.

Van den Bergh, P. Y. K., R. D. M. Hadden, P. Bouche, D. R. Cornblath, A. Hahn, I. Illa, C. L. Koski, J.-M. Léger, E. Nobile-Orazio, J. Pollard, C. Sommer, P. A. van Doorn, I. N. van Schaik, E. F. of Neurological Societies, and P. N. Society (2010). “European Federation of Neurological Societies/Peripheral Nerve Society guideline on management of chronic inflammatory demyelinating polyradiculoneuropathy: report of a joint task force of the European Federation of Neurological Societies and the Peripheral Nerve Society - first revision.” In: *European journal of neurology* 17 (3), pp. 356–363.

Vucic, S., M. C. Kiernan, and D. R. Cornblath (2009). “Guillain-Barré syndrome: an update.” In: 16 (6), pp. 733–741.

Vural, A., K. Doppler, and E. Meinl (2018). “Autoantibodies against the node of Ranvier in seropositive chronic inflammatory demyelinating polyneuropathy: diagnostic, pathogenic, and therapeutic relevance”. In: *Frontiers in immunology* 9, p. 1029.

Walling, A. D. and G. Dickson (2013). “Guillain-Barré syndrome.” In: *American family physician* 87 (3), pp. 191–197.

Waxman, S. G. (1980). “Determinants of conduction velocity in myelinated nerve fibers.” In: *Muscle & nerve* 3 (2), pp. 141–150.

Wegel, E., A. Göhler, B. C. Lagerholm, A. Wainman, S. Uphoff, R. Kaufmann, and I. M. Dobbie (2016). “Imaging cellular structures in super-resolution with SIM, STED and Localisation Microscopy: A practical comparison.” In: *Scientific reports* 6, p. 27290.

Willison, H. J., B. C. Jacobs, and P. A. van Doorn (2016). “Guillain-Barré syndrome.” In: *Lancet (London, England)* 388 (10045), pp. 717–727.

Wong, A. H. Y., N. Kokubun, Y. Fukami, K. Miyaji, and N. Yuki (2015). “Chronic inflammatory demyelinating polyneuropathy with membranous nephropathy.” In: *Journal of the peripheral nervous system : JPNS* 20 (1), pp. 63–66.

Wu, A. D., J. A. Russell, and B. A. Bouthout (2001). “Chronic inflammatory demyelinating polyneuropathy and membranous glomerulonephropathy: report of two cases.” In: *Journal of clinical neuromuscular disease* 3 (2), pp. 70–74.

Wu, H.-M., W. Cao, D. Ye, G.-X. Ren, Y.-N. Wu, and W. Guo (2012). "Contactin 1 (CNTN1) expression associates with regional lymph node metastasis and is a novel predictor of prognosis in patients with oral squamous cell carcinoma." In: *Molecular medicine reports* 6 (2), pp. 265–270.

Xiao, Z. C., D. S. Ragsdale, J. D. Malhotra, L. N. Mattei, P. E. Braun, M. Schachner, and L. L. Isom (1999). "Tenascin-R is a functional modulator of sodium channel beta subunits." In: *The Journal of biological chemistry* 274 (37), pp. 26511–26517.

Xiao, Z. C., J. Taylor, D. Montag, G. Rougon, and M. Schachner (1996). "Distinct effects of recombinant tenascin-R domains in neuronal cell functions and identification of the domain interacting with the neuronal recognition molecule F3/11." In: *The European journal of neuroscience* 8 (4), pp. 766–782.

Xu, K., G. Zhong, and X. Zhuang (2013). "Actin, spectrin, and associated proteins form a periodic cytoskeletal structure in axons." In: *Science (New York, N.Y.)* 339 (6118), pp. 452–456.

Yadegari, S., S. Nafissi, and N. Kazemi (2014). "Comparison of electrophysiological findings in axonal and demyelinating Guillain-Barre syndrome." In: *Iranian journal of neurology* 13 (3), pp. 138–143.

Yan, W., T. Nguyen, N. Yuki, Q. Ji, C. Yiannikas, J. D. Pollard, and E. K. Mathey (2014). "Antibodies to neurofascin exacerbate adoptive transfer experimental autoimmune neuritis". In: *Journal of neuroimmunology* 277.1-2, pp. 13–17.

Yoshida, T. and T. Sakai (2009). "Tunicamycin". In: *Encyclopedia of Cancer*. Ed. by M. Schwab. Berlin, Heidelberg: Springer Berlin Heidelberg, pp. 3084–3087.

Yu, F. H. and W. A. Catterall (2003). "Overview of the voltage-gated sodium channel family." In: *Genome biology* 4 (3), p. 207.

Yudin, Y., B. Lutz, Y.-X. Tao, and T. Rohacs (2016). "Phospholipase C *updelta*4 regulates cold sensitivity in mice." In: *The Journal of physiology* 594 (13), pp. 3609–3628.

Yuki, N., T. Taki, F. Inagaki, T. Kasama, M. Takahashi, K. Saito, S. Handa, and T. Miyatake (1993). "A bacterium lipopolysaccharide that elicits Guillain-Barré syndrome has a GM1 ganglioside-like structure." In: *Journal of Experimental Medicine* 178.5, pp. 1771–1775.

Yuki, N. and H.-P. Hartung (2012). "Guillain-Barré syndrome." In: *The New England journal of medicine* 366 (24), pp. 2294–2304.

Zhang, A., A. Desmazieres, B. Zonta, S. Melrose, G. Campbell, D. Mahad, Q. Li, D. L. Sherman, R. Reynolds, and P. J. Brophy (2015). "Neurofascin 140 is an embryonic neuronal neurofascin isoform that promotes the assembly of the node of Ranvier." In: *The Journal of neuroscience : the official journal of the Society for Neuroscience* 35 (5), pp. 2246–2254.

Zhong, G., J. He, R. Zhou, D. Lorenzo, H. P. Babcock, V. Bennett, and X. Zhuang (2014). "Developmental mechanism of the periodic membrane skeleton in axons." In: *eLife* 3.

Zielasek, J., R. Martini, and K. V. Toyka (1996). "Functional abnormalities in P0-deficient mice resemble human hereditary neuropathies linked to P0 gene mutations". In: *Muscle & Nerve* 19.8, pp. 946–952.

A Abbreviations

ADAM	a disintegrin and metalloproteinase
AIDP	acute inflammatory demyelinating polyradiculoneuropathy
AIS	axon initial segment
AMAN	acute motor axonal neuropathy
AMPA	α-amino-3-hydroxy-5-methyl-4-isoxazolepropionic acid
AMSAN	acute motor and sensory axonal neuropathy
BSA	bovine serum albumin
BT	behavioral testing
CAM	cell adhesion molecule
Caspr	contactin associated protein
CIDP	chronic inflammatory demyelinating polyradiculoneuropathy
CMAP	compound muscle action potential
CNS	central nervous system
CNTN1	contactin 1
CSF	cerebrospinal fluid
DADS	distal acquired demyelinating symmetric
DAPI	4',6-diamidino-2-phenylindole
DMEM/F-12	Dulbecco's Modified Eagle Medium/Nutrient Mixture F-12
dml	distal motor latency
DPPX	dipeptidyl-peptidase-like protein 6
DRG	dorsal root ganglion
EAE	experimental autoimmune encephalomyelitis
EAN	experimental autoimmune neuritis
ECL	enhanced chemiluminescent
eGFP	enhanced green fluorescent protein

ELISA	enzyme-linked immunosorbent assay
Fab	Fragment antigen-binding
FBS	fetal bovine serum
FnIII	fibronectin type III
GBS	Guillain-Barré syndrome
GPI	glycophosphatidylinositol
HEK	human embryonic kidney
hrp	horseradish peroxidase
Ig	immunoglobulin
IgG	immunoglobulin G
IP	intraperitoneal
IVIg	intravenous immune globulin
K_V	voltage-gated potassium
LGI1	leucine-rich glioma inactivated protein 1
MADSAM	multifocal acquired demyelinating sensory and motor
MAG	myelin associated glycoprotein
MEM	minimum essential medium
MRI	magnetic resonance imaging
Na_V	voltage-gated sodium
NCS	nerve conduction studies
NCV	nerve conduction velocity
NF	neurofascin
NGF	nerve growth factor-7S
NGS	normal goat serum
NrCAM	neuronal cell adhesion molecule
PBS	phosphate buffered saline
PCR	polymerase chain reaction
PE	plasma exchange
Pen/Strep	Penicillin-Streptomycin
PFA	paraformaldehyde

PNGase F	peptide-N-glycosidase F
PNS	peripheral nervous system
PWL	paw withdrawal latency
PWT	paw withdrawal threshold
RCF	reversible conduction failure
rpm	revolutions per minute
RT	room temperature (21 °C)
SD	standard deviation
SDS-PAGE	sodium dodecyl sulfate-polyacrylamide gel electrophoresis
SIM	structured illumination microscopy
SNAP	sensory nerve action potential
STED	stimulated emission depletion
STORM	stochastic optical reconstruction microscopy
TBE	Tris-borate-EDTA
TBST	Tris-buffered saline with Tween 20

B List of Figures

C List of Tables

D Publication

Grüner, J., Stengel, H., Werner, C., Appeltshauser, L., Sommer, C., Villmann, C., and Doppler, K. (2021). "Anti-contactin-1 antibodies affect surface expression and sodium currents in dorsal root ganglia". In: *Neurology-Neuroimmunology Neuroinflammation.* DOI: 10.1212/NXI.0000000000001056.

E Curriculum Vitae

F Acknowledgments

First of all, I want to thank PD Dr. Kathrin Doppler and Prof. Dr. Carmen Villmann for the opportunity to work on this exciting project. Thanks for the support and encouragement throughout the whole time of my thesis.

I would like to thank Prof. Dr. Markus Sauer for being part of the thesis committee and for fruitful discussions during our annual meetings.

Thanks to everyone who helped me during the last years. I would like to thank especially Barbara Reuter for keeping the lab on track and for helping with any technical issues and experiments. Thanks to Maria Gallant for helping me with all animal experiments and the Swiss chocolate on long and exhausting "teasing Fridays". In this context, I also want to thank Lydia Biko for her support with the animals. I am also very thankful to all our other technicians, especially Barbara Dekant, Hiltrud Klüpfel, Sonja Gommersbach and Kathleen Stahl for always offering a helping hand. Thanks to Susanne Hellmig for purification of our patients' IgG.

From the Institute of Clinical Neurobiology, I want to thank all members of the AG Villmann. I always felt very welcome when I was there and occupied your lab and office. First and foremost, I want to thank Dr. Vera Rauschenberger for introducing me to the lab and helping me with everything whenever I had a question. I am also very grateful to Nadine Vornberger for her technical expertise and help especially with molecular biological methods. In this regard, I also want to thank Dana Wegmann and Christine Schmitt. Thanks to Dr. Natascha Schäfer and Dieter Janzen for always helping when questions arose. I also want to thank Dr. Corinna Martin for teaching me the DRG dissection.

Within my thesis project, I had the great opportunity to perform super-resolution microscopy at the Department of Biotechnology and Biophysics. In this context, I want to thank Marcus Behringer for introducing me to the system and always helping with technical issues. I would like to express my special thanks to Dr. Christian Werner, who helped me a lot with the analysis of the images and that he always had great ideas and comments.

Furthermore, I would like to thank all members of the AG Sommer for creating such a friendly atmosphere in the lab as well as in the office. I am very grateful to Dr. Beate Hartmannsberger for the time we spent together in the clinic and after work. I will never forget our trip to the

SfN meeting in San Diego and all the other destinations in California. I also want to express my great gratitude to Helena Stengel who taught me a lot of methods at the very beginning of my lab work. Thank you for sharing your knowledge with me, although your day was already full of your own studies. Moreover, I want to thank Dr. Luise Appeltshauser for helping with experiments and for useful comments and discussions in the course of our Seminar. Of course, I also want to thank Katharina Hecker, Inken Piro, Anna-Michelle Brunder, Antonia Hemprich, Julia Messinger and all the other people who contributed to the great atmosphere in our office. It was always a lot of fun with you!

Last but not least, I want to thank my friends and family for their great support. Special thanks to my parents Gerhard and Sabine who always believe in me and support me in every possible way. I am very grateful to have you as my sister, Stephanie! Thank you for always being there for me and telling everyone how proud you are of your “little” sister. Till, I want to thank you for everything you do for me, for your patience and for always putting a smile on my face.

Affidavit

I hereby confirm that my thesis entitled “Pathogenesis of anti-paranodal autoantibodies in peripheral neuropathies” is the result of my own work. I did not receive any help or support from commercial consultants. All sources and / or materials applied are listed and specified in the thesis.

Furthermore, I confirm that this thesis has not yet been submitted as part of another examination process neither in identical nor in similar form.

Place, Date Signature

Eidesstattliche Erklärung

Hiermit erkläre ich an Eides statt, die Dissertation „Pathogenese anti-paranodaler Autoantikörper bei peripheren Neuropathien“ eigenständig, d.h. insbesondere selbständig und ohne Hilfe eines kommerziellen Promotionsberaters, angefertigt und keine anderen als die von mir angegebenen Quellen und Hilfsmittel verwendet zu haben.

Ich erkläre außerdem, dass die Dissertation weder in gleicher noch in ähnlicher Form bereits in einem anderen Prüfungsverfahren vorgelegen hat.

Ort, Datum Unterschrift